



Title	Study of Photoelectrochemical CO ₂ Reduction by Designing Novel Metal Cathodes and Semiconductor Photoanodes with Functional Nanostructure
Author(s)	李, 牧
Citation	北海道大学. 博士(理学) 甲第12377号
Issue Date	2016-06-30
DOI	10.14943/doctoral.k12377
Doc URL	http://hdl.handle.net/2115/62454
Type	theses (doctoral)
File Information	Li_Mu.pdf



[Instructions for use](#)



**Study of Photoelectrochemical CO₂ Reduction by Designing
Novel Metal Cathodes and Semiconductor Photoanodes with
Functional Nanostructure**

(新規ナノ構造電極の構築および CO₂ の光電気化学還元に関する研究)

Mu LI

Functional Materials Chemistry Unit

Graduate School of Chemical Sciences and Engineering

Hokkaido University

2016

CONTENTS

CONTENTS	I
Abstract	1
Chapter 1 Introduction	4
1.1 General introduction	4
1.2 Photocatalytic CO ₂ reduction	7
1.2.1 Metal complex based CO ₂ reduction	9
1.2.2 Semiconductor based CO ₂ reduction	11
1.3 Electrocatalytic CO ₂ reduction	15
1.3.1 Relations between metals catalysts and their products	16
1.3.2 Reaction conditions	19
1.4 Photoelectrochemical CO ₂ reduction	20
1.4.1 Basic theory of photoelectrochemistry	20
1.4.2 Previous studies of PEC CO ₂ reduction	23
1.5 Research motivation and thesis organization	24
References	28
Chapter 2 Effect of Noble Metal Cocatalysts on Photocatalytic CO₂ Reduction over NaTaO₃ Nanoparticles	34
2.1 Introduction	34
2.2 Experimental methods	35
2.2.1 Photocatalysts preparation	35

2.2.2 Sample characterization	36
2.2.3 CO ₂ photoreduction	37
2.3 Results and discussions.....	38
2.3.1 Characteristics of NaTaO ₃ sample	38
2.3.2 The photocatalytic CO ₂ reduction with H ₂ O.....	40
2.3.3 The photocatalytic CO ₂ reduction with H ₂ O in the presence of electron donor H ₂	44
2.4 Conclusions.....	58
References.....	59

**Chapter 3 Mesoporous Palladium-Copper Bimetallic Electrodes for Selective
Electrocatalytic Reduction of Aqueous CO₂ to CO**

3.1 Introduction	62
3.2 Experimental methods	64
3.2.1 Preparation of mesoporous Pd-Cu electrocatalysts	64
3.2.2 Electrochemical measurements	65
3.2.3 Sample characterization	66
3.2.4 Computational section	67
3.3 Results and discussions.....	70
3.3.1 Characteristics of mesoporous Pd-Cu bimetallic electrocatalysts ..	70
3.3.2 The effectiveness of mesoporous nanostructure on the selectivity of CO ₂ reduction	74
3.3.3 The effectiveness of compositional ratio on the selectivity of CO ₂ reduction.....	84
3.4 Conclusions.....	97
References.....	97

Chapter 4 Design of Hierarchical Nanowire Arrays Photoanodes Based on Carbon Nanotubes and Co₃O₄ Decorated ZnO Composite for the Oxidation Half Reaction of Photoelectrochemical CO₂ Conversion	100
4.1 Introduction	100
4.2 Experimental methods	102
4.2.1 Photoanodes preparation	102
4.2.2 Sample characterization	104
4.2.3 Photoelectrochemical measurements	104
4.3 Results and discussions	105
4.3.1 Characteristics of ZnO-based NWs composite	105
4.3.2 PEC performance of pristine ZnO NWs, binary CNTs-ZnO NWs, Co ₃ O ₄ -ZnO NWs photoanode	114
4.3.3 PEC performance of ternary CNTs-ZnO-Co ₃ O ₄ NWs composite photoanode	117
4.4 Conclusions	126
References	126
Chapter 5 Design of Photoelectrochemical Device for the Selective Conversion of CO₂ to CO Using Mesoporous Palladium-Copper Bimetallic Cathode and Hierarchical ZnO-Based Nanowire Arrays Photoanode	130
5.1 Introduction	130
5.2 Experimental methods	132
5.3 Results and discussions	134

5.3.1 The effect of photoanodes on the overall PEC CO ₂ conversion	134
5.3.2 The effect of metal cathodes on the overall PEC CO ₂ conversion ..	139
5.4 Conclusions.....	150
References.....	151
Chapter 6 General Conclusion and Future Prospects.....	153
6.1 General conclusion	153
6.2 Future prospects.....	155
Acknowledgement.....	157

Abstract

Due to the increasing worldwide demand for fossil fuels and the accompanying excessive emissions of greenhouse gas carbon dioxide, finding a highly efficient, selective and economical approach toward carbon dioxide conversion becomes a great challenge in realizing an artificial system for sustainable carbon cycle. The approach of photoelectrochemical (PEC) CO₂ reduction is believed to be one of the most promising candidates for the future-oriented generation of CO₂ recycling technique, since the profound Honda-Fujishima effect has been discovered by the early 1970s. However, so far most of the PEC CO₂ reductions mainly focused on the cathodic half reaction for the directly CO₂ reduction over p-type semiconductor electrodes, such as poisonous phosphides and arsenides. The high overpotentials and limited options of photocathode candidates significantly restrict the research of PEC CO₂ conversion. Furthermore, there are still not enough reports about overall PEC CO₂ conversion. In this respect, the main strategy of this thesis is to study overall PEC CO₂ conversion process by constructing a PEC device with metal cathode and n-type semiconductor photoanode. Both of the cathodic and anodic sides were studied, respectively, and finally a PEC device was constructed by integrating these designed electrodes for obtaining a highly efficient, selective and low energy consumption CO₂ conversion.

Chapter 1 gave a general introduction of the PEC CO₂ reduction, the interrelated photocatalytic CO₂ reduction and electrochemical CO₂ reduction process as well as the design strategy of PEC construction for the study in this thesis.

In chapter 2, a photocatalytic reduction of CO₂ over wide band-gap semiconductor NaTaO₃ was investigated as a preliminary study for the following PEC CO₂ reduction. Various noble metal cocatalysts were loaded on NaTaO₃ to investigate their function in determining the activity and selectivity of photocatalytic CO₂ conversion. This study

demonstrated that the photocatalytic activities over oxides semiconductor are greatly restricted by the unstable water oxidation. On the other hand, noble metal cocatalysts significantly determined the product selectivity. The accumulation mechanism of peroxides intermediates was confirmed during the water oxidation process. Introducing electron donor H_2 could effectively overcome this drawback to obtain a stable reactivity. Ru and Pt were found effective as cocatalysts on hydrogen activation, stabilization and utilization in the presence of electron donor during the gaseous photocatalytic CO_2 reduction process. They exhibited superior activities for the selective reduction of CO_2 to CH_4 ($51.8 \mu mol h^{-1} g^{-1}$) and CO ($139.1 \mu mol h^{-1} g^{-1}$), respectively.

In chapter 3, novel mesoporous palladium-copper bimetallic electrocatalysts were studied for achieving an efficient and selective CO_2 reusable performance. It was reserved as the cathodic material within the PEC device. This was the first research by introducing mesoporous alloys as the electrocatalysts for the selective reduction of CO_2 to CO . The optimal ratio was obtained at Pd_7Cu_3 , with Faradic efficiency (FE) for CO exceeding 80% at $-0.8 V$ vs. RHE. The mesoporous nanostructures could provide roughened surfaces with abundant active sites and could promote selective conversion of CO_2 to CO . DFT calculations demonstrated that Pd atoms served as the reactive centers, while Cu could effectively altered the electronic structure and the adsorption ability of its neighbor Pd within the alloys due to the geometric and electronic effects.

Chapter 4 investigated the water oxidation half reaction over photoanode for the overall PEC CO_2 conversion. Hierarchical carbon nanotube (CNT) and Co_3O_4 decorated ZnO nanowire (NW) arrays composites were fabricated for the half reaction of water oxidation. The ZnO NWs served as the main photo-absorber. CNTs, as cocatalysts, promoted the separation and transfer of photogenerated electrons. Co_3O_4 synergistically transferred the holes and against photo-corrosion of ZnO, so that facilitated the water oxidation. It exhibits a photocurrent density ($1.9 mA cm^{-2}$ at $0.6 V$ vs. $Ag/AgCl$, 2.7

times larger than pristine ZnO NWs), improved incident photon to current conversion efficiency (52.5% at 340 nm, 5.1 times higher than pristine ZnO NWs) under AM 1.5G simulated sunlight. The heterogeneous ternary architecture with certain functional components was found as an effective approach for fabricating photoanodes.

Finally in chapter 5, an overall PEC CO₂ conversion was investigated by integrating the mesoporous Pd-Cu cathode and ZnO-based NWs composite photoanode. This was the first research attempt about overall PEC CO₂ conversion by assembling designed metal cathode and semiconductor photoanode with specific nanostructure. It was found that the overall PEC CO₂ conversion activity was an integrated performance and was determined by both of the cathodic and anodic side. The maximum FE_{CO} of the PEC CO₂ conversion is ca. 75% at bias -1.2 V, with incident photon to current conversion efficiency value of 16% at 340 nm. The metal cathode directly determined the CO₂ conversion activity depending on the density of active sites. The photoanode dominated the solar utilization efficiency of the overall PEC CO₂ conversion process.

In summary, this thesis revealed that integrating metal cathode electrocatalysts and n-type photoanode semiconductors provides a promising approach for overall PEC CO₂ conversion. The designed specific nanostructures of both the cathodic and anodic materials played important role on the performance of PEC CO₂ conversion. The mesoporous bimetallic nanostructures in cathodic side could harvest the specific active sites for selective conversion of CO₂ to CO, which benefited the stabilization of intermediates COOH* as well as the alteration of adsorption abilities of CO₂ and CO. The newly constructed ternary architecture in the photoanode side possessed dual functional cocatalysts, which individually facilitated the transfer of photogenerated charges and accelerated the reaction rates of water oxidation. Moreover, this study opened up a perspective strategy towards obtaining efficient, selective and low energy consumption PEC CO₂ conversion in the future research.

Chapter 1 Introduction

1.1 General introduction

Since the Industrial Revolution was the transition to new manufacturing processes in the past two centuries, the standard of living for the general population began to increase consistently with the fast development of technologies and the rapid growth of economies. Fossil fuels, as the primary energy resources, did great contribution to this qualitative leap. However, due to the increasing worldwide demand for fossil fuels and the accompanying excessive emissions of greenhouse gas carbon dioxide, energy shortage and global warming present to be two main crises for the sustainable development of human society in the 21st century.

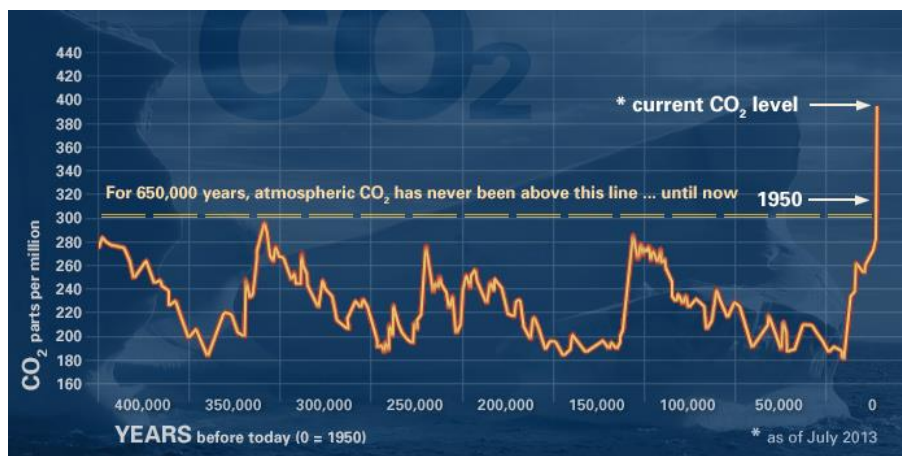


Fig. 1.1 Atmospheric CO₂ concentrations from 650,000 years ago to near present.¹

According to statistics from BP,² if production was to continue at the rate in 2014, reserves-to-production (R/P) ratio of oil was only sufficient to meet 52.5 years of global production. In the case of natural gas and coal, the time was 54.1 years and 110 years, respectively. Therefore, it is imperative to find new energy sources to substitute the

traditional fossil energy. On the other hand, human activity has increased the amount of greenhouse gases in the atmosphere, especially the excessive emission of carbon dioxide from burning fossil fuels as shown in Fig. 1.1. Global warming and climate change thus rise to be a serious risk as a result. According to the Intergovernmental Panel on Climate Change (IPCC) report, the global surface temperature is likely to raise a further 0.3 to 1.7 °C for their lowest emissions scenario using stringent mitigation and 2.6 to 4.8 °C for their highest during the 21st century.³ Thus, reducing the amount of CO₂ in the atmosphere comes to an urgent crisis that hanging over human's head.



Fig. 1.2 Carbon cycle 2.0 diagram.⁴

Artificial CO₂ chemical recycling, as an urgent research topic at the turn of the century, plays an essential role in removing CO₂ from the atmosphere and provides a new energy source simultaneously through efficient CO₂ reduction as shown in Fig. 1.2. Currently, the utilization of CO₂ as chemical feedstock is still limited to a few processes: synthesis of urea (for nitrogen fertilizers and plastics), salicylic acid (a pharmaceutical ingredient), and polycarbonates (for plastics).⁵ But this actual use only corresponds to a few percentage of the CO₂ conversion to chemicals at present

stage. To date, various CO₂ reusable approaches, such as thermocatalysis, photocatalysis, electrocatalysis, photoelectrocatalysis reduction of CO₂, etc., have been dedicatedly studied for decades for the CO₂ conversion to more useful chemicals and fuels as well as to achieve highly efficient and “clean” CO₂ conversion. Among these strategies, thermochemical CO₂ reduction is well-studied for both scientific and industrial importance, in which noble metals, such as Pt, Pd, Ru, Ni, etc., are employed as the dominant catalysts materials.⁶ However, this approach often requires operating temperatures of several hundred degrees or even beyond 1000 C°, which is an unneglectable drawback of this approach due to its large amount of energy consumption.^{7, 8}

To face a future-oriented aspect, the challenge in the research of CO₂ reduction is to develop a highly efficient and low energy consumption strategy with excellent product selectivity. In this respect, the approach of photoelectrochemical (PEC) CO₂ reduction is believed to be one of the most promising candidates for the future-oriented generation of CO₂ recycling technique, since the profound Honda-Fujishima effect has been discovered by employing a semiconductor electrode in an electrochemical cell for photolysis of water at the early 1970s.⁹ It opened up a viable way to directly utilize solar lights as the main energy source to drive the catalytic process and thus significantly reduce the extra energy consumption by introducing semiconductor photocatalysts as the catalysts materials. So far, the Honda-Fujishima effect has evolved into photocatalysis and photoelectrochemistry and attracted a great deal of research efforts for environmental remediation and alternative clean energy supplies for decades.

Photocatalysis reduction of CO₂ appears to be a promising candidate due to its property of free external energy cost besides solar lights.¹⁰ Ideally, CO₂ could react with H₂O to produce carbon products and oxygen simultaneously at the photocatalysts surface.¹¹ However, the low productivity and poor selectivity still limit the study of

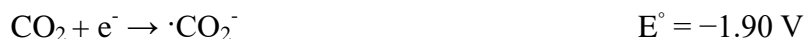
photocatalytic CO₂ reduction as well as its further application. Electrochemical reduction of CO₂ is another attractive “clean” method for its high-density renewable energy storage, incentive ability for CO₂ capture and superior product selectivity.^{12, 13} Noble metals could be directly employed as electrode materials, and it provides a much convenient way to study the relations between metal electrodes and activities and thus facilitates the study of CO₂ reduction mechanism. Moreover, the study reserve of electrochemical CO₂ reduction could also guide the design of PEC CO₂ reduction device as well as the combination options between semiconductor electrodes and electrocatalysts.

Photoelectrochemical (PEC) CO₂ reduction has been developed and researched as an promising approach to obtain an efficient CO₂ reduction and reduce the corresponding energy demand, for it possess both the advantages of photocatalytic and electrocatalytic CO₂ reduction.¹⁴ Since the first report about PEC CO₂ reduction over p-type gallium phosphide,¹⁵ several phosphides and arsenides semiconductors have been fabricated as photocathodes for CO₂ conversion.¹⁴ However, most of the PEC CO₂ reductions mainly focused on the cathodic half reaction, so far, for the directly CO₂ reduction over the semiconductor electrodes and there are still limited reports about the overall PEC CO₂ conversion. The anodic half reaction for water oxidation is also a vital part for the overall PEC CO₂ conversion process. Thus, there are still great challenges in realizing efficient overall PEC CO₂ conversion as well as the corresponding designing of PEC device to face a future-oriented CO₂ conversion demand.

1.2 Photocatalytic CO₂ reduction

Photocatalytic reduction of CO₂, an artificial photosynthesis, is based on the simulation of natural photosynthesis in green plants using solar light as the energy

source. It combines a half-reaction of CO₂ reduction and a matched oxidative half-reaction such as water oxidation, to achieve a carbon neutral cycle.¹⁰ Generally, CO₂ reduction is a chain reaction with the product varying from CO (2e⁻) to CH₄ (8e⁻). Although the reduction potential of CH₄/CO₂ is about -0.24 V vs. NHE which seems to be an attainable level to many photocatalysts, CO₂ reduction has to go through a tough uphill process and its intermediates' redox potentials are much more negative. In particular, the potential for the first electron transfer reduction of CO₂ to ·CO₂⁻ is -1.9 V vs. NHE. The thermodynamic potentials for various CO₂ reduction products are following equations (pH 7 in aqueous solution versus NHE).^{16, 17}

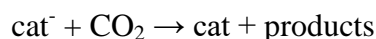
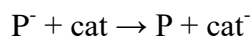
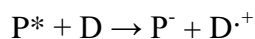
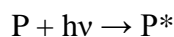


In addition to the thermodynamic aspects, the kinetic challenges of the CO₂ conversion should also be considered seriously. Although the multiple protons coupled electron transfer (PCET) steps are more favorable in thermodynamic considerations, they have only been demonstrated very low efficiencies to produce multiple-electron products such as methane or methanol. Whereas, a great deal of success has been achieved in the reduction of CO₂ to CO and formic acid. This should be associated with their own activation energies and kinetic barriers of these individual PCET steps.¹⁴ So far, there are generally two kinds of photocatalytic CO₂ reduction: transition-metal complex based CO₂ reduction and semiconductor based CO₂ reduction.

1.2.1 Metal complex based CO₂ reduction

Transition-metal compounds are at the forefront of potential catalyst research, because these catalysts can promote multiple and accessible redox states with superior multiple-electron transfer (MET) reactivity. Moreover, the formal reduction potentials can be systematically altered through ligand modification for a better matched potential of CO₂ reduction. A great deal transition-metal compounds have been studied and it commonly could be divided into two types due to the effects of complexes.

In type-I photocatalysis, a molecular light absorber and a transition metal catalyst work in concert.¹⁸ The mechanism of the type-I photocatalysis for reduction of CO₂ consists of a photosensitizer (P), typically ruthenium(II) trisbipyridine, [Ru(bpy)₃]²⁺, capable of absorbing radiation in the ultraviolet or visible region and of the generation of an excited state (P*). The excited state is reductively quenched by a sacrificial donor (D), typically trimethylamine (TEA) or triethanolamine (TEOA), generating a singly reduced photosensitizer (P⁻) and oxidized donor (D^{·+}), (i.e., Et₃N^{·+} or (HOC₂H₄)₃N^{·+}). The choice of photosensitizer must be such that P⁻ is able to transfer an electron efficiently to the catalyst species (cat) to generate the reduced catalyst species (cat⁻). The total reaction process are shown in the following equations and illustrated in Fig. 1.3.



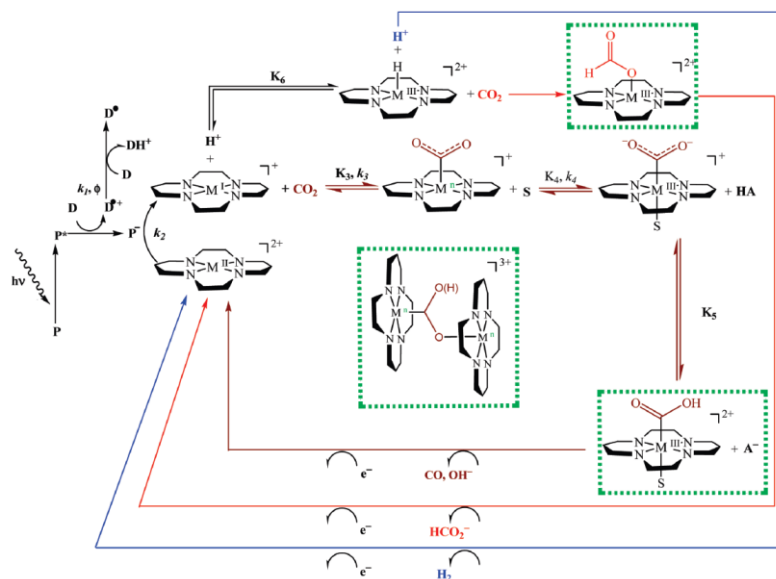


Fig. 1.3 Proposed Mechanistic Steps in the Reduction of CO₂ by Metal Tetraaza-macrocyclesa.¹⁸

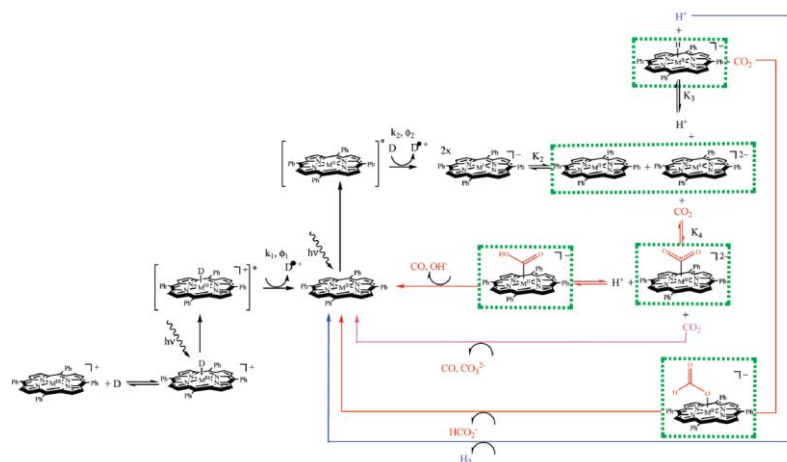


Fig. 1.4 Proposed Mechanistic Steps in the Reduction of CO₂ by Metal Porphyrin Derivatives (M = Fe or Co) via a Type II Mechanism.¹⁸

Type II catalysis occurs when one single compound acts as both the light absorber and the catalyst.¹⁸ The photocatalyst, P_{cat}, is reduced by excited-state reductive quenching as described for Type I catalysis. Similar to the reactivity discussed with type I photocatalysts, oxidized amine donors undergo subsequent reactivity to produce, D^{*},

which can reduce a second Type II compound. The reduced compound, P_{cat}^- , is an active state of the catalyst and directly interacts with CO_2 as shown in Fig. 1.4.

Although the two-type photocatalysts described above primarily produced CO formic acid as CO_2 reduction products, it is worth noting that the product formation was shown to be dependent on the presence of water and the identity of the sacrificial electron donor.¹⁹ However, looking forward to a more practical utility, some additional issues must be considered.¹⁴ Firstly, since most of the photocatalysts presently studied are metal complexes employing rare and expensive transition metals, it is especially important to raise the catalytic rate and long-term stability to make this process economically feasible. Thus, more work must be carried out to try earth-abundant elements that could support large-scale undertakings such as solar fuel production. In addition, another drawback is the use of a sacrificial donor to supply the electrons for the reduction process. Ideally, water would be the source of both the electrons and hydrogen atoms for CO_2 reduction catalysis in an artificial photosynthetic process. Thus, further investigations are still needed to achieve an efficient CO_2 reduction process.

1.2.2 Semiconductor based CO_2 reduction

Ever since the profound Honda-Fujishima effect has been discovered by the early 1970s, semiconductor photocatalysis has received much attention as a potential solution to the worldwide energy shortage due to its promising ability in directly converting solar energy into chemical fuels.⁹ In general, a semiconductor photocatalytic cycle comprises three steps as shown in Fig. 1.5: first, illumination induces a transition of electrons from the valence-band (VB) to the conduction-band (CB), leaving an equal number of vacant sites (holes); second, the excited electrons and holes migrate to the surface; third, they react with absorbed electron donors (D) and electron acceptors (A), respectively.²⁰

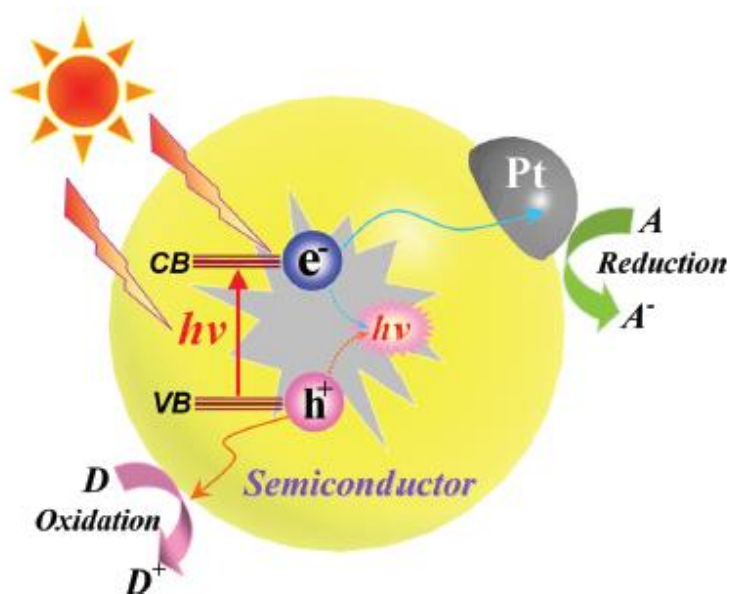


Fig. 1.5 Schematic illustration of basic mechanism of a semiconductor photocatalytic process.²⁰

In particular, photoreduction of CO_2 appears to be a highly fascinating process in lessening the requirement of fossil fuels and climate accommodations by atmospheric CO_2 balance. Since 1979, a pioneering research was reported about the photocatalytic reduction of CO_2 to formaldehyde and methanol,²¹ a great many efforts have been dedicated to the study of the semiconductor photocatalysts for CO_2 reduction. However, to date, only a limited number of materials, such as ZnGa_2O_4 ,²² Zn_2GeO_4 ,^{11, 23, 24} NaNbO_3 ,²⁵⁻²⁷ TiO_2 ,²⁸⁻³⁰ etc., have exhibited photocatalytic activities in CO_2 reduction with various reducing outcomes, which is restricted by the relations between the CB energy potential and the redox potential of products. Consequently, it enforces that the semiconductors must possess a negative enough conduction band (CB) to provide enough energy of the photogenerated electrons to overcome the activation barrier and fulfill the multiple-electron reaction during the CO_2 reduction process. That is the reason why most of the effective materials are wide band-gap semiconductors, as shown

in Fig. 1.6.

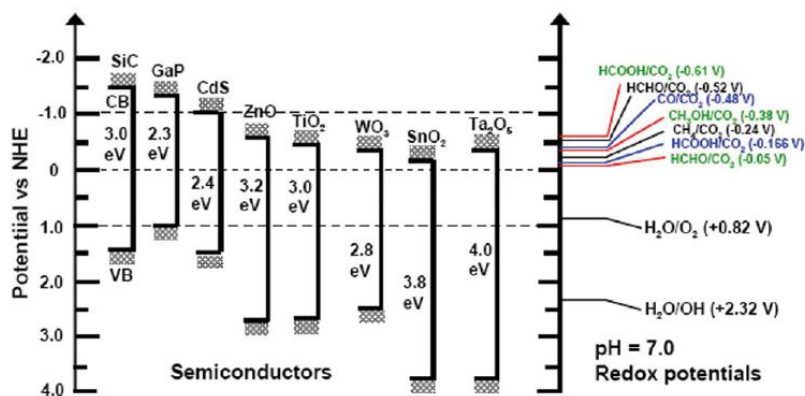


Fig. 1.6 Conduction band, valence band potentials, and band gap energies of various semiconductor photocatalysts relative to the redox potentials at pH 7 of compounds involved in CO₂ reduction.¹⁰

In previous researches, water was generally employed in reducing CO₂ as an active hydrogen source. Ideally, it is believed that CO₂ could react with H₂O to simultaneously output carbon products and O₂ through two respective half reactions with photogenerated electrons and holes in a photocatalytic process as shown in Fig. 1.7. However, O₂ could hardly be detected over most of the oxide semiconductors. It is usually accompanied by a decay of reactivity of CO₂ reduction reaction, because of some peroxide intermediates could form and accumulate on the oxide semiconductor surface during the oxygen photoevolution reaction from water.³¹ These peroxides would hinder the holes to oxidize the water and increase the recombination of the photogenerated electrons and holes, and consequently suppress the release of O₂. The unstable production rate has significantly limited the development and the practical application of CO₂ photoreduction. Electron donors were employed into the photocatalytic CO₂ reduction process over semiconductors as a solution of this unstable activity. A recently attempt showed that the photocatalytic activity and stability can be

significantly enhanced by replacing water with $\text{N}_2\text{H}_4 \cdot \text{H}_2\text{O}$ as electron donor.³² H_2 gas has also been confirmed that it can effectively facilitate the CO_2 reaction with water.^{33, 34} It opens a promising strategy to promote the photocatalytic efficiency and stability by using electron donor.²⁸

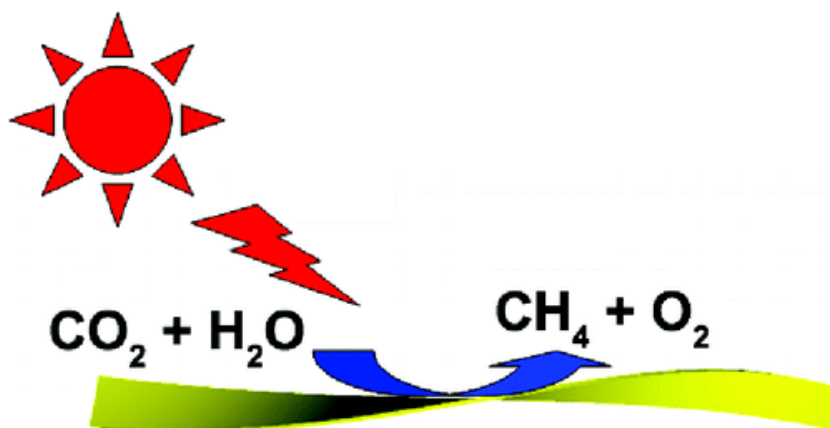


Fig. 1.7 Schematic illustration of a semiconductor photocatalytic process of CO_2 reduction with H_2O .¹¹

On the other hand, cocatalysts are commonly considered effective and broadly used in facilitating photocatalytic activities of semiconductors by (i) promoting the charge separation, (ii) improving the photostability, and (iii) lowering the activation energy of the catalytic reaction.³⁵ In particular, metal cocatalysts were well-investigated in the water reduction half reaction of water splitting, because most of the semiconductors cannot give high H_2 evolution activities without cocatalysts even in the presence of sacrificial reagents. One major reason might be the facile recombination of electron-hole pairs before migrating to the surface for reactions. Another reason is that the surface reaction is too slow to efficiently consume the charges. Thus, in order to “take” the electrons out to the surface, metal cocatalysts, such as Pt, are utilized as the cocatalysts. Noble metals not only serve as electron sinks, but also provides effective

proton reductions sites, hence dramatically facilitate proton reduction reaction. Similarly, metal cocatalysts also play an important role in the photocatalytic CO₂ reduction process,³⁶ and thus should be paid more attention to the relation between the metal cocatalysts and their corresponding activity and product selectivity. Moreover, the study of photocatalytic reduction of CO₂ over semiconductors could also reserve as a preliminary study for guiding the following research of PEC CO₂ reduction, such as the mechanism of CO₂ reduction, suitable reaction potential and reaction environment, the materials options and so on.

1.3 Electrocatalytic CO₂ reduction

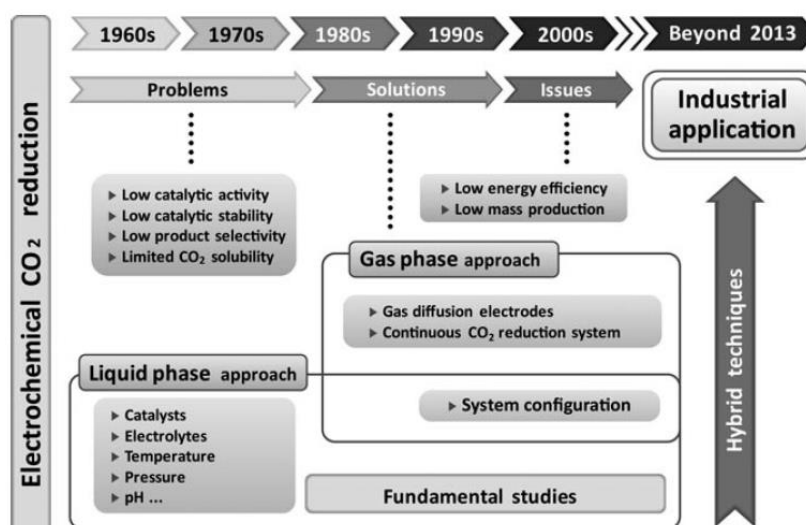


Fig. 1.8 A summary of research trend in the electrochemical CO₂ reduction.³⁷

The electrochemical reduction of CO₂ has attracted great attention due to its several advantages: (1) the catalytic process can be controlled by electrode potentials and reaction temperature; (2) the supporting electrolytes can be fully recycled and thus the overall chemical consumption can be minimized to simply water or wastewater; (3) the

electricity employed to drive the electrocatalytic process can be obtained from clean energy resources, such as solar, wind, hydroelectric, geothermal, tidal, and thermoelectric processes; (4) the electrochemical reaction systems are compact, modular, on-demand, and easy for scale-up applications.^{38,39} Since the early 1960s, a great deal of electrochemical approaches for the reduction of CO₂ have been investigated as summarized in Fig. 1.8.^{37, 40} However, challenges still remain for the further investigation of CO₂ electroreduction, such as the slow kinetics and the high energy consumption.

1.3.1 Relations between metals catalysts and their products

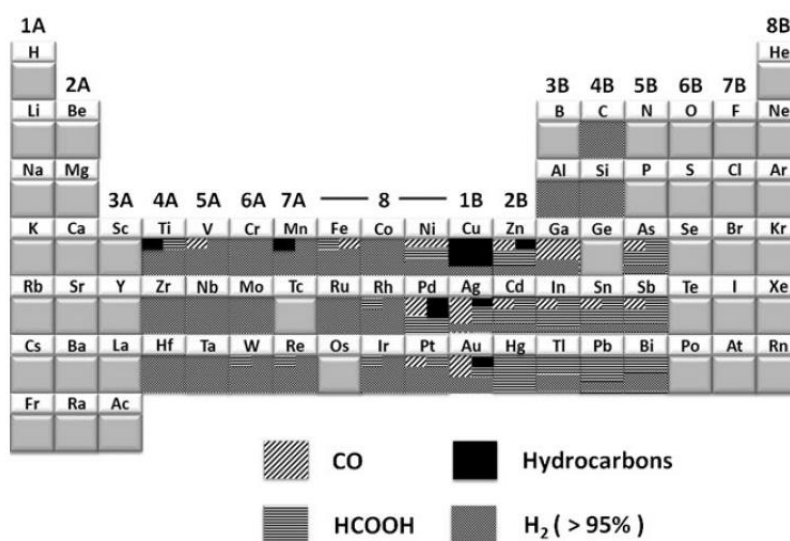


Fig. 1.9 Periodic Table showing CO₂ reduction products at ambient operating conditions.³⁷

The selectivity should be considered seriously in order to obtain desired products during the electrochemical CO₂ reduction and usually electrochemical CO₂ reduction is cited for its superior selectivity with high Faradaic efficiency (FE). Hori et al. reported

that the CO_2 reduction reaction yields CO , HCOOH , CH_4 and other hydrocarbon products, in which the selectivity is highly depended on the nature of the metallic electrode.^{41,42} Azuma et al. have summarized the relations between metal catalysts and their corresponding products as shown in Fig. 1.9.⁴³ The sp metals (e.g., Zn, Cd, Hg, In, Tl, Sn, Pb, and Bi) mainly generate formate in aqueous conditions. However, CO and hydrocarbons are the main products with d metals (e.g., Pd, Pt, Cu, Ag, and Au). The sp group metals have been applied more commonly with high current efficiency for the production of formic acid due to their excellent ability to suppress the competing hydrogen evolution reaction (HER).^{44,45}

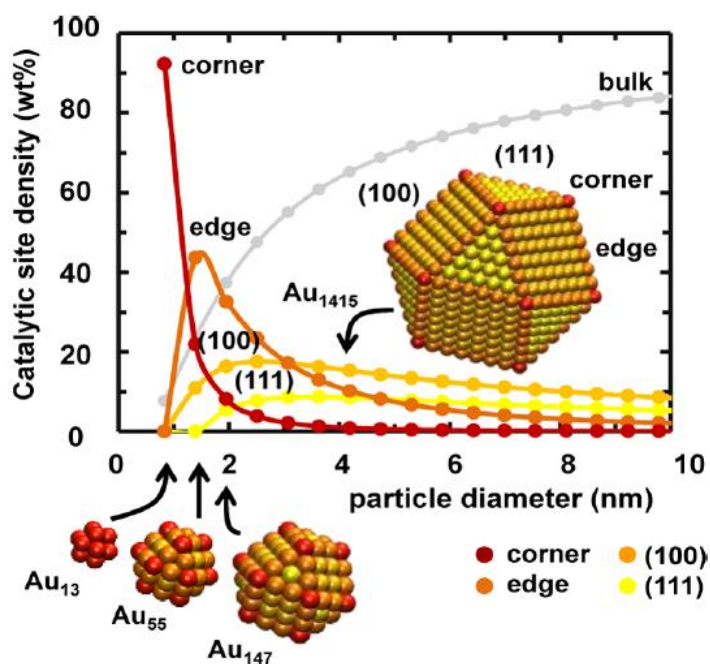


Fig. 1.10 Density of adsorption sites (yellow, light orange, dark orange, or red symbols for (111), (001), edge, or corner on-top sites, respectively) on closed-shell cuboctahedral Au clusters vs the cluster diameter.⁴⁶

Recently, d metals and their corresponding alloys have also attracted great attentions for the selective reduction of CO_2 to CO and hydrocarbons. Gold-based

nanostructured electrocatalysts demonstrated attractively high selectivity in converting CO₂ to CO, with Faradaic efficiency (FE) exceeding 90%.⁴⁶⁻⁴⁸ Recent advances in the synthesis of nanoscale Au electrocatalysts revealed that the increased reaction kinetics depend on the controlled surface area and surface morphology. It was contributed to the increased stabilization of the reduced CO₂ adsorbate and the weakened CO binding on the nanoscale Au surface.⁴⁶ In particular, active sites play a dominant role of the selective reduction of CO₂ to CO. It has been reported that the overpotential of CO₂ reduction or the partial current of CO formation on Au NPs at a given potential is controlled by the density of catalytically active edges, which is determined by NP size and surface structure. The calculated ΔG diagram suggests that Au surfaces exhibit low HER activity due to the metal's nobility,⁴⁹ while edge sites favor CO formation and corner sites are active for H₂ evolution as shown in Fig. 1.10.

On the other hand, copper-based nanoscale electrocatalysts exhibited outstanding selectivity for the reduction of CO₂ to hydrocarbon products. The hydrocarbons methane (CH₄) and ethylene (C₂H₄) are the dominant products at sufficiently negative potentials, while at less negative potentials, hydrogen (H₂), formic acid (HCOOH) and carbon monoxide (CO) appear to be major products.⁵⁰ Electrochemical methanation of CO₂ on copper electrocatalysts is one of the most attractive pathways. Because the methanation reaction involves eight electron-transfer steps at 0.17 V versus reversible hydrogen electrode (RHE) which can easily form a wide range of byproducts during the reaction, the process exhibits poor selectivity for any single product, forming a mixture of methane, ethylene, hydrogen, carbon monoxide, and formic acid.^{42, 51} The highest Faradaic efficiencies for methane reported to date are 64% on a (210) copper single crystal,⁵² 73% on an electrodeposited copper electrode,⁵³ and 80% on a dispersible nanoscale copper nanoparticles.⁵⁴ Although copper has been shown to be unique in producing hydrocarbons from CO₂, more study is still needed to overcome the high

overpotential of the CO₂ reduction on copper-based electrocatalysts.

Alloy materials have recently drawn great attention in reducing the overpotential of electrocatalytic CO₂ reduction and cutting down the amount of noble metals.⁵⁵⁻⁵⁷ It is believed that by alloying, due to the electronic effect and geometric effect, the binding strength of intermediates could be effectively tuned to accelerate the reaction rate of CO₂ reduction on the catalyst surface. The geometric effect is related to the atomic arrangement at the active site and so that determines the catalytic activity.⁵⁸ The electronic effect significantly affects the binding strength of intermediates by adjusting the electronic structure of the catalysts.⁵⁷ Thus, it shows a promising candidate strategy for the research of the selective reduction of CO₂.

1.3.2 Reaction conditions

The operating reaction conditions, such as type of media, reaction temperature, pressure, and concentrations of electrolytes, significantly influence the electrochemical reduction of CO₂, which could determine the selectivity as well as the type of products. For example, according to Hori et al.'s reports, the different concentration of electrolytes result in different product distributions of EtOH, PrnOH, CH₄, and C₂H₄ with the concentrations from 0.03 M to 1.5 M KHCO₃.⁵⁹ The solution pH also plays a key role in the obtained product distributions as well as the product selectivity.^{60, 61} In addition, it has been found that a higher pressure of CO₂ gas tends to increase the solubility and the amount of gas that reaches the surface of the electrodes for the reduction process, thus give a higher product formation faradaic efficiency.⁶²

Furthermore, the type of electrolyte solution is also one of the most challenging parts in the research of electrochemical reduction of CO₂. Since the solubility of CO₂ gas is very low in the aqueous phase (0.033m in water), while an increased solubility can be obtained in a non-aqueous media.³⁷ Ionic liquids are commonly used as an

alternative potential media for CO₂ dissolution and capture.⁶³ Although the ionic liquids and non-aqueous electrolytes demonstrate very high faradaic efficiency in reducing CO₂, the real effect of the electrolyte and active components of the electrolyte are still unclear.⁶⁴ Therefore, the study in non-aqueous media makes much more sense about the reaction process and mechanism of the selective electrochemical reduction of CO₂.

1.4 Photoelectrochemical CO₂ reduction

Research in the field of photoelectrochemical (PEC) reduction of CO₂ has grown rapidly in the last few decades due to the increasing amount of CO₂ in the atmosphere and the steady growth in global fuel demand. PEC CO₂ reduction is believed to be a promising approach, since it possesses both the advantages of photocatalytic and electrocatalytic CO₂ reduction. The great challenges presented to PEC CO₂ reduction require appropriate catalysts and energy input to realize a highly efficient, selective and low energy consumption device that minimizes the electric energy demand and utilizes the solar energy as the greatest extent during the aqueous CO₂ conversion. Thus, it poses several fundamental challenges in chemical catalysis, electrochemistry, photochemistry, and semiconductor physics and engineering.¹⁴

1.4.1 Basic theory of photoelectrochemistry

The foundation of modern photoelectrochemistry was laid down by the work of Brattain and Garret deriving from a mere support of photography⁶⁵ and Gerischer subsequently carried out the first detailed electrochemical and photoelectrochemical studies of the semiconductor–electrolyte interface.⁶⁶ Then the research on PEC cells went through a rapid development since the oil crisis in 1973, which stimulated a worldwide demand for alternative new energy sources.⁶⁷

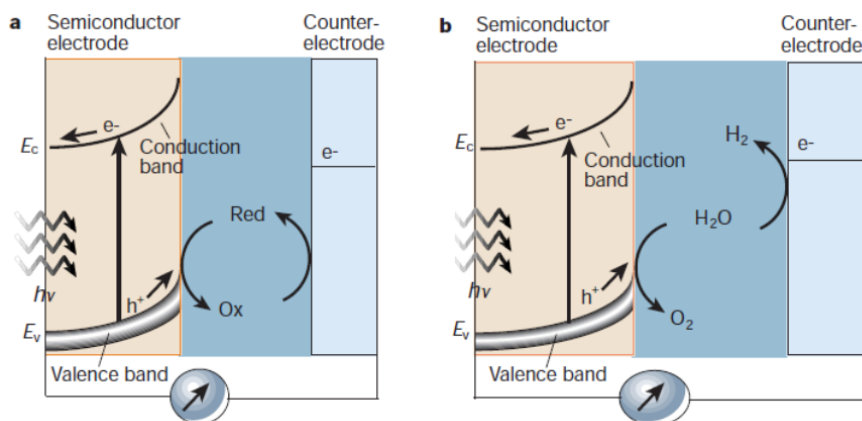


Fig. 1.11 Principle of operation of photoelectrochemical cells based on n-type semiconductors. a) Regenerative-type cell producing electric current from sunlight; b) a cell that generates a chemical fuel, hydrogen, through the photo-cleavage of water.⁶⁷

The Investigations of PEC cells could be separate into two types as shown in Fig. 1.11. The first type is the regenerative cell. It converts light to electric power without any net chemical change behind (Fig. 1.11a). The photogenerated electron-hole pairs are separated by the electric field present in the space-charge layer. Then the electrons transfer through the bulk semiconductor and the external circuit to the counter side. On the other hand, the holes are driven to the surface to oxidize a redox relay molecule (R): $h^+ + R \rightarrow O$. The oxidized form O is finally reduced back to R at the counter side and thus accomplishes a recycle process. The research on regenerative cells were mainly focused on electron-doped (n-type) II/VI or III/V semiconductors using electrolytes based on sulphide/polysulphide, vanadium(II)/vanadium(III) or I₂/I⁻ redox couples.⁶⁸ The second type is photosynthetic cells which operate on a similar principle with the first type but go through two respective redox systems (Fig. 1.11b): one carries out an oxidation reaction using holes at the surface of photoanode and the other reacting with the electrons through a reduction reaction in the photocathode side. The type two PEC cells were well-studied in the past decades for water splitting, CO₂ reduction, hydrogen

sulfide splitting, etc., in which PEC water splitting has drawn most of the attentions.

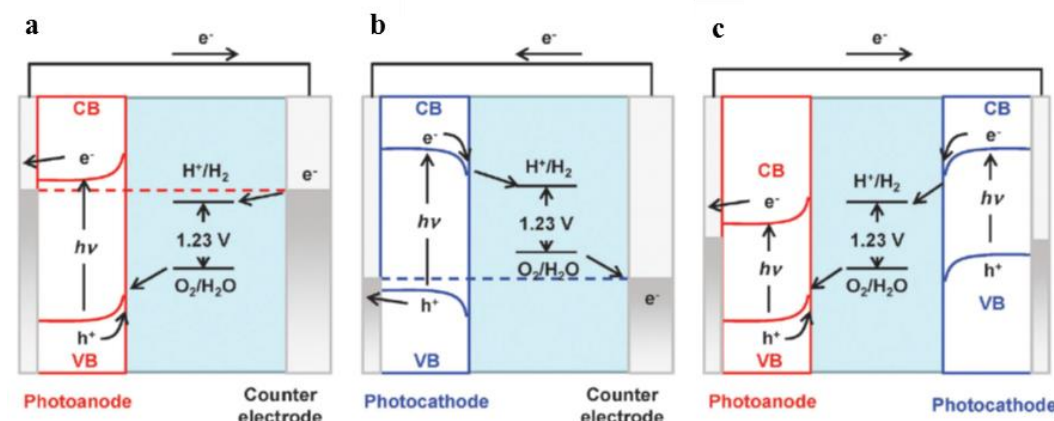


Fig. 1.12 Energy diagrams of PEC water splitting a) photoanode, b) photocathode, and c) photoanode and photocathode in tandem configuration.⁶⁹

Fig. 1.12 illustrates thermodynamics of PEC water splitting as an example of the basic reaction mechanism of PEC cells. When a semiconductor electrode is immersed into an electrolyte solution, electron transfer takes place between the semiconductor and the electrolyte solution so that the Fermi level is equilibrated with the redox potential of electrolyte solution.⁷⁰ The Fermi level equilibrium leads to a band bending, since the density of electrons in a semiconductor is finite and the Fermi level of the semiconductor is more negative (positive) than the reduction potential of the electrolyte solution.⁶⁹ The electric field induced by the space charge layer plays an important role in charge separation.⁷⁰ In the case of n-type semiconductor photoelectrodes, which usually act as photoanodes, the photogenerated holes accumulate at the surface of the semiconductor and then enroll in the oxidation reactions. Meanwhile, the photogenerated electrons are transferred to a counter electrode via an external circuit, and consumed in the reduction reactions (Fig. 1.12a). The top of the valence band must be more positive than the oxygen evolution potential so that the water oxidation reaction

could be carried out. On the other hand, a p-type semiconductor serves as a photocathode for hydrogen evolution and thus it requires the conduction band edge is more negative than the hydrogen evolution potential (Fig. 1.12b). Consequently, PEC reactions on photoelectrodes are driven by photoexcited minority carriers in both cases. The potential of electrons on the counter electrode is identical to the Fermi level of the photoelectrode under illumination. Usually, an external bias is applied between the photoelectrode and counter electrode to compensate for the potential deficiency. So that the desired reactions on a counter electrode can be proceeded, even if the Fermi level of the photoelectrode is positioned at an undesirable potential.⁶⁹ Furthermore, a photoanode and a photocathode can be integrated together to carry out overall water splitting (Fig. 1.12c) instead of using a single photoelectrode and a counter electrode. The maximum photocurrent and the working potential of the photoelectrodes are theoretically determined by the intersection of the steady current-potential curves of the respective photoelectrodes in the total PEC water splitting configuration.⁷¹

1.4.2 Previous studies of PEC CO₂ reduction

Halmann et al. reported one of the earliest study of PEC CO₂ reduction by using p-type GaP as photocathode in 1978.¹⁵ From then on, many research groups focused their researches on the PEC CO₂ reduction at different kinds of photocathodes. Similar to the electrochemical reduction of CO₂, the reaction conditions also exhibited significantly influence on the activity and selectivity PEC CO₂ reduction. Among various semiconductors, Si, InP, GaP, GaAs, GaAs, etc. attracted most of the research focuses due to their superior activities. The main product for the PEC CO₂ reduction in most nonaqueous solvents on p-Si,⁷²⁻⁷⁴ p-InP,^{72, 73, 75} p-GaAs,^{72, 73, 75} and p-GaP⁷² in various nonaqueous solvents was CO with varying FE. Both p- and n-type GaAs have been used for direct PEC reduction of CO₂ and exhibited their outstanding ability in

converting CO₂ to methanol.⁷⁶ Bocarsly et al. have also reported a selective reduction to methanol on p-GaP photocathode.⁷⁷ (111) p⁺/p-Si has exhibited a selective reduction of CO₂ to formate in an aqueous Na₂SO₄ electrolyte solution.^{78,79} Yoneyama et al. reported the reduction of CO₂ on (111) surface p-CdTe and (100) surface p-InP with various electrolytes at -1.2 V versus SCE.⁸⁰ InP was found to be more selective for proton reduction (FE ≥ 60%) than CdTe (FE ≥ 38%). When tetraalkylammonium electrolytes were used, proton reduction to H₂ decreased on both CdTe (FE ≥ 10%) and InP (FE ≥ 25%), in which the selectivity for CO decreased and HCOOH raised at higher negative potentials.

Although these attempts demonstrated some attractive activities, the high overpotentials were still required to obtain these results. In addition, phosphides and arsenides are rank poisonous, which would lead a high risk and raise the cost during the manufacturing process. Alternatively, Centi et al. reported another approach for the PEC reduction of CO₂ to fuel by integrating a photoanode for water dissociation with an electrocatalyst for CO₂ reduction.^{81,82} It shows strong analogies to PEM fuels cells and can take effective advantages of the large technological developments made on these systems. In this regard, it provides more options to utilize noble metals in PEC CO₂ reduction, in which noble metals could not only serve as cocatalysts of photoelectrodes, but also could be employed as the cathodic materials directly. Thus, it opens up a promising strategy towards the study of PEC CO₂ reduction in the future.

1.5 Research motivation and thesis organization

Due to the increasing worldwide demand for fossil fuels and the accompanying excessive emissions of greenhouse gas carbon dioxide, finding a highly efficient, selective and economical approach toward carbon dioxide conversion becomes a great

challenge in realizing an artificial system for sustainable carbon cycle. The approach of photoelectrochemical (PEC) CO₂ reduction is a promising candidate for the future-oriented generation of CO₂ recycling technique. However, so far most of the PEC CO₂ reductions mainly focused on the cathodic half reaction for the directly CO₂ reduction over semiconductor electrodes, such as poisonous phosphides and arsenides. The high overpotentials and limited options of photocathode candidates significantly restrict the research of PEC CO₂ conversion. Furthermore, there are still not enough reports about overall PEC CO₂ conversion.

In this thesis, the main strategy is to construct a PEC device by integrating both the designed cathode and anode for obtaining a highly efficient, selective and low energy consumption overall PEC CO₂ conversion. Firstly, a photocatalytic reduction of CO₂ over wide band-gap semiconductor NaTaO₃ was studied as a preliminary research for the following PEC CO₂ reduction. Various noble metal cocatalysts were loaded on NaTaO₃ to investigate their function in determining the activity and selectivity of photocatalytic CO₂ conversion. Concerning about the straitened circumstances of realizing an overall CO₂ conversion in one single semiconductor photocatalyst, electrocatalytic CO₂ reduction was studied as following step to achieve an efficient and selective CO₂ reusable performance and also reserved as the cathode materials for the PEC CO₂ reduction in the following study. Novel mesoporous palladium-copper bimetallic alloys were prepared for the selective reduction of CO₂ to CO by using metals as catalysts directly, after referring the relations between metal electrocatalysts and their corresponding products. PEC CO₂ reduction was studied to obtain a highly efficient, selective and low energy consumption CO₂ reduction by constructing a PEC device and separating the two half reactions of CO₂ conversion into two different electrode reactions. A ZnO-based NWs composite was fabricated and selected as photoanode for the half reaction of water oxidation within the PEC device. Finally, an

overall PEC CO₂ conversion was investigated by integrating the mesoporous Pd-Cu cathode and ZnO-based NWs arrays photoanode for the selective reduction of CO₂ to CO. Solar light was utilized as an alternative energy source to minimize the electric energy demand during the aqueous CO₂ conversion in our designed PEC device. The effects of both of the cathodic and anodic materials on the overall PEC CO₂ conversion performance were studied. The dissertation is divided into six chapters as follows:

Chapter 1 Introduction

Chapter 1 gave a general introduction of the PEC CO₂ reduction, the interrelated photocatalytic CO₂ reduction and electrochemical CO₂ reduction process as well as the design strategy of PEC construction for the study in this thesis.

Chapter 2 Effect of Noble Metal Cocatalysts on Photocatalytic CO₂ Reduction over NaTaO₃ Nanoparticles

NaTaO₃ was chosen as the target material for the photocatalytic CO₂ reduction, due to its significantly negative conduction band and proper band gap to provide energetic electrons to carry out the CO₂ reduction. Various noble metals (Pt, Au, Cu, Pd, Ru) were loaded on NaTaO₃ as cocatalysts to study the effect of metal cocatalysts on the activity and selectivity. An electron donor (H₂) was introduced into the CO₂ reduction process with water to improve the stability of the CO₂ reduction and to better present the function of metal cocatalysts.

Chapter 3 Mesoporous Palladium-copper Bimetallic Electrodes for Selective Electrocatalytic Reduction of Aqueous CO₂ to CO

Novel mesoporous palladium-copper bimetallic electrocatalysts were fabricated for the selective reduction of CO₂ to CO. Pd and Cu were selected as the alloy components

when concerning about the cost of catalysts and the relations between metal electrocatalysts and their corresponding products. A mesoporous nanostructure was introduced to roughen the catalysts surface and increase the active sites, while the compositional ratios between Pd and Cu were finely controlled for the selective conversion of CO₂ to CO. DFT calculations were carried out to examine the reactive centers within the active sites and absorption/desorption ability of CO₂, COOH* intermediates and CO.

Chapter 4 Design of Hierarchical Nanowire Arrays Photoanodes Based on Carbon Nanotubes and Co₃O₄ Decorated ZnO Composite for the Oxidation Half Reaction of Photoelectrochemical CO₂ Conversion

The half reaction of water oxidation is a very important reaction and to some extent can decide the total activity of CO₂ reduction, according to the previous study of photocatalytic reaction of CO₂. Thus, a hierarchical carbon nanotube (CNT) and Co₃O₄ decorated ZnO nanowire (NW) arrays composite was fabricated as photoanode for the water oxidation reaction via a facile stepwise synthesis strategy. ZnO NWs was chosen as the main photoresponse material due to its tunable alignment and morphology as well as the prospective electronic and optical properties. Co₃O₄ bears the responsibility of efficient O₂ evolution and long durability against chemical- and photo-corrosion, while CNTs possess unique electrical and optical properties in photovoltaic, thus were selected as the cocatalysts of ZnO to obtain a highly enhanced activity for PEC water oxidation.

Chapter 5 Design of Photoelectrochemical Device for the Selective Conversion of CO₂ to CO Using Mesoporous Palladium-Copper Bimetallic Cathode and Hierarchical ZnO-Based Nanowire Arrays Photoanode

In the last chapter, an attempt study for a highly efficient, selective and low energy consumption PEC CO₂ reaction was carried out in a two-electrode cell system. The PEC device was constructed with a metal cathode and n-type semiconductor photoanode. The previous studied mesoporous palladium-copper alloy was employed as cathode for selective reduction of CO₂ to CO. And ternary hierarchical ZnO-based NWs arrays composite was used as photoanode for the other half reaction of water oxidation. The overall PEC CO₂ conversion activity was an integrated performance and it was determined by both of the cathodic and anodic materials.

Chapter 6 General Conclusion and Future Prospects

This chapter makes an overall summary and conclusions of the results in this dissertation work. The prospects for further study and future plan were also presented in this chapter.

References

1. *Global Climate Change -- Earth Science Communications Team at NASA's Jet Propulsion Laboratory / California Institute of Technology (data from NOAA)*, 2013.
2. *BP Statistical Review of World Energy June 2015*, 2015.
3. *CLIMATE CHANGE 2014: Synthesis Report*. .
4. *Carbon Cycle 2.0*, A U.S. Department of Energy National Laboratory Operated by the University of California.
5. G. Centi and S. Perathoner, *Catal. Today.*, 2009, **148**, 191-205.
6. D. Pakhare and J. Spivey, *Chem. Soc. Rev.*, 2014, **43**, 7813-7837.
7. J. H. Bitter, K. Seshan and J. A. Lercher, *J. Catal.*, 1998, **176**, 93-101.

8. M. M. V. M. Souza, D. A. G. Aranda and M. Schmal, *J. Catal.*, 2001, **204**, 498-511.
9. A. Fujishima and K. Honda, *Nature*, 1972, **238**, 37-38.
10. W. Tu, Y. Zhou and Z. Zou, *Adv. Mater.*, 2014, **26**, 4607-4626.
11. Q. Liu, Y. Zhou, J. Kou, X. Chen, Z. Tian, J. Gao, S. Yan and Z. Zou, *J. Am. Chem. Soc.*, 2010, **132**, 14385-14387.
12. C. W. Li, J. Ciston and M. W. Kanan, *Nature*, 2014, **508**, 504-507.
13. K. Nakata, T. Ozaki, C. Terashima, A. Fujishima and Y. Einaga, *Angew. Chem. Int. Ed.*, 2014, **53**, 871-874.
14. B. Kumar, M. Llorente, J. Froehlich, T. Dang, A. Sathrum and C. P. Kubiak, *Annu. Rev. Phys. Chem.*, 2012, **63**, 541-569.
15. M. Halmann, *Nature*, 1978, **275**, 115-116.
16. N. Sutin, C. Creutz and E. Fujita, *Comments Inorg. Chem.*, 1997, **19**, 67-92.
17. J.-M. Lehn and R. Ziessel, *Proc. Natl. Acad. Sci. U.S.A.*, 1982, **79**, 701-704.
18. A. J. Morris, G. J. Meyer and E. Fujita, *Acc. Chem. Res.*, 2009, **42**, 1983-1994.
19. H. Ishida, T. Terada, K. Tanaka and T. Tanaka, *Inorg. Chem.*, 1990, **29**, 905-911.
20. H. Tong, S. Ouyang, Y. Bi, N. Umezawa, M. Oshikiri and J. Ye, *Adv. Mater.*, 2012, **24**, 229-251.
21. T. Inoue, A. Fujishima, S. Konishi and K. Honda, *Nature*, 1979, **277**, 637-638.
22. S. C. Yan, S. X. Ouyang, J. Gao, M. Yang, J. Y. Feng, X. X. Fan, L. J. Wan, Z. S. Li, J. H. Ye, Y. Zhou and Z. G. Zou, *Angew. Chem. Int. Ed.*, 2010, **49**, 6400-6404.
23. N. Zhang, S. Ouyang, P. Li, Y. Zhang, G. Xi, T. Kako and J. Ye, *Chem. Commun.*, 2011, **47**, 2041-2043.
24. S. Yan, L. Wan, Z. Li and Z. Zou, *Chem. Commun.*, 2011, **47**, 5632-5634.
25. P. Li, S. Ouyang, Y. Zhang, T. Kako and J. Ye, *J. Mater. Chem. A*, 2013, **1**, 1185-1191.
26. P. Li, H. Xu, L. Liu, T. Kako, N. Umezawa, H. Abe and J. Ye, *J. Mater. Chem. A*,

- 2014, **2**, 5606-5609.
27. P. Li, S. Ouyang, G. Xi, T. Kako and J. Ye, *J. Phys. Chem. C*, 2012, **116**, 7621-7628.
28. S. N. Habisreutinger, L. Schmidt-Mende and J. K. Stolarczyk, *Angew. Chem. Int. Ed.*, 2013, **52**, 7372-7408.
29. H. Xu, S. Ouyang, L. Liu, D. Wang, T. Kako and J. Ye, *Nanotechnology*, 2014, **25**, 165402.
30. T. Wang, X. Meng, P. Li, S. Ouyang, K. Chang, G. Liu, Z. Mei and J. Ye, *Nano Energy*, 2014, **9**, 50-60.
31. R. Nakamura and Y. Nakato, *J. Am. Chem. Soc.*, 2004, **126**, 1290-1298.
32. Q. Kang, T. Wang, P. Li, L. Liu, K. Chang, M. Li and J. Ye, *Angew. Chem. Int. Ed.*, 2015, **54**, 841-845.
33. H. Tsuneoka, K. Teramura, T. Shishido and T. Tanaka, *J. Phys. Chem. C*, 2010, **114**, 8892-8898.
34. K. Teramura, T. Tanaka, H. Ishikawa, Y. Kohno and T. Funabiki, *J. Phys. Chem. B*, 2004, **108**, 346-354.
35. J. Yang, D. Wang, H. Han and C. Li, *Acc. Chem. Res.*, 2013, **46**, 1900-1909.
36. H. Zhou, J. Guo, P. Li, T. Fan, D. Zhang and J. Ye, *Sci. Rep.*, 2013, **3**, 1667.
37. J. Lee, Y. Kwon, R. L. Machunda and H. J. Lee, *Chem. Asian J.*, 2009, **4**, 1516-1523.
38. A. S. Agarwal, Y. Zhai, D. Hill and N. Sridhar, *ChemSusChem.*, 2011, **4**, 1301-1310.
39. J. Qiao, Y. Liu, F. Hong and J. Zhang, *Chem. Soc. Rev.*, 2014, **43**, 631-675.
40. S. D. Sullivan and K. B. Weiss, *Allergy*, 1993, **48**, 146-152.
41. Y. Hori, H. Wakebe, T. Tsukamoto and O. Koga, *Electrochim. Acta*, 1994, **39**, 1833-1839.

42. Y. Hori, in *Modern Aspects of Electrochemistry*, eds. C. Vayenas, R. White and M. Gamboa-Aldeco, Springer New York, 2008, vol. 42, ch. 3, pp. 89-189.
43. M. Azuma, K. Hashimoto, M. Hiramoto, M. Watanabe and T. Sakata, *J. Electrochem. Soc.*, 1990, **137**, 1772-1778.
44. S. Ikeda, T. Takagi and K. Ito, *Bull. Chem. Soc. Jpn.*, 1987, **60**, 2517-2522.
45. Y. Tomita, S. Teruya, O. Koga and Y. Hori, *J. Electrochem. Soc.*, 2000, **147**, 4164-4167.
46. W. Zhu, R. Michalsky, Ö. Metin, H. Lv, S. Guo, C. J. Wright, X. Sun, A. A. Peterson and S. Sun, *J. Am. Chem. Soc.*, 2013, **135**, 16833-16836.
47. Y. Chen, C. W. Li and M. W. Kanan, *J. Am. Chem. Soc.*, 2012, **134**, 19969-19972.
48. H. Mistry, R. Reske, Z. Zeng, Z.-J. Zhao, J. Greeley, P. Strasser and B. R. Cuenya, *J. Am. Chem. Soc.*, 2014, **136**, 16473-16476.
49. J. Greeley, T. F. Jaramillo, J. Bonde, I. Chorkendorff and J. K. Nørskov, *Nat. Mater.*, 2006, **5**, 909-913.
50. A. A. Peterson, F. Abild-Pedersen, F. Studt, J. Rossmeisl and J. K. Nørskov, *Energy Environ. Sci.*, 2010, **3**, 1311-1315.
51. K. P. Kuhl, E. R. Cave, D. N. Abram and T. F. Jaramillo, *Energy Environ. Sci.*, 2012, **5**, 7050-7059.
52. Y. Hori, I. Takahashi, O. Koga and N. Hoshi, *J. Phys. Chem. B*, 2002, **106**, 15-17.
53. R. L. Cook, R. C. MacDuff and A. F. Sammells, *J. Electrochem. Soc.*, 1988, **135**, 1320-1326.
54. K. Manthiram, B. J. Beberwyck and A. P. Alivisatos, *J. Am. Chem. Soc.*, 2014, **136**, 13319-13325.
55. J. Christophe, T. Doneux and C. Buess-Herman, *Electrocatalysis*, 2012, **3**, 139-146.
56. S. Rasul, D. H. Anjum, A. Jedidi, Y. Minenkov, L. Cavallo and K. Takanabe, *Angew. Chem. Int. Ed.*, 2015, **54**, 2146-2150.

57. D. Kim, J. Resasco, Y. Yu, A. M. Asiri and P. Yang, *Nat Commun*, 2014, **5**.
58. S. Siahrostami, A. Verdaguer-Casadevall, M. Karamad, D. Deiana, P. Malacrida, B. Wickman, M. Escudero-Escribano, E. A. Paoli, R. Frydendal, T. W. Hansen, I. Chorkendorff, I. E. L. Stephens and J. Rossmeisl, *Nat. Mater.*, 2013, **12**, 1137-1143.
59. Y. Hori, A. Murata, R. Takahashi and S. Suzuki, *J. Chem. Soc., Chem. Commun.*, 1988, 17-19.
60. M. Gattrell, N. Gupta and A. Co, *J. Electroanal. Chem.*, 2006, **594**, 1-19.
61. S. Kaneco, N.-h. Hiei, Y. Xing, H. Katsumata, H. Ohnishi, T. Suzuki and K. Ohta, *Electrochim. Acta*, 2002, **48**, 51-55.
62. K. Hara, A. Tsuneto, A. Kudo and T. Sakata, *J. Electrochem. Soc.*, 1994, **141**, 2097-2103.
63. J. D. Figueroa, T. Fout, S. Plasynski, H. McIlvried and R. D. Srivastava, *Int. J. Greenhouse Gas Control*, 2008, **2**, 9-20.
64. J. L. DiMeglio and J. Rosenthal, *J. Am. Chem. Soc.*, 2013, **135**, 8798-8801.
65. W. H. Brattain and C. G. B. Garrett, *Bell Syst. Tech. J.*, 1955, **34**, 129-176.
66. H. Gerischer, *J. Electrochem. Soc.*, 1966, **113**, 1174-1182.
67. M. Gratzel, *Nature*, 2001, **414**, 338-344.
68. S. Licht, O. Khaselev, P. A. Ramakrishnan, T. Soga and M. Umeno, *J. Phys. Chem. B*, 1998, **102**, 2536-2545.
69. T. Hisatomi, J. Kubota and K. Domen, *Chem. Soc. Rev.*, 2014, **43**, 7520-7535.
70. K. Sivula, *J. Phys. Chem. Lett.*, 2013, **4**, 1624-1633.
71. M. G. Walter, E. L. Warren, J. R. McKone, S. W. Boettcher, Q. Mi, E. A. Santori and N. S. Lewis, *Chem. Rev.*, 2010, **110**, 6446-6473.
72. I. Taniguchi, B. Aurian-Blajeni and J. O. M. Bockris, *Electrochim. Acta*, 1984, **29**, 923-932.
73. K. Hirota, D. A. Tryk, T. Yamamoto, K. Hashimoto, M. Okawa and A. Fujishima, *J.*

- Phys. Chem. B*, 1998, **102**, 9834-9843.
74. Y. Nakamura, R. Hinogami, S. Yae and Y. Nakato, in *Studies in Surface Science and Catalysis*, eds. M. A. K. I. S. Y. T. Inui and T. Yamaguchi, Elsevier, 1998, vol. Volume 114, pp. 565-568.
75. S. Kaneco, H. Katsumata, T. Suzuki and K. Ohta, *Chem. Eng. J.*, 2006, **116**, 227-231.
76. W. M. Sears and S. R. Morrison, *J. Phys. Chem.*, 1985, **89**, 3295-3298.
77. E. E. Barton, D. M. Rampulla and A. B. Bocarsly, *J. Am. Chem. Soc.*, 2008, **130**, 6342-6344.
78. L. Junfu and C. Baozhu, *J. Electroanal. Chem.*, 1992, **324**, 191-200.
79. C. Amatore and J. M. Saveant, *J. Am. Chem. Soc.*, 1981, **103**, 5021-5023.
80. H. Yoneyama, K. Sugimura and S. Kuwabata, *J. Electroanal. Chem.*, 1988, **249**, 143-153.
81. G. Centi, S. Perathoner, G. Wine and M. Gangeri, *Green Chem.*, 2007, **9**, 671-678.
82. G. Centi and S. Perathoner, *Top. Catal.*, 2009, **52**, 948-961.

Chapter 2 Effect of Noble Metal Cocatalysts on Photocatalytic CO₂ Reduction over NaTaO₃ Nanoparticles

2.1 Introduction

Semiconductor photocatalysis appears to be a promising CO₂ reusable approach, since the Honda-Fujishima effect has been discovered by the early 1970s.^{1, 2} Generally, a photocatalytic CO₂ reduction over semiconductors can only utilize solar lights as energy source to convert CO₂ to usable fuels without applying any other energy. In the previous investigation of semiconductor photocatalytic CO₂ reduction, only a limited number of wide band-gap semiconductors have exhibited photocatalytic activities with various reducing outcomes.³ The semiconductors must possess a negative enough conduction band (CB) to provide enough energy of the photogenerated electrons to overcome the activation barrier and to promote the multiple-electron reaction during the CO₂ reduction process.^{4, 5}

NaTaO₃ has been reported by Kudo et al. as one of the best pure water splitting photocatalysts.⁶⁻⁸ It possesses a significantly negative CB and wide band gap and thus should be a promising photocatalyst in CO₂ reduction, although there are few reports about it. In addition to the band structure, the reactivity of the two half reaction significantly affect the overall performance of photocatalytic CO₂ reduction with water. Since the noble metal cocatalysts could determine the activity and selectivity of the half reaction of CO₂ reduction,^{9, 10} while a smooth holes consumption within the half reaction of water oxidation have an extreme influence on the stability of the total reaction.¹¹

In this chapter, NaTaO₃ was selected as the photocatalyst to carry out the CO₂ reduction as a preliminary research for the following PEC CO₂ reduction. An electron donor (H₂ gas) was introduced to the reaction system to verify the peroxide intermediates mechanism during the water oxidation reaction and to enhance the activity as well as the stability of the CO₂ reduction. On the other hand, the effect of different noble metal cocatalysts (Pt, Au, Cu, Pd, Ru) for CO₂ photoreduction was studied with and without the electron donor, respectively.

2.2 Experimental methods

2.2.1 Photocatalysts preparation

The NaTaO₃ was synthesized via a typical furfural alcohol derived polymerization–oxidation (FAPO) process.¹²⁻¹⁴ First, 1.61 g of (C₂H₅O)₅Ta and 0.29 g of C₂H₅ONa were added into 15 mL of 2-methoxyethanol and stirred at room temperature to form a clear colloid. After that, 2.0 g of P-123 (M_w = 5800) dissolved in 30 mL of furfuryl alcohol was added. Next, the mixture was stirred for 60 min and then heated to 95°C with a rate of 1°C·min⁻¹ and maintained at this temperature for 120 h in air to form a black solid polymer. Finally, the black solid was oxidized in air at 500°C for 10 h, and a white powder product was obtained.

The loading process was performed by a photocatalytic reduction method. 0.5wt % of Pt, Au, Cu, Pd and Ru co-catalysts were photodeposited on the NaTaO₃ catalyst by adding a calculated amount of H₂PtCl₆, HAuCl₄, Cu(NO₃)₂, Pd(O₂CCH₃)₂ and RuCl₃ solution into the reaction solution, respectively. The NaTaO₃ powder (0.2 g) was dispersed by using a magnetic stirrer in CH₃OH aqueous solution (230 mL of distilled water + 50 mL of CH₃OH) in a Pyrex cell

with a side window. The reactant solution was irradiated by a 300 W UV-enhanced Xe lamp ($\lambda > 200\text{nm}$) for 4 h. The H_2 evolution was measured with an online gas chromatograph (GC-8A, Shimadzu) with a thermal conductivity detector (TCD) according to the standard curve. After H_2 evolution achieving a stable linear growth, the resulting NaTaO_3 photocatalyst with cocatalysts was collected after heating and drying in air overnight. The powder was then dried in vacuum at $300\text{ }^\circ\text{C}$ for 3 h to remove organic compounds adsorbed on the surface of the catalyst. The obtained samples with different cocatalysts loaded were further tested for the photoactivity of CO_2 reduction.

2.2.2 Sample characterization

The crystal structure of NaTaO_3 powder was determined with an X-ray diffractometer (X'Pert Powder, PANalytical B.V., Netherlands) with $\text{Cu-K}\alpha$ radiation. Scanning electron microscopy images were recorded with a HITACHI S-4800 field emission scanning electron microscopy. Transmission electron microscopy images were recorded with a field emission transmission electron microscope (2100F, JEOL Co., Japan) operated at 200 kV. The diffuse reflection spectra were measured with an integrating sphere equipped UV–visible recording spectrophotometer (UV-2600, Shimadzu Co., Japan) using BaSO_4 as reference and the optical absorptions were converted from the reflection spectra according to Kubelka-Munk equation. The specific surface areas were determined with a surface-area analyzer (BEL Sorp-II mini, BEL Japan Co., Japan) by the Brunauer–Emmett–Teller (BET) method. X-ray Photoelectron Spectroscopy (XPS) experiments were performed in type Theta probe (ULVAC-PHI, Japan)

using monochromatized Al K α at 1.4×0.1 mm 100 W (20 kV, 5 mA) and the peak positions were internally referenced to the C 1s peak at 285.0 eV.

2.2.3 CO₂ photoreduction

The CO₂ photoreduction experiments were carried out in a gas-closed circulation system. The NaTaO₃ powder as well as 0.5 wt% cocatalysts loaded samples (0.07 g) were located in a Pyrex reaction cell equipped with an upside window, respectively. In the case of using H₂O as the reducing agent, 3 mL of distilled water was added into the gas-closed reaction system. Then, the whole system was evacuated and filled with 80 kPa of pure CO₂ gas. In the case of using H₂ gas electron donors, 3 mL of distilled water was also added into the gas-closed reaction system firstly, and then the whole system was evacuated. Finally, the filled atmosphere was change to 40 kPa of pure CO₂ gas and 40 kPa of pure H₂ gas. The light source was a 300 W UV-enhanced Xe lamp ($\lambda > 200\text{nm}$) without filter. The CO, CO₂ and organic products were sampled and measured with a gas chromatograph (GC-14B, Shimadzu) equipped with a flame ionization detector (FID) according to the standard curves. The GC column is Porapak Q-methanizer for CO and CO₂ measurement (CH=1), PEG1000 for organic products measurement (CH=2). The H₂ evolution was measured with an online gas chromatograph (GC-8A, Shimadzu) with a TCD detector according to the standard curve. The GC column is 5A molecular sieve.

2.3 Results and discussions

2.3.1 Characteristics of NaTaO₃ samples

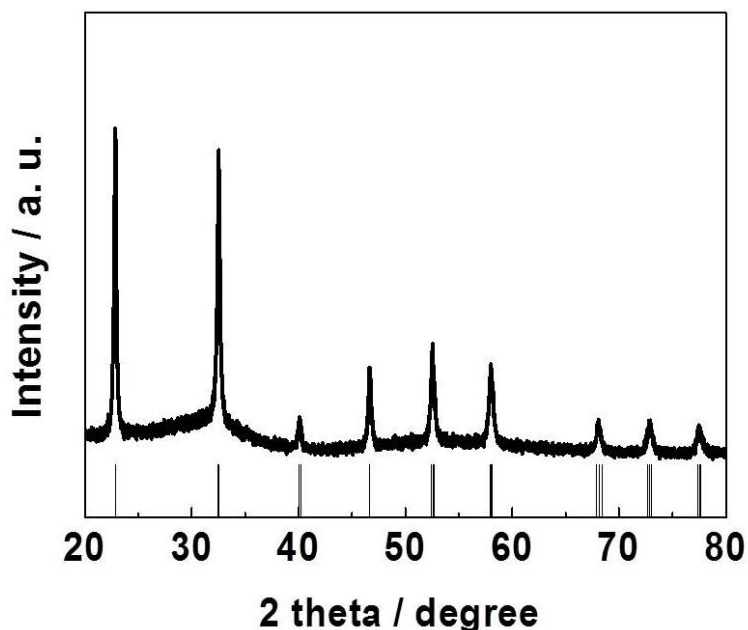


Fig. 2.1 XRD pattern of the as-prepared NaTaO₃ sample.

The crystallographic phases of the NaTaO₃ samples were examined by X-ray diffraction (XRD) as shown in Fig. 2.1. The NaTaO₃ prepared through the FAPO route crystallized in a monoclinic system with the space group of P2/m, which could be well indexed to the JCPDS database card (JCPDS-01-074-2477). The morphology of the as-prepared sample was characterized by scanning electron microscope (SEM) and transmission electron microscopy (TEM) as shown in Fig. 2.2. According to both of the SEM image (Fig. 2.2a) and TEM image (Fig. 2.2b), the NaTaO₃ crystallite grew into cuboid particles, in which this morphology should be attributed to the effect of P123 and the furfural alcohol polymerization.¹³ The average size of the NaTaO₃ sample is about 20 ~ 30 nm.

Furthermore, two sets of monoclinic fringes with lattice spacing of 0.390 nm and 0.275 nm can be observed from the HRTEM image in the insert of Fig. 2.2b, corresponding to the (100) and (011) planes of monoclinic NaTaO₃, respectively. This result is in agreement with the XRD pattern and further confirms the successful preparation of monoclinic NaTaO₃.¹⁵

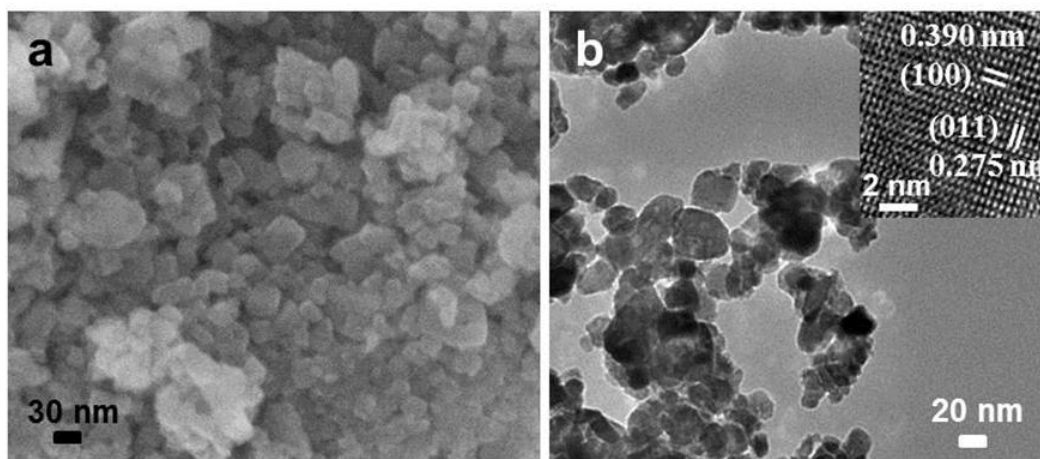


Fig. 2.2 a) SEM image of NaTaO₃ sample; b) TEM image of NaTaO₃ sample, the insert shows HRTEM image.

UV-visible absorption spectrum of the NaTaO₃ nanoparticles is shown in Fig. 2.3, with an intense absorption with steep edge in the UV region. The band gap (E_g) of NaTaO₃ was determined by the following equation¹⁵

$$(\alpha h\nu)^n = A(h\nu - E_g)$$

in which α , ν , A , and E_g are the absorption coefficient, light frequency, proportionality constant and band gap, respectively. The value of index n depends on the property of materials, in which $n = 2$ for the direct band-gap materials and $n = 1/2$ for the indirect band-gap materials. In the case of NaTaO₃, the index is $1/2$ according to the previous report⁶ and the band gap is determined to be 4.2 eV as shown in the inset of Fig. 2.3.

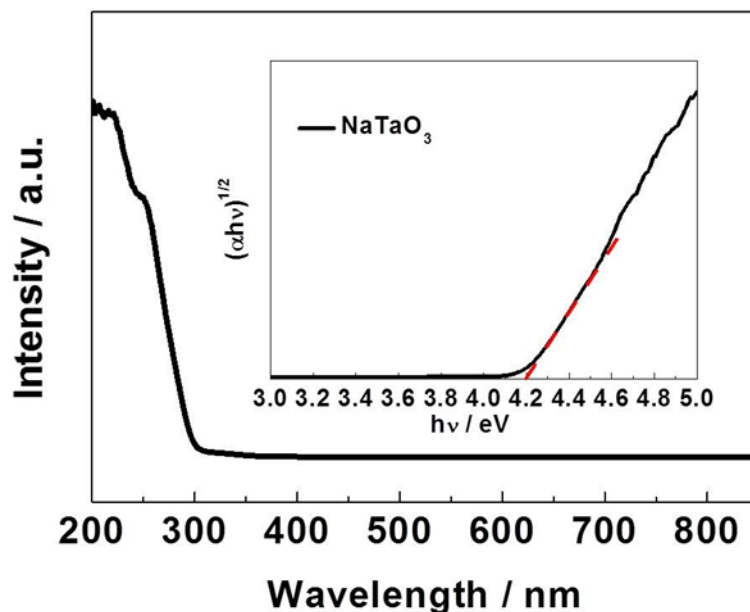


Fig. 2.3 UV-vis absorption spectrum of NaTaO₃ sample and the inset is the corresponding $(\alpha h\nu)^{1/2} \sim h\nu$ curve.

2.3.2 The photocatalytic CO₂ reduction with H₂O

The photocatalytic properties of the as-prepared NaTaO₃ were estimated by photoreduction of gaseous phase CO₂ under the irradiation of a 300 W UV-enhanced Xe lamp. Fig. 2.4a and Fig. 2.4b exhibit the results of CO₂ reduction over different noble metal (Pt, Au, Cu, Pd, Ru) loaded NaTaO₃ using water as the reducing agent. All the samples showed certain abilities, where CH₄ and CO presented to be the two main carbon products with CO appears more dominant. The total productivities were listed in Table 2.1. The loaded noble metal cocatalysts mainly benefited H₂ evolution in this reaction condition (CO₂+H₂O), because H₂ evolution is a highly preferred competing reaction. Moreover, the CO₂ reduction reactions exhibited not linear growth of the products evolution for both of the desired carbon products. The bent curves indicate an unstable reactivity of CO₂ reduction reaction for all the samples,

which also often puzzles the study of photocatalytic CO₂ reduction over oxide semiconductors using water as the reducing agent.^{3, 16}

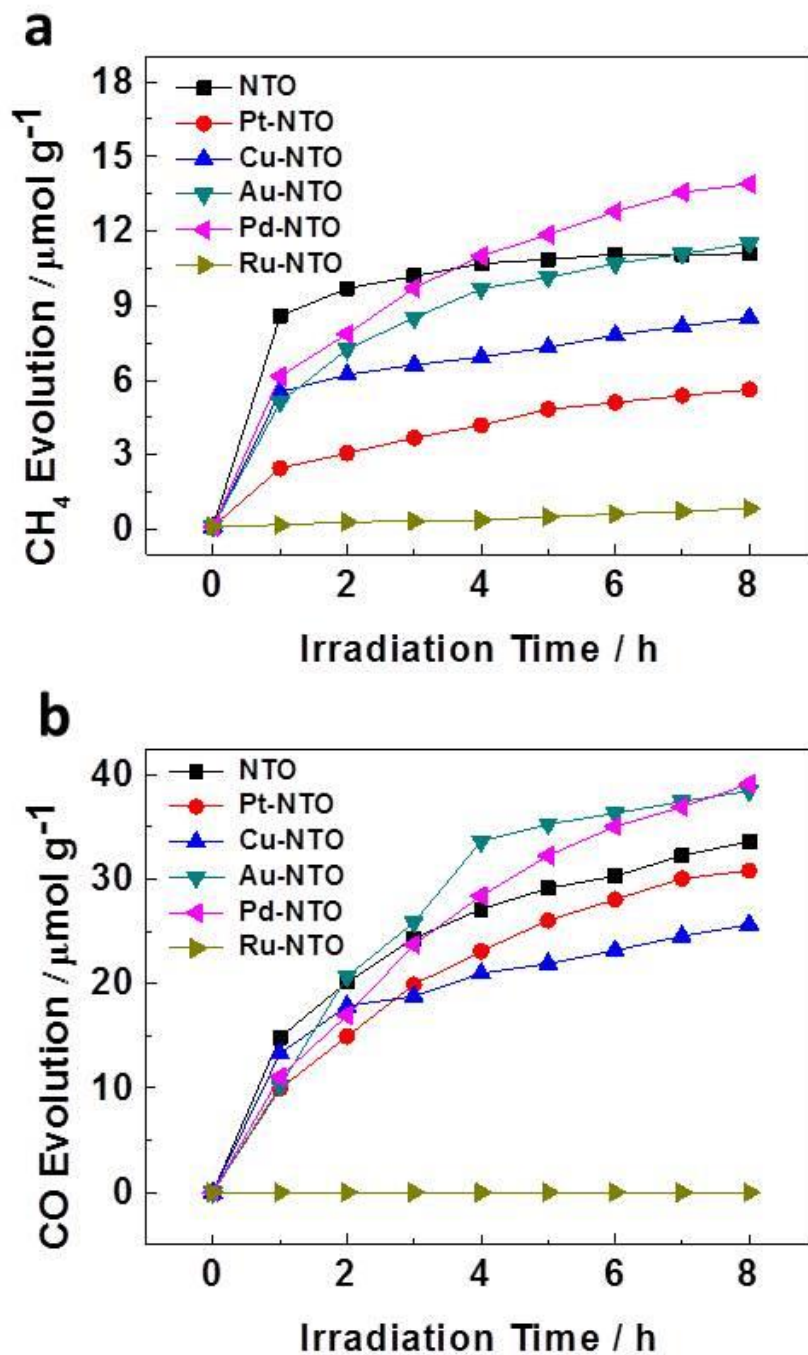
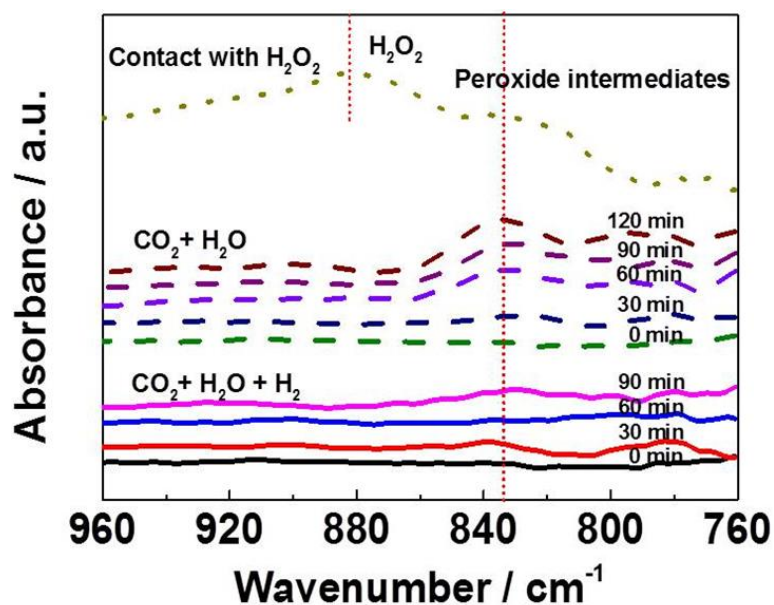


Fig. 2.4 Gaseous product generation over 0.5 wt% co-catalysts loaded NaTaO₃ in H₂O and CO₂ atmosphere: a) CH₄, b) CO.

Table 2.1 Productivities of the series of NaTaO₃ using water as the reducing agent.

Materials	CH ₄ productivity /	CO productivity /	H ₂ productivity /
	$\mu\text{mol g}^{-1}\text{h}^{-1}$	$\mu\text{mol g}^{-1}\text{h}^{-1}$	$\mu\text{mol g}^{-1}\text{h}^{-1}$
	CO ₂ +H ₂ O	CO ₂ +H ₂ O	CO ₂ +H ₂ O
NaTaO ₃	1.39	6.49	1.36
Pt-NaTaO ₃	0.70	5.95	80.23
Cu-NaTaO ₃	1.07	4.95	38.94
Au-NaTaO ₃	1.43	7.43	53.10
Pd-NaTaO ₃	1.73	7.56	76.43
Ru-NaTaO ₃	0.11	0.07	6.82

**Fig. 2.5** In situ FTIR spectra of NaTaO₃ during the CO₂ reduction process.

It is noticeable that O₂ could also not be detected as the product of water oxidation. Thus, an obstructive O₂ release process should be the main reason for

the above phenomena. It has been reported that some peroxide intermediates would be formed at the oxide semiconductor surface during the oxygen photoevolution reaction from water.¹¹ In situ FTIR spectra were examined to confirm the existence of these peroxide intermediates during the photocatalytic CO₂ reduction process over NaTaO₃ as shown in Fig. 2.5.

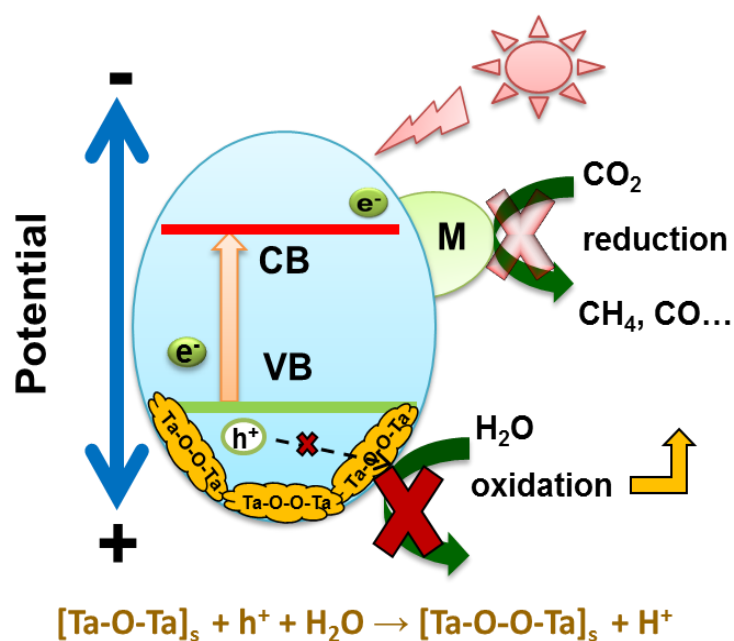


Fig. 2.6 Schematic model of peroxide intermediates formation and accumulation at the surface of NaTaO₃.

By referring the method reported in the literature, NaTaO₃ film was firstly exposed to a 30% H₂O₂ aqueous solution to position the peak of peroxide intermediates. Two new peaks emerged at 834 cm⁻¹ and 883 cm⁻¹ (dot line) and could be considered as the peaks of peroxide intermediates and H₂O₂, respectively. Then the CO₂ reduction was investigated by in situ FTIR spectra with capsuling the NaTaO₃ samples with CO₂ gas and H₂O within a sealed sample compartment. As the dash line shown, during the CO₂ reduction process,

the peroxide intermediates were confirmed to form and accumulate with the time at the surface of NaTaO₃. The schematic model in Fig. 2.6 could describe this process. These accumulated peroxide intermediates significantly hindered the photogenerated holes to oxidize water. Thus, the recombination of electrons and holes increased, and so that reflects on a decreased photocatalytic activity.

2.3.3 The photocatalytic CO₂ reduction with H₂O in the presence of electron donor H₂

Table 2.2 Productivities of the series of NaTaO₃ with and without the electron donor H₂.

Materials	CH ₄ productivity / μmol g ⁻¹ h ⁻¹		CO productivity / μmol g ⁻¹ h ⁻¹		H ₂ productivity / μmol g ⁻¹ h ⁻¹	
	CO ₂ +H ₂ O	CO ₂ +H ₂ O+H ₂	CO ₂ +H ₂ O	CO ₂ +H ₂ O+H ₂	CO ₂ +H ₂ O	CO ₂ +H ₂ O+H ₂
NaTaO ₃	1.39	2.07	6.49	10.10	1.36	N/A
Pt-NaTaO ₃	0.70	1.13	5.95	139.1	80.23	N/A
Cu-NaTaO ₃	1.07	3.71	4.95	16.23	38.94	N/A
Au-NaTaO ₃	1.43	2.44	7.43	14.47	53.10	N/A
Pd-NaTaO ₃	1.73	8.61	7.56	9.71	76.43	N/A
Ru-NaTaO ₃	0.11	51.8	0.07	2.16	6.82	N/A

In order to eliminate the hamper of peroxide intermediates and realize a stable reduction of CO_2 , an electron donor (H_2 gas) was introduced to the reaction system to release the peroxides. All the samples exhibit obvious promotions of the catalytic activity compared with the counterparts only using H_2O as the reducing agent to react with CO_2 as summarized in Table 2.2. Fig. 2.7a and 2.7b show the results of CO_2 reduction with different noble metal loaded NaTaO_3 samples in the presence of H_2O , CO_2 and H_2 . Almost linear curves indicate that enhanced stabilities and activities of the CO_2 reduction are obtained over the catalysts. The CO_2 reduction was also investigated by the in situ FTIR spectra in the presence of electron donor H_2 . As the solid lines in Fig. 2.5 shown, there is almost no accumulation of the peroxides in the presence of electron donor H_2 . Thus, it can be concluded that the peroxide intermediates are effectively reduced by H_2 and so that a stable reduction of CO_2 are observed.

An isotope experiment within a D_2O , CO_2 and H_2 atmosphere was carried out to distinguish the hydrogen source between water (D_2O) and H_2 of the produced methane. As shown in Fig. 2.8, CD_4 is the dominant methane products initially, which illustrates clearly that the hydrogen in methane comes from water (D_2O). With the reaction proceeded after several hours, some CD_3H and CD_2H_2 can be observed among the methane products (Fig. 2.8b). It can be deduced that the protium atoms should mainly derive from the normal water (H_2O) reduced from peroxides at NaTaO_3 surface by H_2 . Thus, it is confirmed that the direct hydrogen source of the CO_2 reduction is still water, but not the H_2 gas introduced as the electron donor. H_2 promotes the CO_2 reduction reaction by a successful conversion of peroxide intermediates (O_2^*) into water rather than directly reduces CO_2 to CH_4 as the schematic model shows in Fig. 2.9. This is because that the requisite active hydrogen to react with CO_2 in a photocatalytic process should be

atomic hydrogen rather than molecular hydrogen. The hydrogenation reaction between molecular hydrogen and CO_2 must climb over an energy barrier to push forward,^{17, 18} where the requirement could not be met in this work. The atomic hydrogen is activated from other hydrogen sources (water in this work), although there are hydrogen molecules in the system.¹⁹

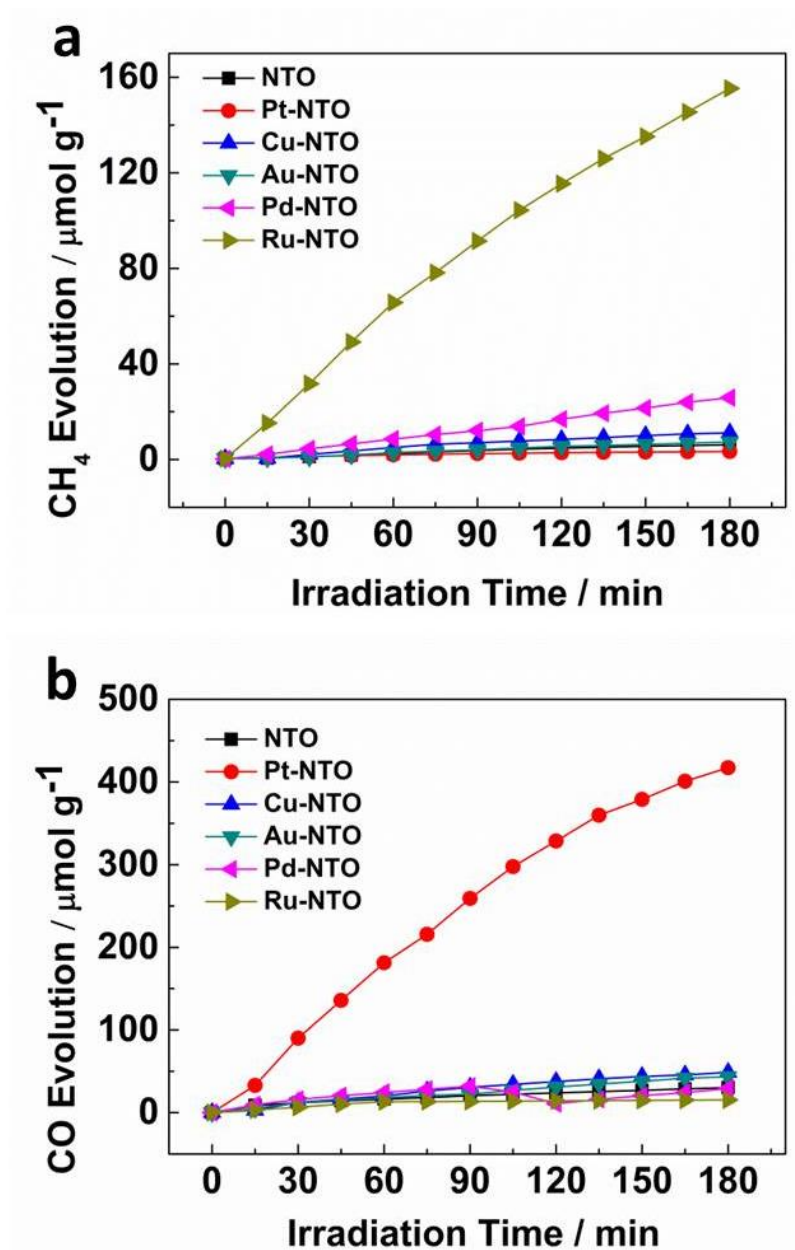
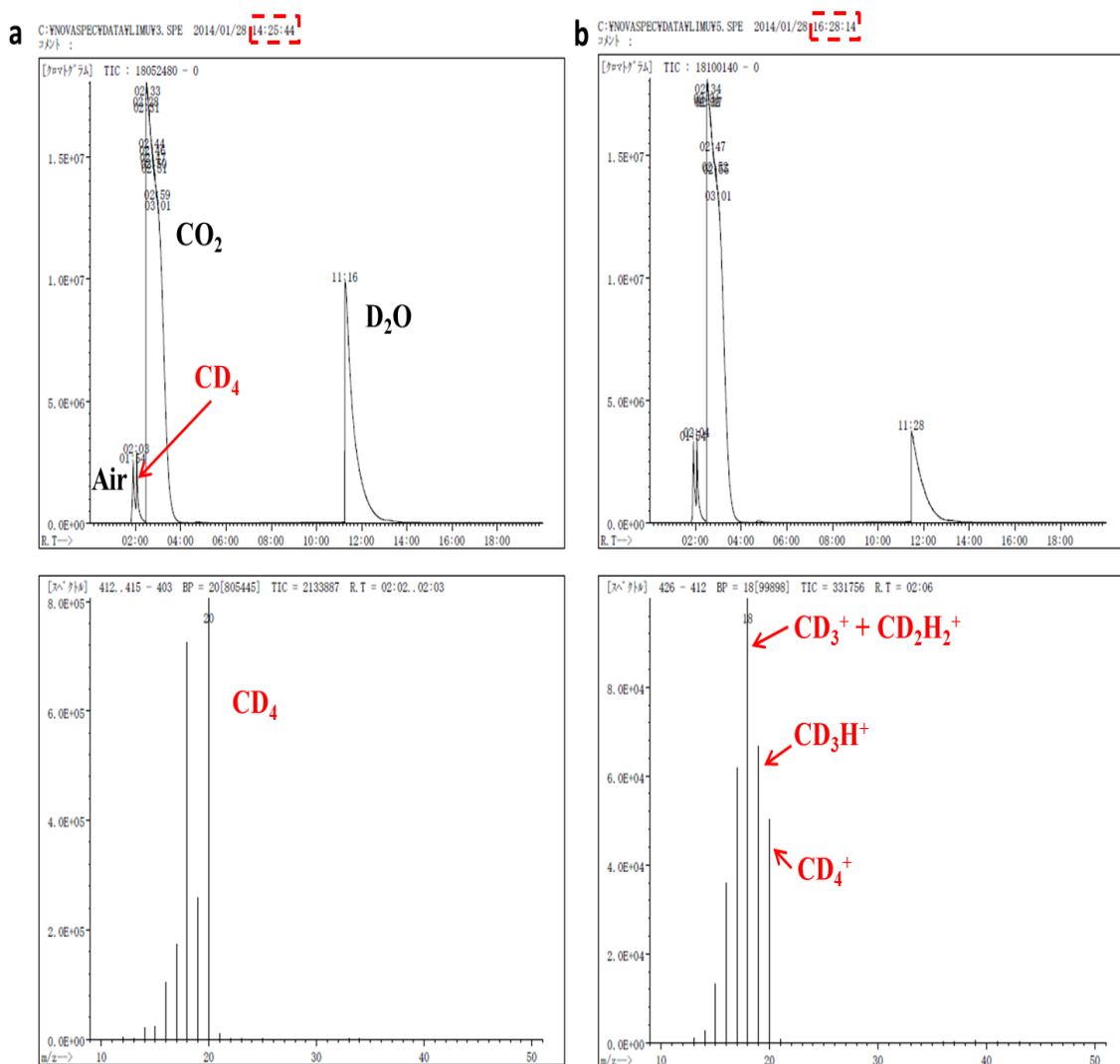


Fig. 2.7 Gaseous product generation over 0.5 wt% co-catalysts loaded NaTaO_3 in CO_2 , H_2O and H_2 atmosphere: a) CH_4 , b) CO .



Initial period (a): $\text{CO}_2 + \text{D}_2\text{O} \rightarrow \text{CD}_4 + \text{O}_2^*$



After several hours (b): $\text{CO}_2 + \text{D}_2\text{O} + \text{H}_2\text{O} \rightarrow \text{CD}_3\text{H} + \text{CD}_2\text{H}_2 + \text{O}_2^*$

O_2^* : peroxide intermediates

Fig. 2.8 Original data of GC-MS spectra of photocatalytic CO₂ reduction products over Ru-NaTaO₃ under H₂ atmosphere in the present of D₂O: (a) Sampling at the initial period of the reaction, (b) sampling several hours after the reaction start.

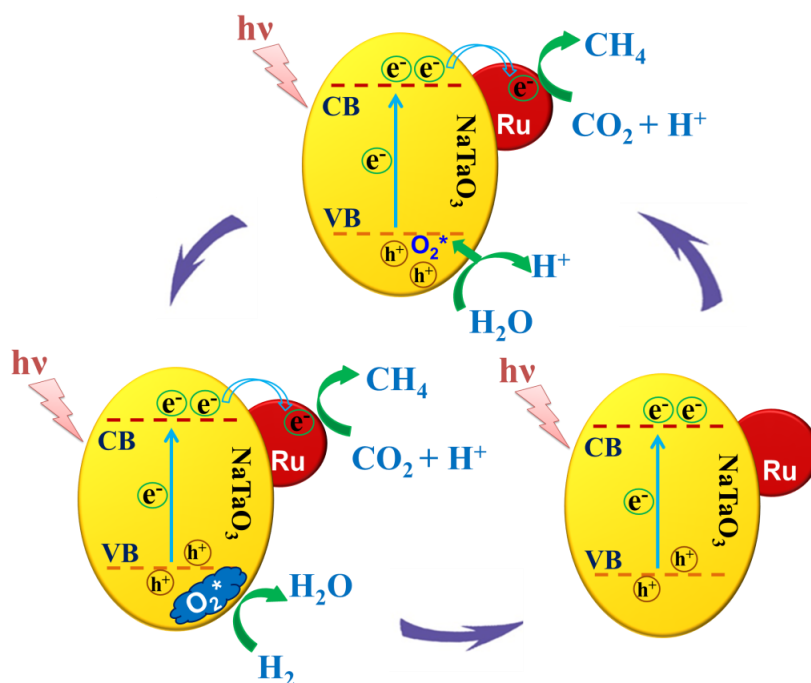


Fig. 2.9 Schematic model of a proposed reaction process over Ru-NaTaO₃ in CO₂, H₂O and H₂ atmosphere.

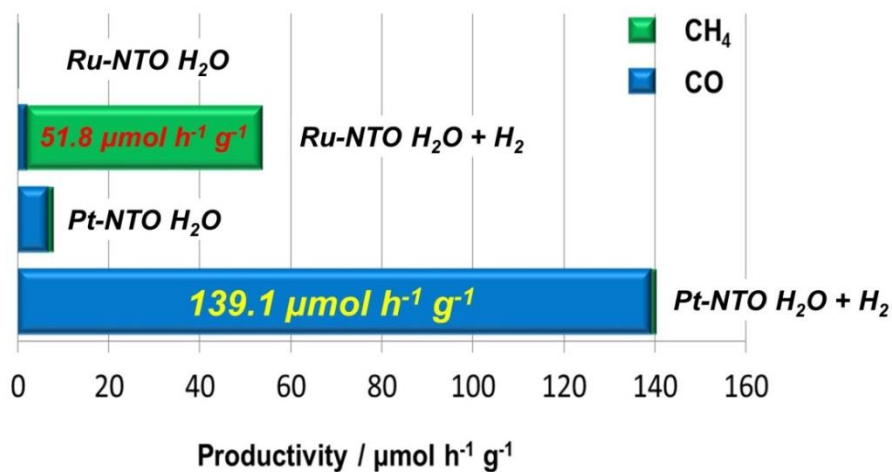


Fig. 2.10 Productivity with and without H₂ over Ru-NaTaO₃ and Pt-NaTaO₃.

In the point view of cocatalyst, except for Ru and Pt, other cocatalysts did not exhibit a pronounced activity enhancement and selectivities of CO₂ reduction due

to their natural properties as shown in Table 2.2. Ru-NaTaO₃ (CH₄ 51.8 μmol h⁻¹ g⁻¹) and Pt-NaTaO₃ (CO 139.1 μmol h⁻¹ g⁻¹) exhibited the best activities and products selectivity over the series (Fig. 2.7a and Fig. 2.7b). The CH₄ or CO versus total carbon products (CH₄ + CO) ratio is about 0.96 for Ru-NaTaO₃ and 0.99 for Pt-NaTaO₃ as shown in Fig. 2.10. These results accord well with the results in the literatures.^{18,20,21} It is mainly attributed to the excellent abilities of Ru and Pt in hydrogen activation, stabilization and utilization, since these two metals are commonly used materials for hydrogen storage^{22,23} and fuel cells.^{24,25} Since converting CO₂ to CH₄ is a multiple-step and multiple-electron reaction, there must be an inexhaustible supply of active hydrogen (H*) to CO₂.^{4,5} CO molecules possess dominant adsorption ability than H₂O at Pt surface.²⁶ After CO₂ molecules have been reduced to CO, the supply of active hydrogen decrease gradually until the Pt surface was fully occupied by CO and finally poisoned by them.^{26,27} Thus, the CO₂ reduction over Pt predominantly carries out a 2e⁻ reaction and CO become the main product. Conversely, water molecules are more adsorptive at Ru surface,²⁶ and Ru has a relative high overpotential in H₂ evolution²⁸ to depress the H* recombining to H₂. Thus, active hydrogens could be constantly provided to CO₂ to carry out 8e⁻ reaction.

In addition, the state of Ru is also very important to the activity. Different from other noble metals, Ru is very easy to be oxidized during the drying process. Moreover, this oxidation might be even enhanced when only using water as the reductant due to the formation of Ru(OH)_{ads}.^{25,26} Thus, the real state of the cocatalysts should be a mixture of Ru and RuO₂ or RuO_x as the XRD patterns shown in Fig. 2.11. The partially oxidized RuO_x not only hinder the electron transfer from NaTaO₃ to Ru, but also weaken the hydrogen activation on metal Ru. So that it lead to a very poor activity as shown in the previous part (Fig. 2.4).

However, after introducing the electron donor H_2 , RuO_x could be reduced and transformed to metal Ru again. As the XPS spectra shown in Fig. 2.12, Ru oxides in the as-prepared Ru-NaTaO₃ were reduced to metal Ru. The corresponding TEM image (Fig. 2.13) also indicates the successful transformation to metal Ru. Thus, a stable CO₂ reduction can be ensured over Ru-NaTaO₃.

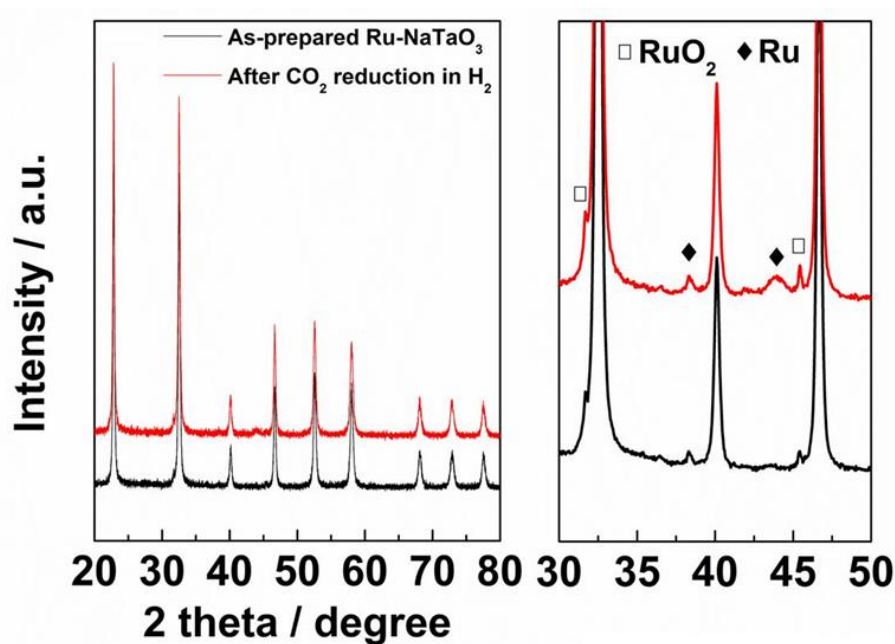


Fig. 2.11 XRD patterns of Ru-NaTaO₃ samples. Black line: as-prepared Ru-NaTaO₃, Red line: Ru-NaTaO₃ after a CO₂ reduction under H₂ atmosphere.

□ RuO₂, ◆ Ru. 10 wt% Ru-NaTaO₃ was adopted for better observation of the responds of RuO₂ and Ru.

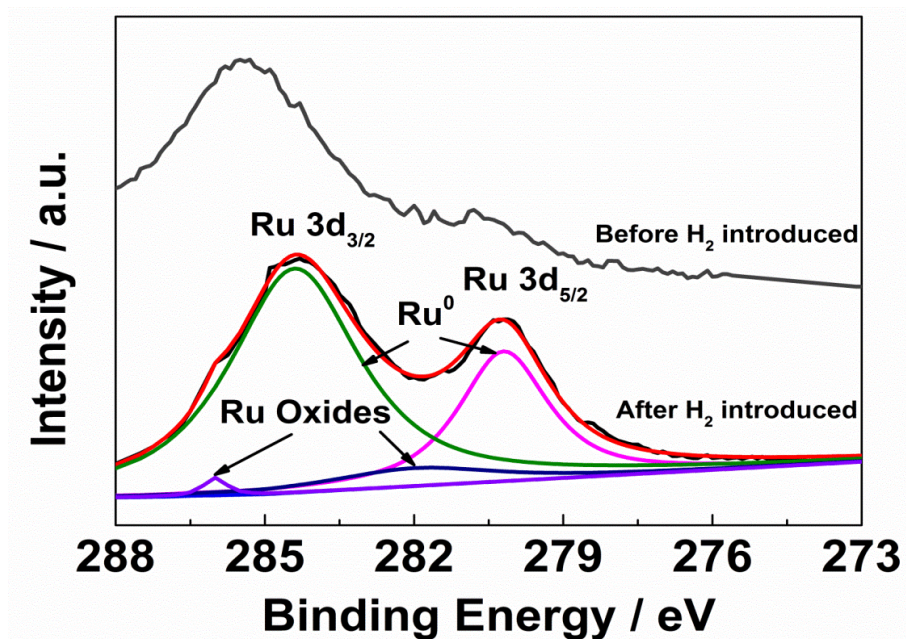


Fig. 2.12 XPS spectra of Ru-NaTaO₃ before and after the CO₂ reduction in the presence of electron donor H₂.

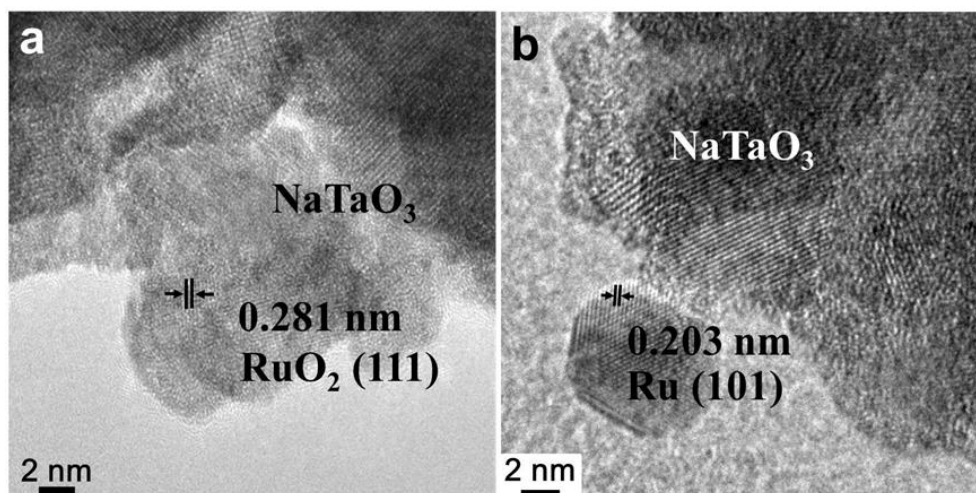


Fig. 2.13 TEM images of a) as-prepared Ru-NaTaO₃, b) Ru-NaTaO₃ after CO₂ reduction in H₂ atmosphere.

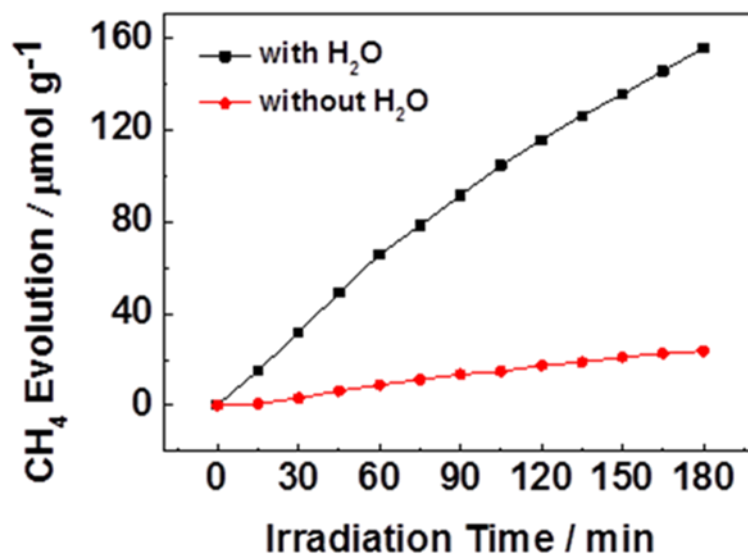


Fig. 2.14 CH₄ evolution comparison of Ru-NaTaO₃ with and without H₂O in presence of electron donor H₂.

The CO₂ reduction over Ru-NaTaO₃ without specifically adding the distilled water into the reaction system was compared with the water-using sample as shown in Fig. 2.14. The activity decreased obviously without water, but there is still a little amount of CH₄ could be detected. It could be considered that these CH₄ was comes from the water remained in the system as well as the gas atmosphere, because it is very different to make an extreme anhydrous condition in our reaction system. Long-playing experiments were carried out to examine the stabilities of these two samples, respectively (Fig. 2.15). Ru-NaTaO₃ keeps a linear growth of CH₄ evolution even overnight, whereas Pt-NaTaO₃ exhibits a decay of CO evolution after several hours due to the poisoning of Pt by the produced CO.^{26,27} Further experiments were also carried out to confirm the light dependent photocatalytic activity (Fig. 2.16). Both Ru-NaTaO₃ and Pt-NaTaO₃ expressed obviously feedbacks, i.e., the reactions exhibit very poor activities under visible light irradiation and there were hardly increases of the products

until the L42 filter was removed. Thus, it could be definitely concluded that CO_2 was photocatalytically reduced over Ru-NaTaO_3 and Pt-NaTaO_3 , as NaTaO_3 is a wide band-gap semiconductor (4.2 eV). An isotope experiment was carried out over Ru-NaTaO_3 for further investigation using $^{13}\text{CO}_2$. The GC-MS spectrum exactly confirmed that the organic product $^{13}\text{CH}_4$ was reduced from $^{13}\text{CO}_2$ as shown in Fig. 2.17.

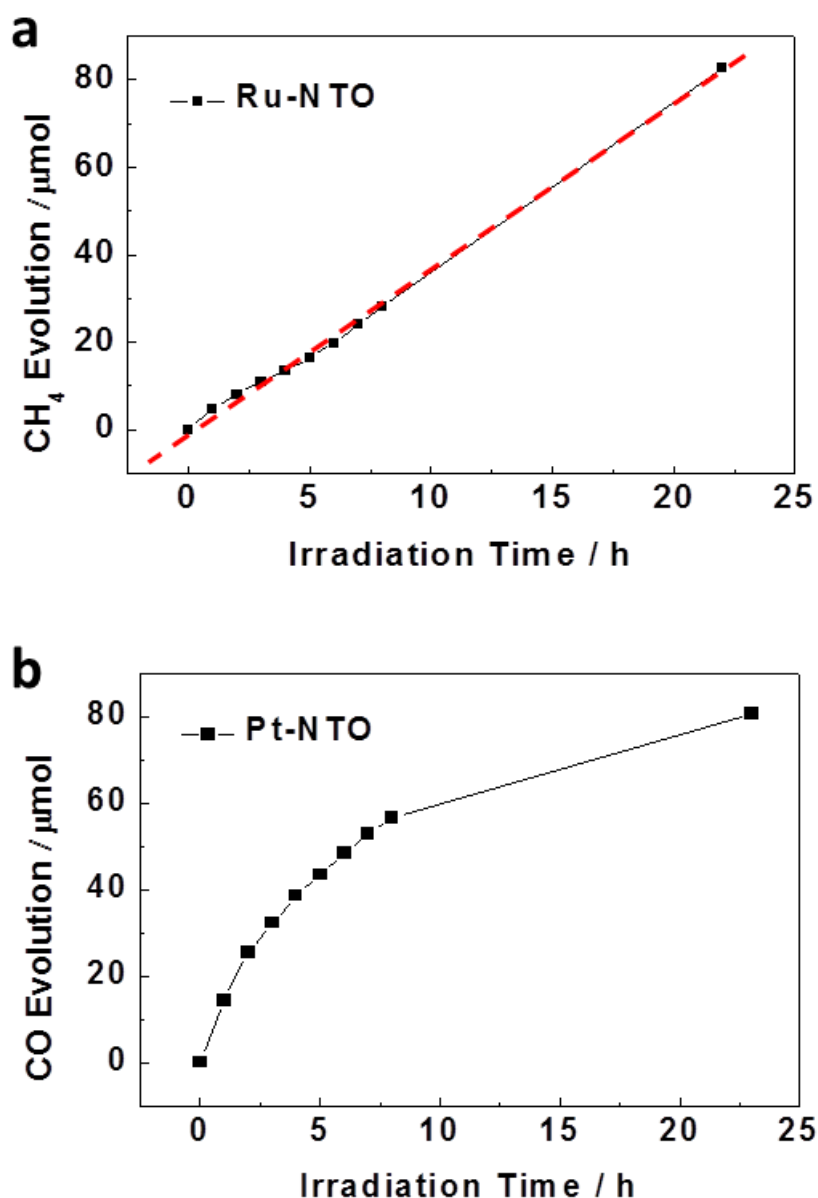


Fig. 2.15 An overnight prolonging text in the presence of electron donor H_2 : a) CH_4 evolution over Ru-NaTaO_3 , b) CO evolution over Pt-NaTaO_3 .

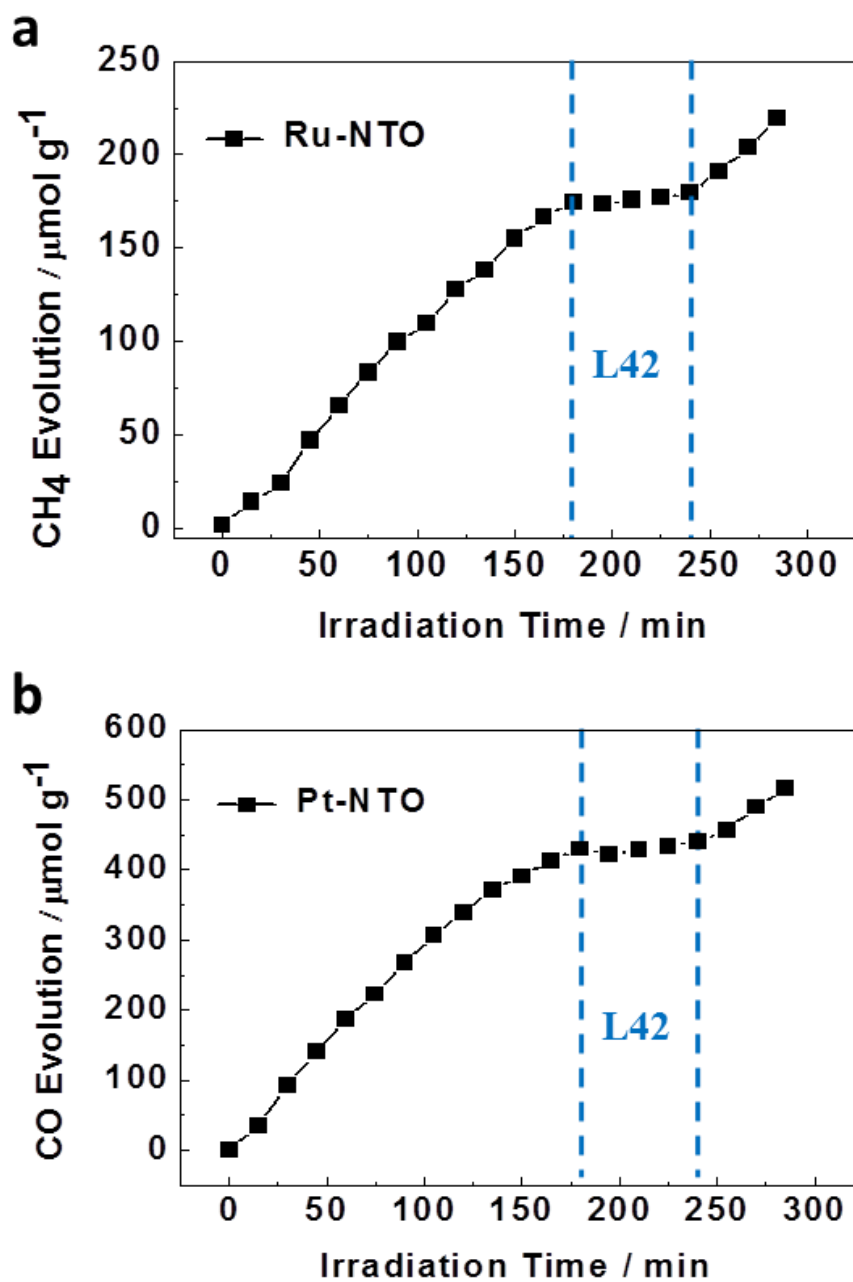


Fig. 2.16 UV-light responds text by inserting a cutoff 420 nm filter (L42) under the irradiation of a 300W UV-enhanced Xe lamp within H₂ atmosphere: a) CH₄ evolution over Ru-NaTaO₃, b) CO evolution over Pt-NaTaO₃.

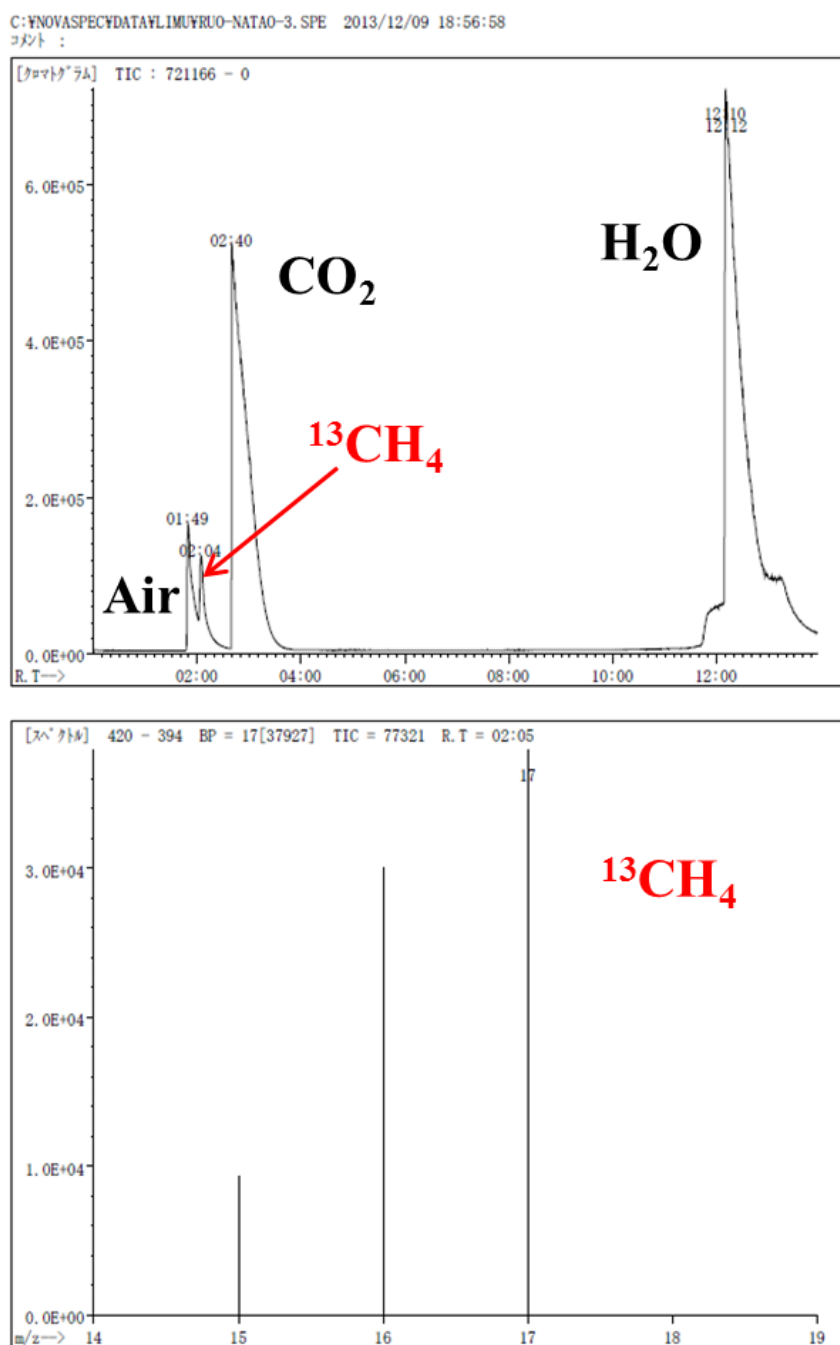


Fig. 2.17 Original data of GC-MS spectra of photocatalytic CO₂ reduction products over Ru-NaTaO₃ under H₂ atmosphere in the present of ¹³CO₂.

In addition, Ru loaded SrTiO₃ and TiO₂ also exhibit stable photocatalytic activities of converting CO₂ to CH₄ in the presence of electron donor H₂ as summarized in Table 2.3 and Fig. 2.18. The activity differences among NaTaO₃, SrTiO₃ and TiO₂ are mainly attributed to their different CB levels (Fig. 2.18 and Fig. 2.19). NaTaO₃ possess the most negative CB energy level, thus it could provide the most energetic photogenerated electrons to overcome the activation barrier and fulfill the 8e⁻ reaction during the CO₂ reduction process. Moreover, these results demonstrate that electron donor could also be extended to other semiconductors to realize a stable photoreduction of CO₂.

Table 2.3 Comparison of the band gaps, BET surface areas and productivities among NaTaO₃, SrTiO₃ and TiO₂.

Materials	Band gap / eV ^a	VB / V ^b	CB / V ^c	Surface area	CH ₄ productivity	Normalized productivity
				/ m ² g ⁻¹ ^d	/ μmol g ⁻¹ h ⁻¹ ^e	/ μmol h ⁻¹ m ⁻² ^f
NaTaO ₃	4.2	2.7	-1.5	29.2	51.8	1.72
SrTiO ₃	3.7	2.6	-1.1	14.4	5.4	0.38
TiO ₂	3.5	3.0	-0.5	302.2	29.2	0.10

^aThe band gap were obtained from UV-vis absorption spectra and the corresponding $(\alpha h\nu)^{1/2} - h\nu$ curves as shown in Fig.1c and Fig. S8. ^bThe valence band positions were obtained from valence band XPS as shown in Fig. S7. ^cThe conduction band positions were calculated from the data of band gap (E_g) and valence band by using the equation $CB = VB - E_g$. ^dThe surface area were determined by the Brunauer–Emmett–Teller (BET) method. ^eThe apparent productivity within 8 hours. ^fCalculated from dividing the apparent productivity by BET surface area.

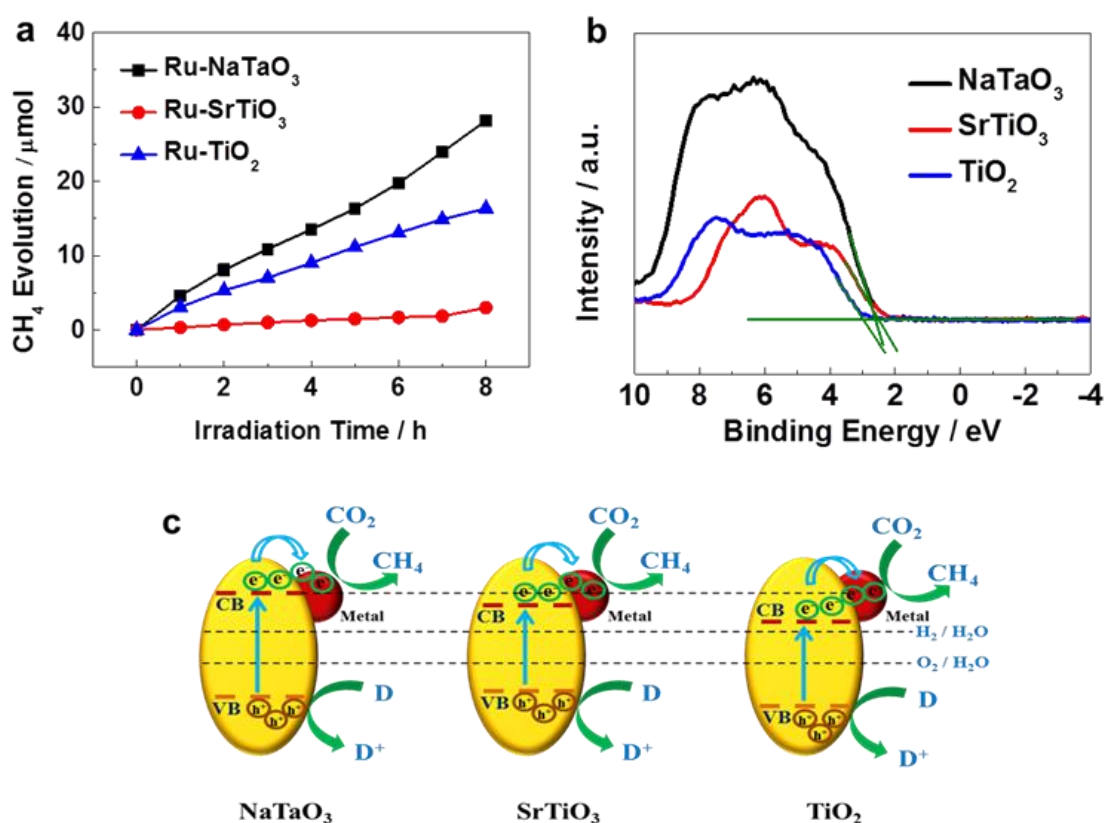


Fig. 2.18 a) CH₄ evolution comparison of Ru loaded NaTaO₃, commercial SrTiO₃ (Nano-sized, Wako Pure Chemical Industries, Japan) and TiO₂ (ST01, ISHIHARA SANGYO KAISHA, Japan) under the irradiation of a 300W UV-enhanced Xe lamp within H₂ atmosphere. b) Valence band XPS of NaTaO₃, SrTiO₃ and TiO₂. c) Schematic model of energy levels of NaTaO₃, SrTiO₃ and TiO₂ under UV irradiation.

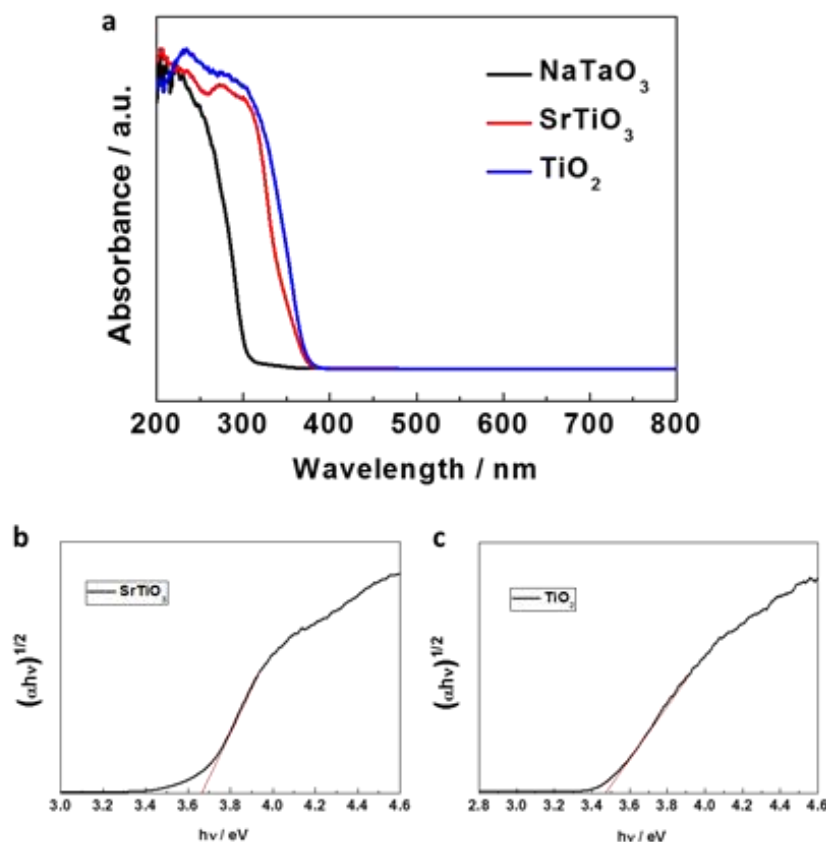


Fig. 2.18 a) UV-vis absorption spectra comparison of NaTaO₃, SrTiO₃ and TiO₂; b) the corresponding band gap obtained from $(\alpha h\nu)^{1/2} - h\nu$ curves: (b) SrTiO₃, (c) TiO₂.

2.4 Conclusions

In conclusion, this study demonstrated that the photocatalytic activities of NaTaO₃ are greatly affected by noble metal cocatalysts and the reaction atmosphere. By introducing electron donor H₂ into the system, a stable reactivity has been obtained over the series of NaTaO₃ due to an effective release of the peroxides intermediates of water oxidation. Ru-NaTaO₃ (CH₄ 51.8 $\mu\text{mol h}^{-1} \text{g}^{-1}$) and Pt-NaTaO₃ (CO 139.1 $\mu\text{mol h}^{-1} \text{g}^{-1}$) exhibited the best products selectivity in

the presence of the electron donor. Besides, Ru demonstrated an efficient and stable photocatalytic activity in converting CO₂ to CH₄ beyond 24 hours. These results and discussion reveal that as co-catalysts, Ru possesses an efficient ability to promote the photogenerated charge separation as well as the hydrogen activation, stabilization and utilization in the presence of electron donor in photocatalytic reduction CO₂ to CH₄.

Moreover, according to this chapter's study, it can be concluded that it is still very difficult for realizing an overall CO₂ conversion in one single semiconductor photocatalyst. For one thing, the water oxidation half reaction can hardly be carried out without electron donors. On the other hand, the exact reaction process of the reduction half reaction is still unclear, because the gaseous reaction environment makes it very different to study the mechanism as well as to obtain an efficient CO₂ conversion. In this regard, photoelectrochemistry provides a facile approach to study the CO₂ reduction process, in which the reduction process can be easily investigated at the fixed potential region.

References

1. A. Fujishima and K. Honda, *Nature*, 1972, **238**, 37-38.
2. H. Tong, S. Ouyang, Y. Bi, N. Umezawa, M. Oshikiri and J. Ye, *Adv. Mater.*, 2012, **24**, 229-251.
3. W. Tu, Y. Zhou and Z. Zou, *Adv. Mater.*, 2014, **26**, 4607-4626.
4. J.-M. Lehn and R. Ziessel, *Proc. Natl. Acad. Sci. U.S.A.*, 1982, **79**, 701-704.
5. B. Kumar, M. Llorente, J. Froehlich, T. Dang, A. Sathrum and C. P. Kubiak, *Annu. Rev. Phys. Chem.*, 2012, **63**, 541-569.
6. H. Kato and A. Kudo, *J. Phys. Chem. B*, 2001, **105**, 4285-4292.

7. H. Kato, K. Asakura and A. Kudo, *J. Am. Chem. Soc.*, 2003, **125**, 3082-3089.
8. A. Yamakata, T.-a. Ishibashi, H. Kato, A. Kudo and H. Onishi, *J. Phys. Chem. B*, 2003, **107**, 14383-14387.
9. J. Yang, D. Wang, H. Han and C. Li, *Acc. Chem. Res.*, 2013, **46**, 1900-1909.
10. H. Zhou, J. Guo, P. Li, T. Fan, D. Zhang and J. Ye, *Sci. Rep.*, 2013, **3**, 1667.
11. R. Nakamura and Y. Nakato, *J. Am. Chem. Soc.*, 2004, **126**, 1290-1298.
12. P. Li, S. Ouyang, G. Xi, T. Kako and J. Ye, *J. Phys. Chem. C*, 2012, **116**, 7621-7628.
13. P. Li, S. Ouyang, Y. Zhang, T. Kako and J. Ye, *J. Mater. Chem. A*, 2013, **1**, 1185-1191.
14. P. Li, H. Xu, L. Liu, T. Kako, N. Umezawa, H. Abe and J. Ye, *J. Mater. Chem. A*, 2014, **2**, 5606-5609.
15. M. A. Butler, *J. Appl. Phys.*, 1977, **48**, 1914-1920.
16. Q. Liu, Y. Zhou, J. Kou, X. Chen, Z. Tian, J. Gao, S. Yan and Z. Zou, *J. Am. Chem. Soc.*, 2010, **132**, 14385-14387.
17. W. Wang, S. Wang, X. Ma and J. Gong, *Chem. Soc. Rev.*, 2011, **40**, 3703-3727.
18. X. Meng, T. Wang, L. Liu, S. Ouyang, P. Li, H. Hu, T. Kako, H. Iwai, A. Tanaka and J. Ye, *Angew. Chem. Int. Ed.*, 2014, **53**, 11478-11482.
19. Q. Kang, T. Wang, P. Li, L. Liu, K. Chang, M. Li and J. Ye, *Angew. Chem. Int. Ed.*, 2015, **54**, 841-845.
20. M. Azuma, K. Hashimoto, M. Hiramoto, M. Watanabe and T. Sakata, *J. Electrochem. Soc.*, 1990, **137**, 1772-1778.
21. J. Lee, Y. Kwon, R. L. Machunda and H. J. Lee, *Chem. Asian J.*, 2009, **4**, 1516-1523.
22. L. Wang and R. T. Yang, *J. Phys. Chem. C*, 2008, **112**, 12486-12494.
23. D. Saha and S. Deng, *Langmuir*, 2009, **25**, 12550-12560.
24. H. F. Oetjen, V. M. Schmidt, U. Stimming and F. Trila, *J. Electrochem. Soc.*, 1996,

143, 3838-3842.

25. H. Liu, C. Song, L. Zhang, J. Zhang, H. Wang and D. P. Wilkinson, *J. Power Sources*, 2006, **155**, 95-110.
26. T. Yajima, H. Uchida and M. Watanabe, *J. Phys. Chem. B*, 2004, **108**, 2654-2659.
27. M. Wakisaka, T. Ohkanda, T. Yoneyama, H. Uchida and M. Watanabe, *Chem. Commun.*, 2005, 2710-2712.
28. A. J. Bard and L. R. Faulkner, *Electrochemical Methods: Fundamentals and Applications*, Wiley, 2000.

Chapter 3 Mesoporous Palladium-Copper Bimetallic Electrodes for Selective Electrocatalytic Reduction of Aqueous CO₂ to CO

3.1 Introduction

Electrocatalytic reduction of CO₂ is a promising method for its high-density renewable energy storage and the incentive ability for CO₂ capture among various CO₂ reusable approaches.^{1,2} Significantly, electrochemical CO₂ reduction possess much higher energy conversion efficiency, better product selectivity and much clearer mechanism than the photocatalytic CO₂ reduction process.³ It provides a convenient approach to study the kinetic reaction process of CO₂ reduction. And consequently could guide the research and fabrication of not only electrocatalysts but also photocatalysts (cocatalysts).

In the point view of CO₂ reduction product, CO is a desirable product of CO₂ reduction, because it could serve as a very important raw material in chemical industry to produce chemicals and synthetic fuels through the well-known Fischer–Tropsch process.⁴ So far, gold-based nanostructured electrocatalysts demonstrated attractively high selectivity in converting aqueous CO₂ to CO, with Faradaic efficiency (FE) exceeding 90%.⁵⁻⁷ However, the high cost of Au as noble metal and the complicated process for fabricating Au to the extremely specific nanostructure have significantly impeded the large scale manufacture as well as the subsequent commercial application of the gold-based electrocatalysts. Moreover, although some non-precious metals also demonstrated very high FE in

reducing CO₂ to CO in ionic liquids or non-aqueous electrolytes,^{8,9} the real effect and active components of these electrolyte are still nebulous.¹⁰ Aqueous electrolyte is more conducive to precisely assess the catalytic ability of metal catalysts. Therefore, it is important to pay more attention to lessening the use of noble metals in the design of electrocatalysts and finding a facile synthesis process for the selective reduction of CO₂ to CO in aqueous electrolyte.

Alloying is one of the most impactful candidate approaches to reduce the materials cost.^{11,12} It is believed that by alloying, due to the electronic effect and geometric effect, the binding strength of intermediates could be effectively tuned to accelerate the reaction rate of CO₂ reduction on the catalyst surface.¹¹ According to Azuma et al.'s summary about the relations between metal catalysts and corresponding products,¹³ CO and hydrocarbons are the primary products over d metals (e.g., Pd, Pt, Cu and Au).¹⁴ Thus, alloying palladium with inexpensive copper should be a promising strategy for the selective reduction of aqueous CO₂ to CO. Based on the metal price from London Metal Exchange (LME), at least 40% of the materials cost can be reduced when comparing with the gold catalysts.

Well-defined mesoporous metal catalysts are commonly cited for superior performance on electrocatalytic activity because of their high porosity, large area per unit volume, and excellent activity-structure relationship.^{15, 16} The physicochemical characteristics of Pd and Cu also benefit the alloy synthesis to a functional architecture, such as mesoporous nanostructure, with more roughened surface and active sites than nanoparticles. It has been confirmed by both of the experimental results and DFT calculations that active sites play a dominant role for the selectivity of CO₂ reduction on Au nanoparticles.⁶ The density of

catalytically active sites is largely dependent on the particle size and surface structure and it is deduced that a roughened surface facilitates the selective reduction of CO₂.^{7,17}

In this chapter, novel mesoporous palladium-copper bimetallic electrocatalysts with a high density of mesopores were designed and fabricated via a facile electrodeposition approach for selective reduction of aqueous CO₂ to CO. Various ratios of mesoporous Pd-Cu electrodes have been prepared by finely controlling the stoichiometric ratio of electrolyte solution. The mesoporous nanostructure was expected to harvest the active sites for the selective reduction of aqueous CO₂ to CO. The binding strength of intermediates was proposed to be adjusted by forming palladium-copper alloys. To the best of our knowledge, this is the first paradigm of mesoporous alloy electrocatalysts for the selective reduction of CO₂ to CO.

3.2 Experimental methods

3.2.1 Preparation of mesoporous Pd-Cu electrocatalysts

To fabricate mesoporous Pd-Cu electrodes, a constant potential electrodeposition was carried out at -0.2 V by using an electrochemical machine (CHI 660D electrochemical analyzer, CH Instrument, U.S.) with a standard three-electrode cell system, including an Ag/AgCl (saturated KCl) electrode as a reference electrode, a platinum wire as a counter electrode. Glassy Carbon (GC) substrate (diameter = 3 mm, BAS Inc.) was employed as the working electrode for the measurements of electrocatalytic reduction of CO₂, while ITO substrate (deposition area: ca. 1 cm²) was used as working electrode for sample

characterizations. The electrolyte solution contained PdCl_2 and $\text{Cu}(\text{NO}_3)_2$ with Brij 58 ($\text{C}_{16}\text{H}_{33}(\text{OCH}_2\text{CH}_2)_{20}\text{OH}$, 1.0 wt%) as the surfactant. The total concentration of metal precursors was 10 mM. The molar ratios of Pd to Cu species were gradually changed ($\text{Pd}^{2+}/\text{Cu}^{2+} = 10:0, 9:1, 8:2, 7:3, 6:4, 5:5, 3:7$ and $0:10$, respectively) for the preparation of mesoporous Pd-Cu electrodes with different compositions. After electrodeposition for 600 s, as-prepared films were soaked in ethanol for 24 h to extract the surfactants, then thoroughly rinsed with de-ionized water, and dried in air. $\text{Pt}_x\text{Cu}_{10-x}$ (x varies from 9 to 1) were used as abbreviations for the samples prepared from different precursor solutions and pure Pd and Cu were abbreviated as “Pd” and “Cu”, respectively. Nanoparticle counterpart Pd_7Cu_3 was prepared by the same electrodeposition method without surfactant Brij 58. Nanoparticle Pd_7Cu_3 and mesoporous Pd_7Cu_3 were abbreviated as N- Pd_7Cu_3 and M- Pd_7Cu_3 , respectively.

3.2.2 Electrochemical measurements

The electrocatalytic reduction of CO_2 was measured on a CHI 660D electrochemical workstation in aqueous 0.1 M KHCO_3 solution ($\text{pH} \approx 6.8$). The electrolyte solution was purged by Ar gas and saturated with CO_2 successively before the measurement. The experiments were performed in a gas-tight two compartment H-cell separated by a Nafion117 film. Platinum and Ag/AgCl (in saturated KCl) electrode were selected as the counter electrode and reference electrode, respectively. All of the applied potentials were recorded against Ag/AgCl (saturated KCl) reference electrode and then converted to reversible hydrogen electrode (RHE). The CO and other carbon products were sampled and measured with a gas chromatograph (GC-14B, Shimadzu) equipped with a flame

ionization detector (FID) according to the standard curves. The GC column is Porapak Q-methanizer for CO and CO₂ measurement, PEG1000 for organic products measurement. The product of H₂ was measured with a gas chromatograph (GC-8A, Shimadzu) with a TCD detector according to the standard curve. The GC column is 5A molecular sieve. The Faradaic efficiency (FE) can be calculated from $FE = znF / jt$, where z (reaction electron number) = 2 for CO and H₂, n is the GC detected product molar number (mol cm⁻²), F is the Faradaic constant (C mol⁻¹), j is the photocurrent (A cm⁻²) and t is the reaction time (s).

3.2.3 Sample characterization

Scanning electron microscopy (SEM) was conducted with a HITACHI S-4800 field emission scanning electron microscopy. Transmission electron microscopy (TEM) and High-resolution TEM (HRTEM) images were recorded with a field emission transmission electron microscope (2100F, JEOL Co., Japan) operated at 200 kV, combined with energy dispersive X-ray spectroscopy (EDX) for the determination of metal composition. The compositional ratios of the mesoporous alloys were analyzed by inductively coupled plasma optical emission spectrometry (ICP-OES, Agilent 720-ES, Agilent Technologies, United States). X-ray diffraction (XRD) patterns were recorded on an Intelligent XRD system (SmartLab, Rigaku Corporation, Japan). Low-angle X-ray diffraction (XRD) patterns were acquired by a Rigaku NANOViewer (Cu K α) operated at 40 kV and 30 mA. The specific surface areas were determined with Belsorp 28 apparatus (Bel Japan Inc., Japan) by the Brunauer-Emmett-Teller (BET) method. X-ray Photoelectron Spectroscopy (XPS) experiments were performed in type

Theta probe (ULVAC-PHI, Japan) using monochromatized Al $K\alpha$ at 1.4×0.1 mm 100 W(20 kV, 5 mA) and the peak positions were internally referenced to the C 1s peak at 285.0 eV.

3.2.4 Computational section

All of structure relaxation and electronic structure calculations were performed within the Kohn-Sham density functional theory (DFT) framework as implemented in the Vienna ab initio simulation package (VASP). The projector augmented wave (PAW) method and the semilocal Perdew-Burke-Ernzerhof exchange-correlation functional revised for solids (PBEsol) were adopted in present calculations. A 900 eV kinetic energy cutoff was used in the relaxations and electronic structure calculations of bulk metals, and a 600 eV cutoff energy was employed for surfaces. K-points for bulk relaxation and surface relaxation are respectively $9 \times 9 \times 9$ and $3 \times 3 \times 1$.

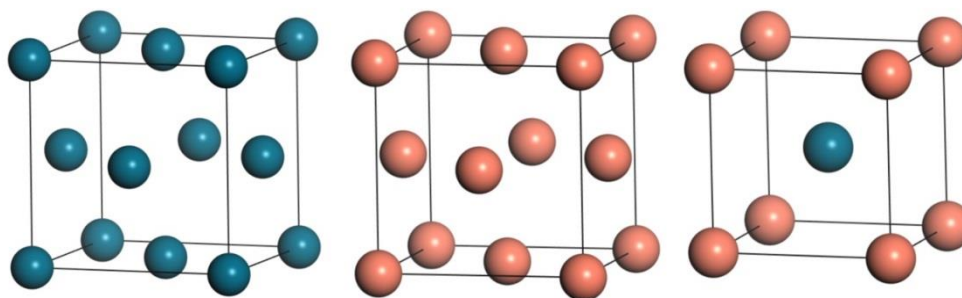


Fig. 3.1 Crystal structures of different metals: (a) Pd, (b) Cu and (c) Pd-Cu.

Table 3.1 Experimental and calculated lattice constants of Pd, Cu and Pd-Cu.

Metal	Space group	$a=b=c$ (Å)	
		Experimental	Calculated (PBEsol)
Pd	FM-3M	3.891	3.872
Cu	FM-3M	3.615	3.570
Pd-Cu	PM-3M	3.987	3.963

The structures and lattice parameters of Pd, Cu and Pd-Cu used in present study are shown and listed in Fig. 3.1 and Table 3.1. The lattice constants obtained from DFT calculations are very consistent with experimental values. Different crystalline structures were adopted for constructing the slab models for DFT calculations (Space group FM-3M for Pd, Cu; PM-3M for Pd-Cu alloy). These different slab models were employed for obtaining stable 111 facet models of Pd, Cu and Pd-Cu alloy during the DFT calculations. Based on the relaxed bulk structures, the slab models of Pd (111), Cu (111), Pd- and Cu-terminated Pd-Cu (111) were built. Among them, Cu (111) and Pd (111) are respectively composed of 96 Cu atoms and 96 Pd atoms. Pd-terminated Pd-Cu (111) surface possesses 63 Pd atoms and 54 Cu atoms, whereas Cu-terminated Pd-Cu (111) surface has 63 Cu atoms and 54 Pd atoms. All slab models are separated from z-direction neighbours by a 20 Å vacuum thickness. To get a quantitative

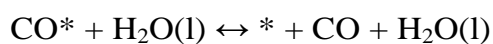
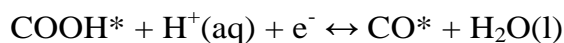
measurement of the charge transfer between Pd and Cu atoms in Pd-Cu alloy, Bader charge analysis was performed and the results for surfaces.

To study the influence of charge transfer between Pd and Cu atoms on the adsorption and desorption of CO₂, COOH* and CO, the adsorption energies of X (X stands for CO₂, COOH* and CO) molecule on different kinds of surface were calculated using following equation:

$$E_{\text{ads}}(\text{X}) = E_{\text{tot}}(\text{X/surface}) - E_{\text{tot}}(\text{X}) - E_{\text{tot}}(\text{surface})$$

Where $E_{\text{tot}}(\text{X/surface})$ is the total energy of optimized X molecule adsorption configuration at different surface, $E_{\text{tot}}(\text{X})$ is the total energy of an isolated X molecule, and $E_{\text{tot}}(\text{surface})$ is the total energy of surface model.

In order to understand the experimentally observed trends for the electroreduction of CO₂ to CO, the following reaction mechanism was adapted to calculate the free energy:



Here, the asterisk (*) denotes a site on the surface.

3.3 Results and discussions

3.3.1 Characteristics of mesoporous Pd-Cu bimetallic electrocatalysts

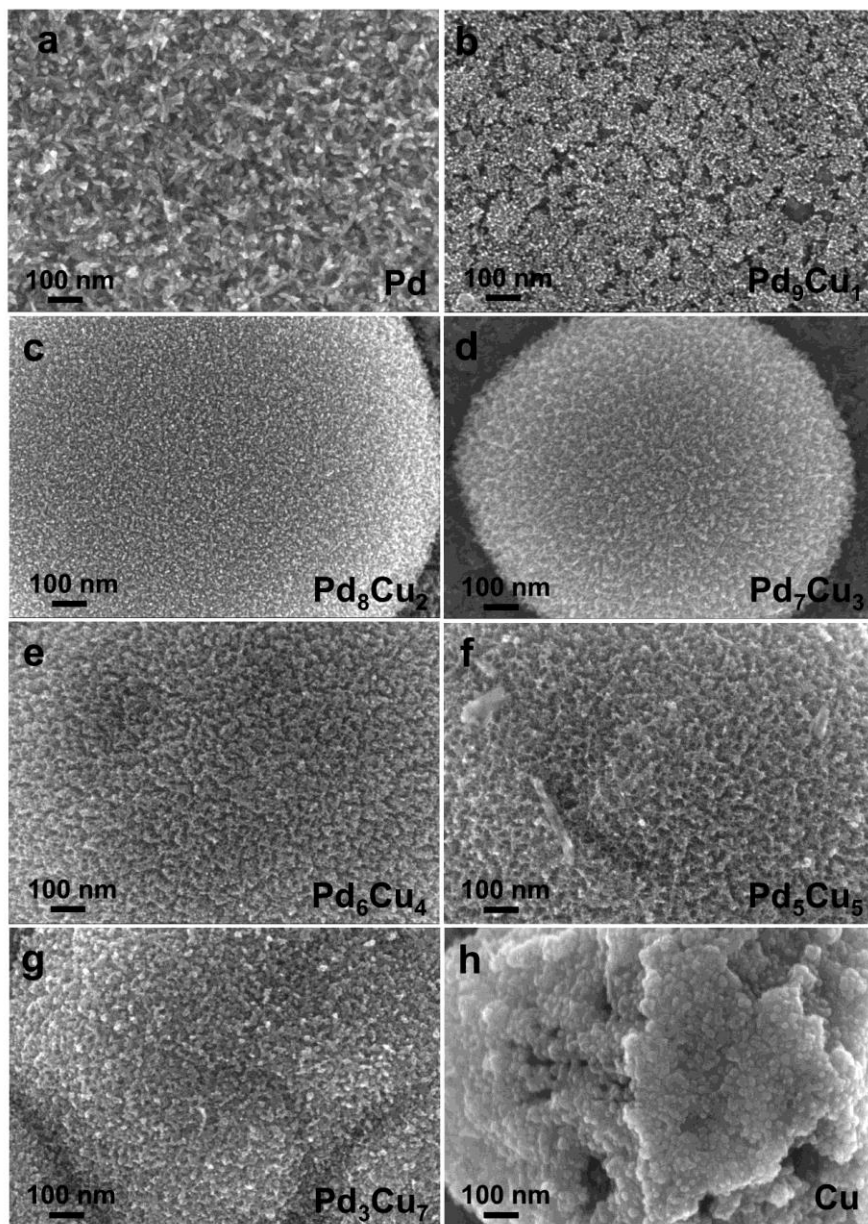


Fig. 3.2 Top-surface SEM images of mesoporous Pd-Cu electrocatalysts with different ratios: a) Pd, b) Pd₉Cu₁, c) Pd₈Cu₂, d) Pd₇Cu₃, e) Pd₆Cu₄, f) Pd₅Cu₅, g) Pd₃Cu₇ and h) Cu.

The top-surface morphologies of the Pd-Cu alloy electrocatalysts with various molar ratios were characterized by scanning electron microscope (SEM) as shown in Fig. 3.2. The morphologies exhibit obvious differences depending on the Pd and Cu compositions. Pure Pd (Fig. 3.2a) shows a nanorod-like surface structure with large disordered pores. With alloying Pd with Cu, the surface structures change to cauliflower-like surfaces gradually (Fig. 3.2b-3.2g). Highly dispersed mesopores with uniform sizes could be clearly confirmed in each bimetallic electrocatalysts. Pure Cu (Fig. 3.2h), whereas, tend to form nanoparticles, due to the difficult preparation of copper into porous in this synthetic condition.¹⁸

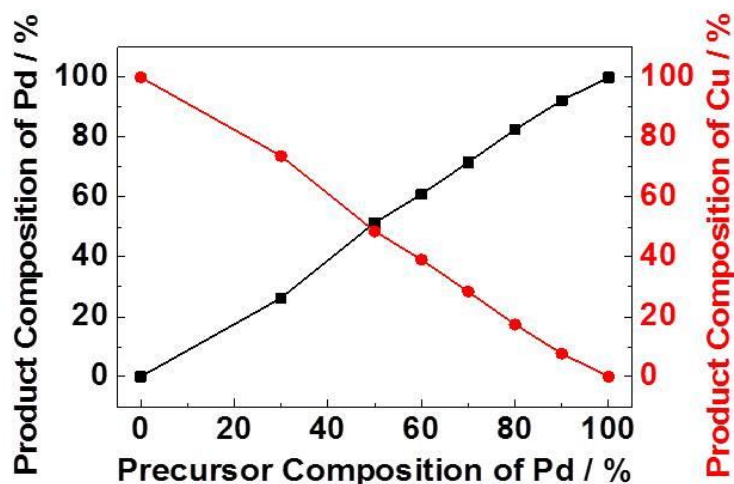


Fig. 3.3 Top-surface relationship between the product and precursor compositions examined by ICP-OES.

The exact compositional ratios of the alloys were characterized by inductively coupled plasma optical emission spectrometry (ICP-OES) as shown in Fig. 3.3. The content of both palladium and copper in the products was linearly varied with the corresponding metallic precursors and accorded well with the stoichiometric ratios in the starting electrolyte solutions. In order to further

confirm the formation of mesoporous architecture, low-angle X-ray diffraction (XRD) measurements were carried out as shown in Fig. 3.4. Broad peaks are confirmed in the 2θ range around 1.0° . The d-spacing of the peaks is calculated to be ~ 8 nm which corresponds to the pore-to-pore distance. Considering the pore wall thickness (1~2 nm), the average pore size can be estimated to be approximately 6~7 nm, which coincides with the ideal pore size prepared by Brij 58 micelles through constant potential deposition.^{19, 20}

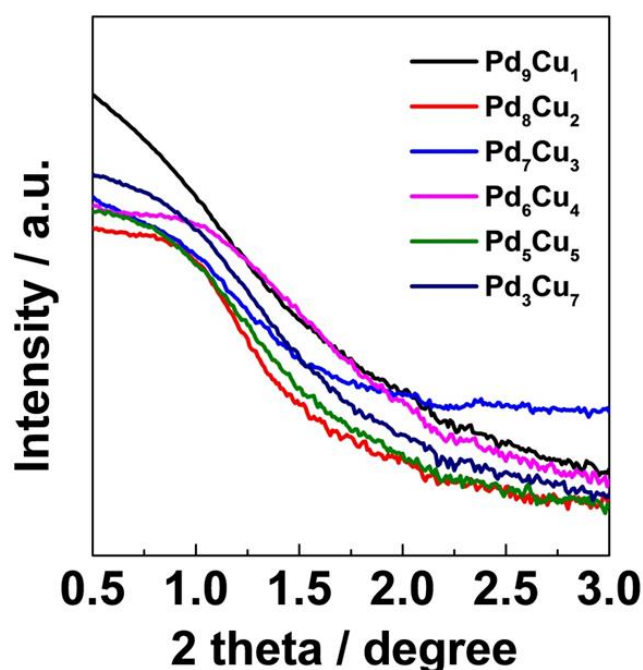


Fig. 3.4 Low-angle XRD patterns of mesoporous Pd-Cu electrocatalysts with different ratios.

The detailed nanostructure of mesoporous electrocatalysts was further investigated by high-resolution TEM (HR-TEM) over Pd₇Cu₃ electrocatalyst as an example. Fig. 3.5a shows the TEM image and provides a parallel cauliflower-like mesoporous structure as the SEM results exhibited. The HR-TEM image in Fig. 3.5b shows a lattice fringes correspond to the crystal

plane (111) ($d = 2.22 \text{ \AA}$), which is between the characteristics of face centred cubic Pd ($d = 2.24 \text{ \AA}$) and Cu ($d = 2.09 \text{ \AA}$) crystal phase in the (111) plane, indicating the successful preparation of palladium-copper bimetallic alloys.^{21, 22} The corresponding EDX mapping analysis in Fig. 3.6 confirms that palladium and copper are homogeneously distributed within the mesoporous bimetallic alloys.

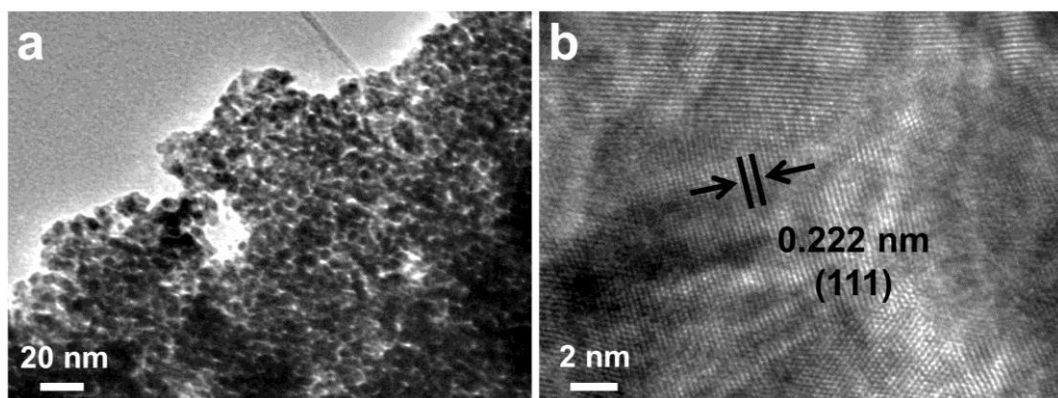


Fig. 3.5 a) TEM image, b) HR-TEM image of mesoporous Pd₇Cu₃ electrocatalyst.

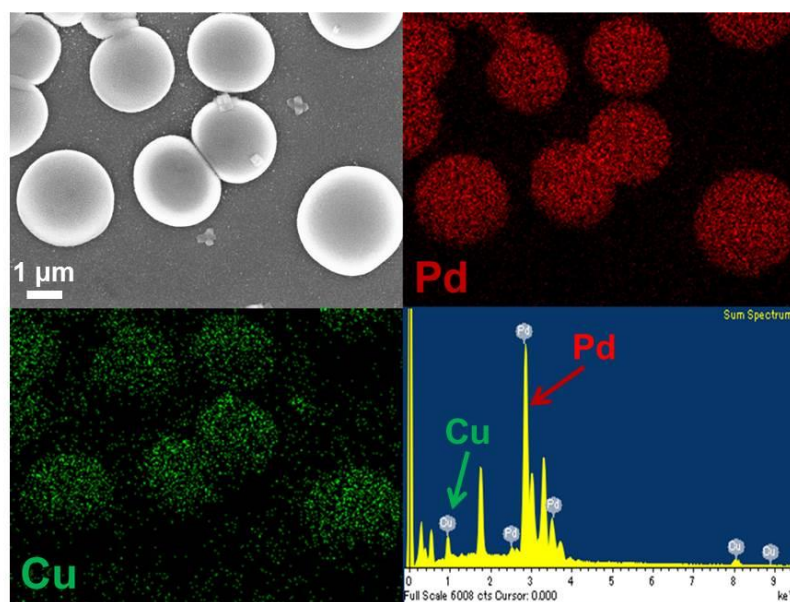


Fig. 3.6 EDX mapping of mesoporous Pd₇Cu₃ electrocatalyst.

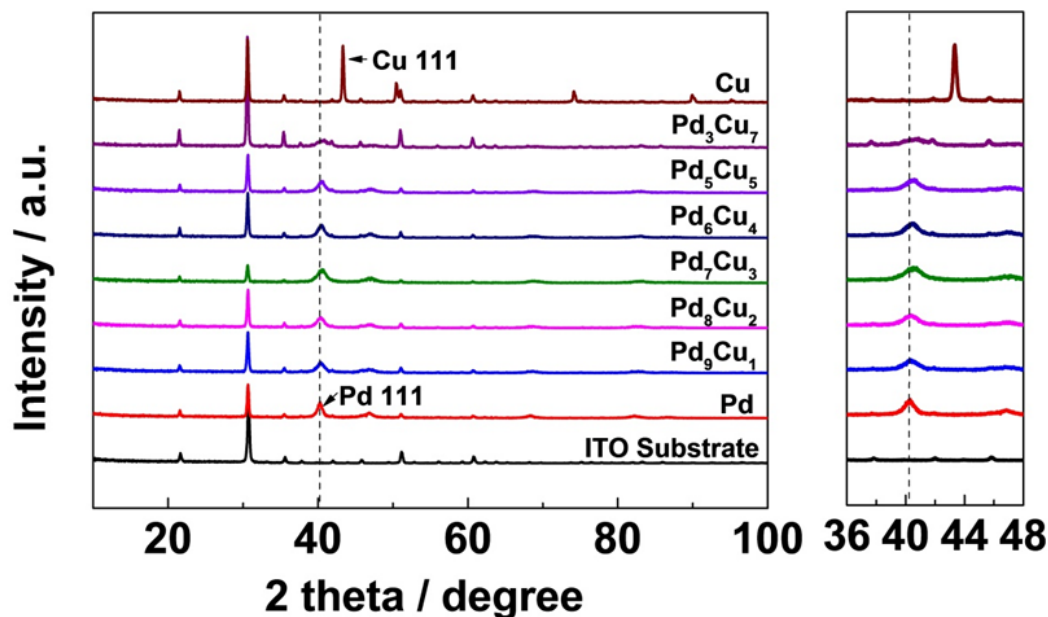


Fig. 3.7 XRD patterns of mesoporous Pd-Cu electrocatalysts with different ratios.

The XRD patterns of the mesoporous palladium-copper electrocatalysts are shown in Fig. 3.7. The (111) peak of each alloy sample can be observed between Pd (111) peak and Cu (111) peak. It shifts to higher angles gradually when increasing the Cu amount alloyed with Pd. It thus can be considered as another evidence of the successful preparation of palladium-copper bimetallic alloys.

3.3.2 The effectiveness of mesoporous nanostructure on the selectivity of CO₂ reduction

The electrocatalytic performances of the series of mesoporous Pd-Cu bimetallic alloys were investigated in a gas-tight two compartment H-cell separated by a Nafion film. The electrolyte solution containing 0.1 M aqueous KHCO₃ was purged by Ar gas and saturated with CO₂ successively before the measurement. Fig. 3.8 shows the overall current densities of the mesoporous Pd-Cu bimetallic alloys in the potential region from -0.7 V to -1.2 V vs. RHE. All the metal electrocatalysts show much higher activities

than the GC substrate where mesoporous Pd₇Cu₃ exhibits the largest total current density among the series. However, hydrogen evolution reaction (HER) is a very aggressive competing reaction to the selective reaction of CO₂ to CO, in which usually the overall current density also contains HER current. Fig. 3.9 shows the Faradaic efficiencies (FEs) for CO at different applied potentials. The optimal composition appears at Pd₇Cu₃, in which the FE for CO exceeds 80% at -0.8 V vs. RHE. Kanan et al. have reported a selective electrochemical reduction of CO₂ to formate on palladium nanoparticles.²³ While the products over reduced oxidized copper electrodes varied from 2-electron products CO, HCO₂H to multi-electron products C₂ hydrocarbons.²⁴ The products variation in our report can be contributed to the formation of Pd-Cu alloy, in which the electronic structures of electrocatalysts were adjusted gradually with the composition ratios. Moreover, the selectivity variation between 2-electron products from formate to CO can be also ascribed to the roughened surface. It is deduced that the mesoporous architecture benefit the selective reduction of CO₂ to CO by providing abundant active site.

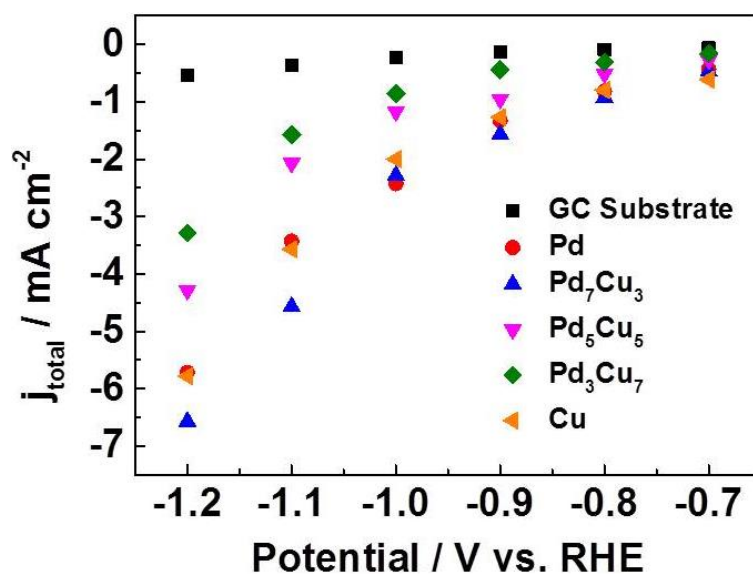


Fig. 3.8 Total current density plots of mesoporous Pd-Cu electrocatalysts.

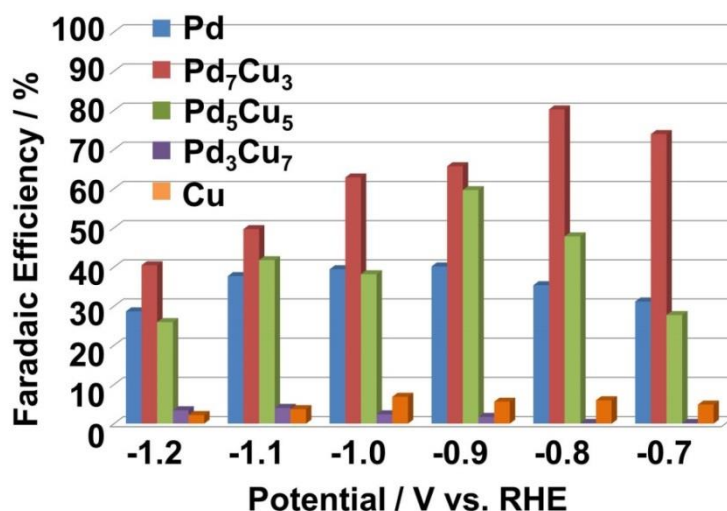


Fig. 3.9 Faradaic efficiency for CO of mesoporous Pd-Cu electrocatalysts.

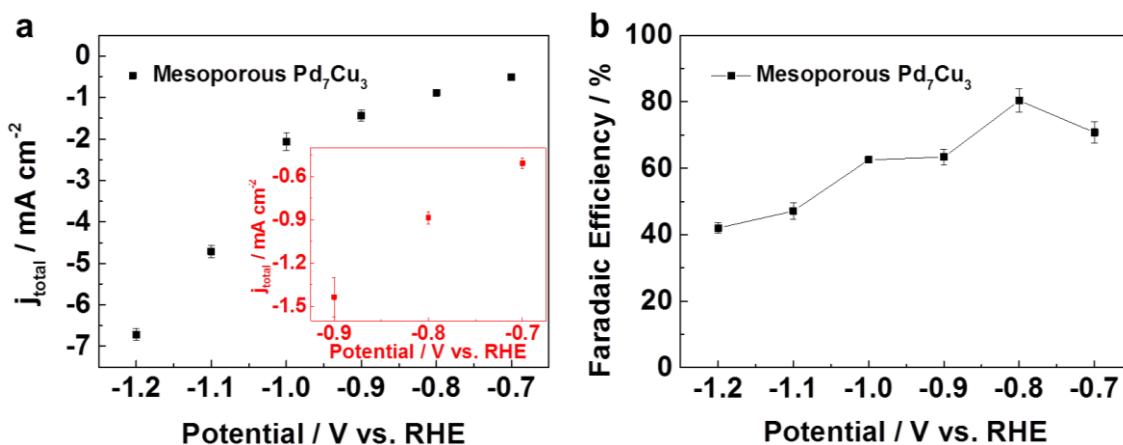


Fig. 3.10 a) Current densities and b) Faradaic efficiencies for CO of mesoporous Pd₇Cu₃ alloy with error bars.

Error bars were added to the current densities of mesoporous Pd₇Cu₃ by averaging the data of different samples as shown in Fig. 3.10. The inset in Fig. 3.10a shows the error bars at low current density potentials (-0.7 ~ -0.9 V vs. RHE). All the current densities at different potentials do not exhibit very large errors. At the optimal potential, -0.8 V vs. RHE, for the highest FE for CO, the current density varies within the region of -0.84 mA cm² to -0.93 mA cm². The corresponding FEs for CO on mesoporous

Pd₇Cu₃ are shown in Fig. 3.10b. The FEs at all the applied potentials also do not show very large errors. At -0.8 V vs. RHE, the FE varies within the region of ca. 77% to ca. 84% and a FE_{CO} of 80% was reported in my thesis. These data suggest that the electrocatalytic performance of the mesoporous alloy sample is not an incident result and can be reproduced within modest error region. The current density at the optimal potential, -0.8 V vs. RHE, is still very low compared with some previous reports. More studies will be focused on not only reducing the overpotentials, but also obtaining high FE_{CO} at larger current densities in the future study. Thus we can collect more actual output of CO to consider about further application. Error bars of the current densities of other ratios Pd-Cu alloys are shown in Fig.3.11. The currents decrease with increasing the Cu amount alloyed with Pd and all the error bars also keep within modest regions.

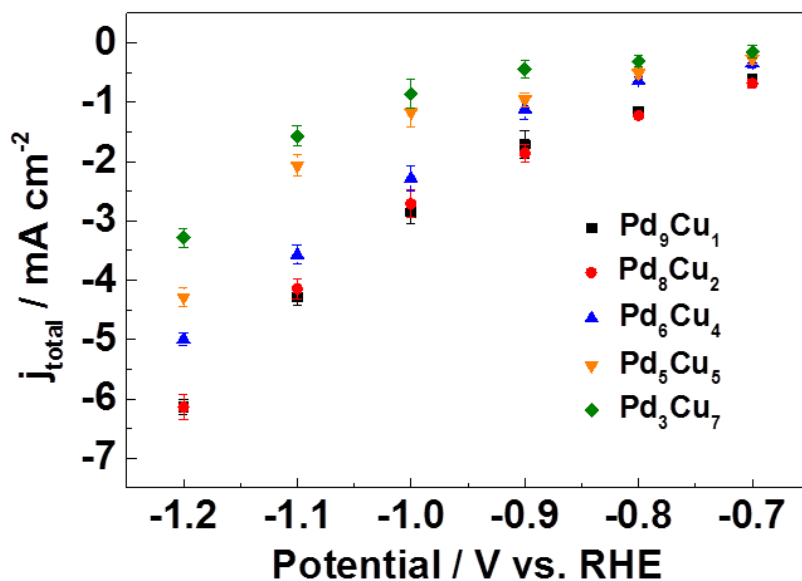


Fig. 3.11 Current densities of other ratios Pd-Cu alloys with error bars.

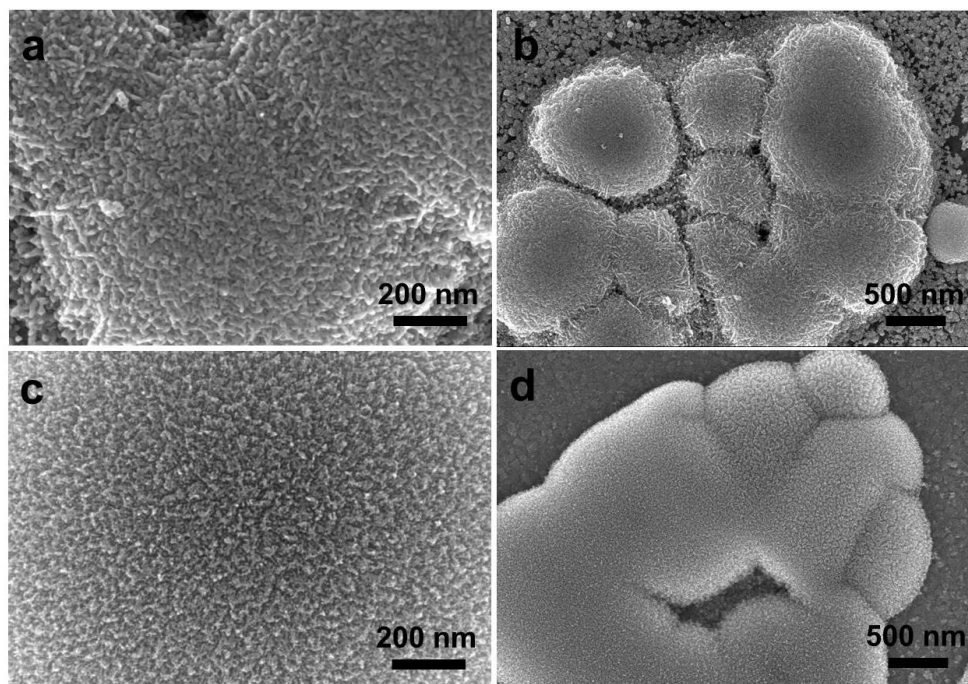


Fig. 3.12 Top-surface SEM images of a) and b) N-Pd₇Cu₃ prepared without surfactant; c) and d) M-Pd₇Cu₃ prepared with surfactant.

Thus, to evaluate the effectiveness of mesoporous nanostructure on the selectivity of CO₂ reduction, nanoparticle counterpart Pd₇Cu₃ was prepared by the same electrodeposition method without surfactant Brij 58. The morphology comparison of the nanoparticle Pd₇Cu₃ (N-Pd₇Cu₃) and mesoporous Pd₇Cu₃ (M-Pd₇Cu₃) are shown in Fig. 3.12. Without Brij 58, the alloy electrocatalyst tend to form a bulk nanoparticle structure, which is accumulated by numerous tiny nanoparticles.

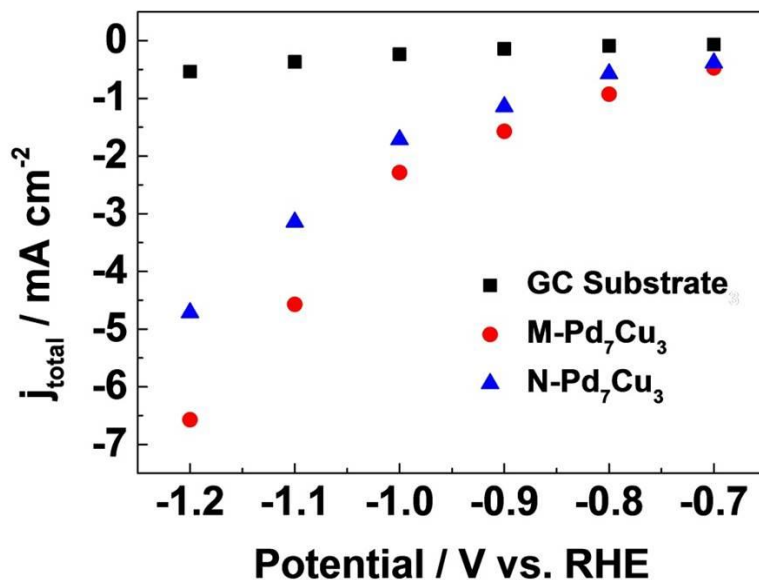


Fig. 3.13 Comparison of total current density between mesoporous Pd₇Cu₃ electrocatalyst (M-Pd₇Cu₃) and nanoparticle Pd₇Cu₃ electrocatalyst (N-Pd₇Cu₃).

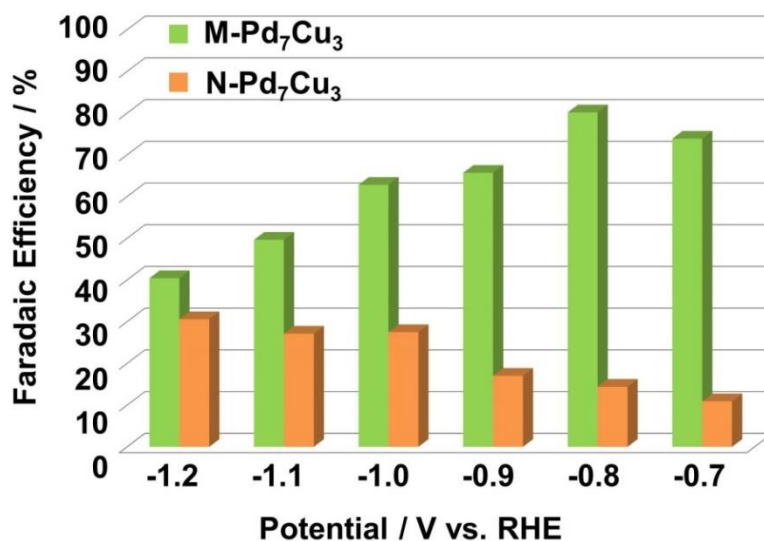


Fig. 3.14 Faradaic efficiency for CO of M-Pd₇Cu₃ and N-Pd₇Cu₃.

Fig. 3.13 exhibits the total current density difference between M-Pd₇Cu₃ and N-Pd₇Cu₃. M-Pd₇Cu₃ shows obviously much larger current density than the nanoparticle counterpart. Their corresponding FEs for CO are contrasted in Fig. 3.14. N-Pd₇Cu₃ demonstrate much smaller FE for CO at all the applied potential region, especially at lower potentials. In addition, the FE_{CO} over N-Pd₇Cu₃ increases with the applied potential, whereas M-Pd₇Cu₃ exhibits nonlinear relationship of FE_{CO} with the bias. The highest FE_{CO} over M-Pd₇Cu₃ is obtained at lower potential -0.8 V vs. RHE, and the FE_{CO} decreases with raising the applied bias. It can be deduced that M-Pd₇Cu₃ and N-Pd₇Cu₃ go through different mechanism during the CO₂ reduction process and M-Pd₇Cu₃ possesses much lower overpotential. It has been reported that active sites dominate the selectivity of CO₂ reduction by adjusting the reaction mechanism and the rate-determining step.^{6, 12} Edge sites are believed as the most desirable active sites for the selective reduction of CO₂ to CO by facilitating the stabilization of the reduction intermediates (such as COOH*) and the formation of CO.⁶ And by roughening the surface, active sites (in particular edge sites) could be effectively multiplied.¹⁷

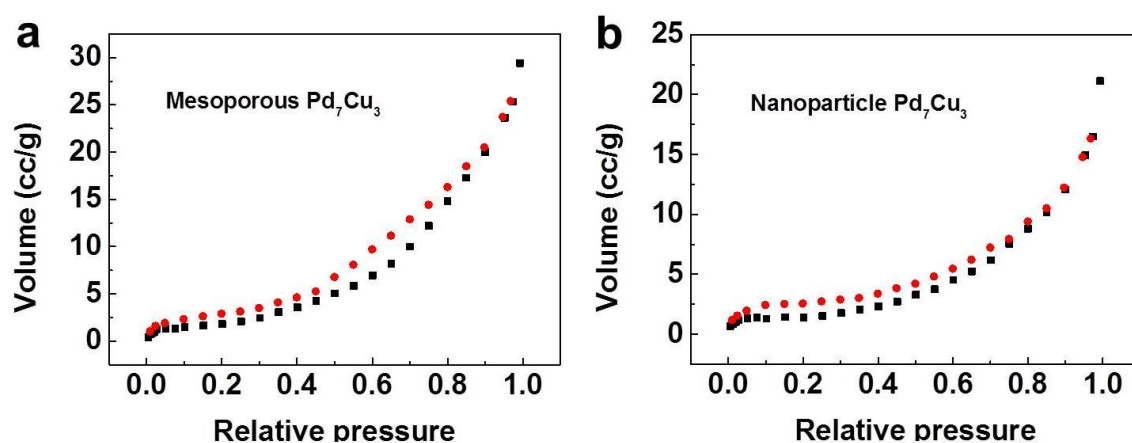


Fig. 3.15 Nitrogen adsorption-desorption isotherm of a) mesoporous Pd₇Cu₃ and b) nanoparticle Pd₇Cu₃.

The specific surface areas of M-Pd₇Cu₃ and N-Pd₇Cu₃ were determined by the Brunauer-Emmett-Teller (BET) method as shown in Fig. 3.15. M-Pd₇Cu₃ gives a much larger surface area (17.6 m² g⁻¹) than N-Pd₇Cu₃ (9.6 m² g⁻¹), which is attributed to its superior porous structure. The relative small specific surface area of mesoporous Pd₇Cu₃ can be ascribed to the high density of metal samples. Usually the specific surface area of semiconductor materials can be characterized over 100 m² g⁻¹, while the values of metal samples are much lower than semiconductors due to density differences. Our detected specific surface area of mesoporous Pd₇Cu₃ (17.6 m² g⁻¹) exhibited similar value to the previous reported mesoporous Pt (14 ~ 22 m² g⁻¹).²⁵⁻²⁷ In addition, the disordered mesopores with divergent structure might be the other reason for the low specific surface area. The surface area and pore size decrease gradually from the surface to the inner side of the mesoporous particles.

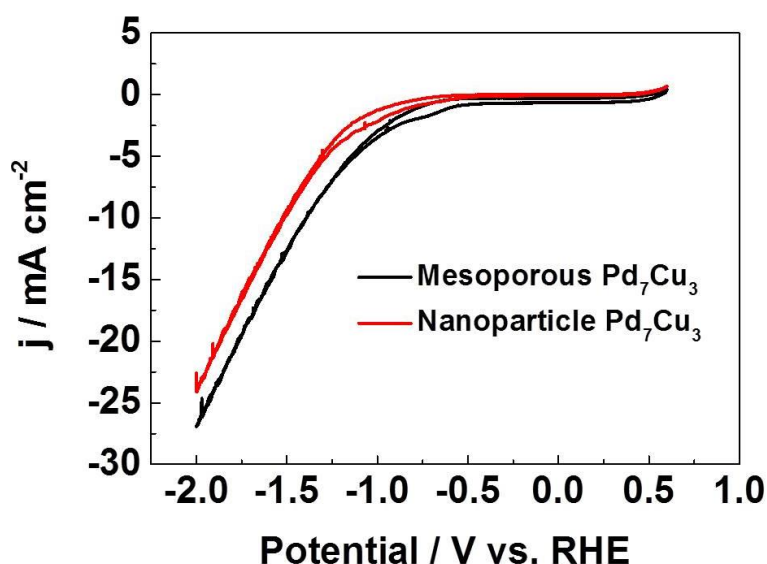


Fig. 3.16 Cyclic voltammograms of mesoporous Pd₇Cu₃ and nanoparticle Pd₇Cu₃ in 0.1 M CO₂ saturated KHCO₃ solution at a scan rate of 100 mV s⁻¹ from 0.6 V to -2.0 V.

To confirm these enlarged surface area contributes to the active sites, cyclic voltammetry were performed in a CO₂ saturated KHCO₃ solution as shown in Fig. 3.16. The cathodic current of M-Pd₇Cu₃ starts at more positive potential and a peak of CO₂ reduction can be observed at -0.7 V vs. RHE. Moreover, M-Pd₇Cu₃ shows larger peak and current density at the potential region of CO₂ reduction, which should be due to the presence of more active sites within the specific mesoporous architecture. Thus, it can be deduced that mesoporous nanostructure benefits the CO₂ reduction by providing more active sites than the nanoparticle counterpart. Moreover, the surface composition of M-Pd₇Cu₃ and N-Pd₇Cu₃ was examined by XPS as shown in Fig. 3.17. The surface composition Pd:Cu was determined as 54:46 and 30:70 for M-Pd₇Cu₃ and N-Pd₇Cu₃, respectively. Both the Pd:Cu ratios are lower than the stoichiometric concentration Pd₇Cu₃ in the starting electrolytes. The surface composition of M-Pd₇Cu₃ is also lower than the ICP-OES result (Fig. 3.3). It can be deduced that the total compositional ratio within the mesoporous Pd-Cu alloy accords well with the stoichiometric concentration in the starting electrolytes, while the surface composition is different from the total alloy compositional ratio. This difference can be ascribed to the deposition potential gap ($E_{Pd} = 0.951V$, $E_{Cu} = 0.342 V$) between Pd and Cu as well as the long deposition time (600 s) of our preparation process. Pd was more primarily reduced than Cu during the initial period of deposition process. With Pd concentration decreasing gradually in the electrolyte solution, more Cu became to be deposited and thus exhibited lower Pd:Cu ratio than the stoichiometric concentration 7:3 at the surface. The SEM images (Fig. 3.2) shows that the mesoporous morphology highly depend on the Pd:Cu ratio. It exhibits perfect mesoporous surface when Pd is the dominant component, which can be

deduced that the surfactant Brij 58 preferably interacts with Pd. So that Brij 58 could balance the deposition rate gap between Pd and Cu. Thus, the surface composition of M-PdCu (54:46) shows high Pd:Cu ratio than N-PdCu (30:70). This result also accord with the DFT calculations in the following part.

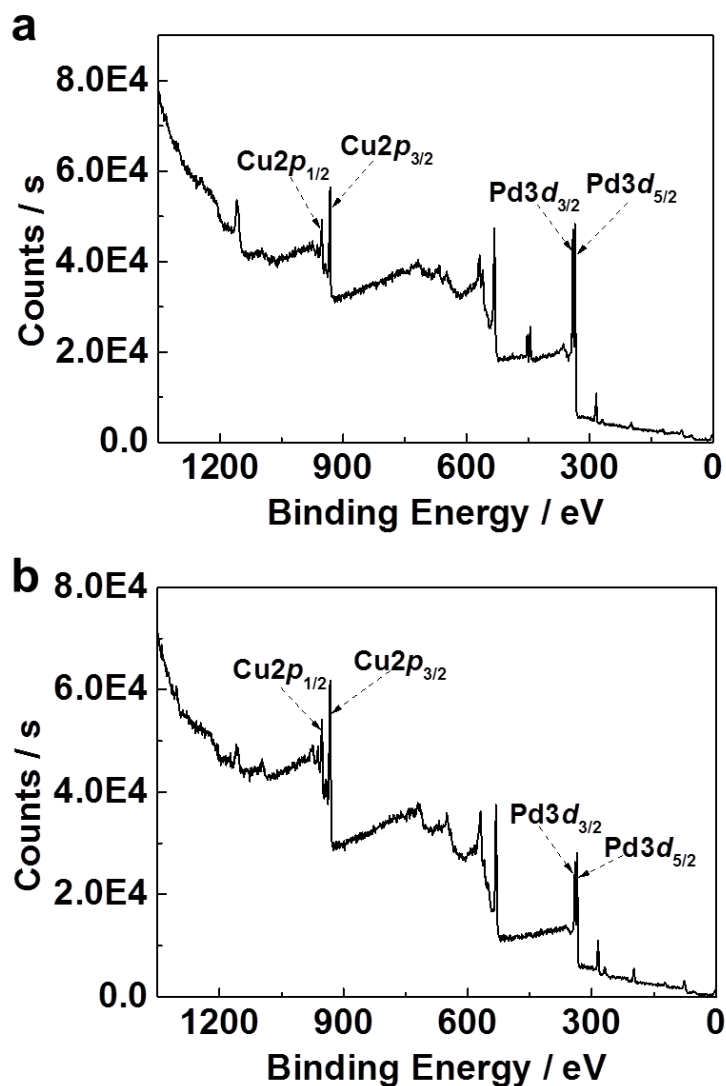


Fig. 3.17 XPS spectra of PdCu bimetallic electrocatalysts a) with and b) without surfactant.

3.3.3 The effectiveness of compositional ratio on the selectivity of CO₂ reduction

The experimental data of CO selectivity over the series of mesoporous PdCu bimetallic electrocatalysts also exhibit strong dependence on the compositional ratios. Fig. 3.18 shows the Faradaic efficiencies (FEs) for the two main products CO and H₂ at the applied potential region from -0.7 V to -1.2 V vs. RHE. Pure Pd exhibits similar FEs for CO and H₂ at almost all the applied potential region (FEs \approx 30% ~ 40%) as shown in Fig. 3.18a, while pure Cu demonstrates much higher H₂ evolution FE than the FE for CO as exhibited in Fig. 3.18h. With alloying Pd with Cu gradually, the trends in FEs for CO and H₂ vary greatly for all the mesoporous bimetallic electrocatalysts. CO becomes the dominant product when the mesoporous bimetallic alloy contains more Pd than Cu (Fig. 3.18b-3.18f). As the Cu ratio increases to a majority component, the FEs for CO decreases dramatically. H₂ turns into the major product and also a small amount of methane can be detected as a product as shown in Fig. 3.18g. It is clear that the compositional ratio of the mesoporous bimetallic alloy significantly alters the electrocatalytic activity of the selective reduction of CO₂ to CO. Fig. 3.19 exhibits a volcano relation of the CO productivity with the Pd-Cu ratio at -0.8 V vs. RHE. The optimal composition appears at Pd₇Cu₃, in which the FE for CO exceeds 80% at -0.8 V vs. RHE.

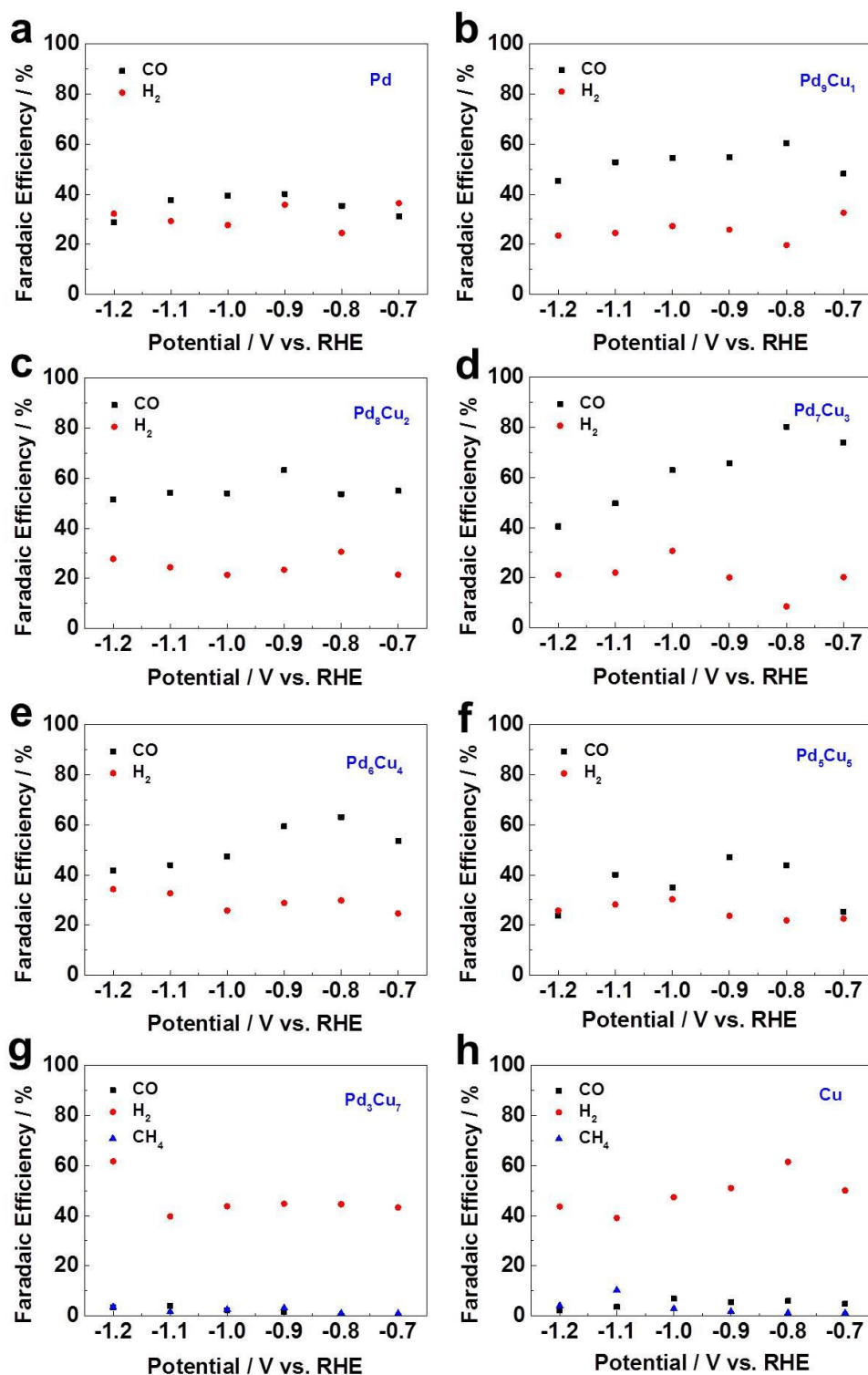


Fig. 3.18 Faradaic efficiencies of the series of mesoporous palladium-copper bimetallic electrocatalysts for the two main products of CO and H₂: a) pure Pd, b) Pd₉Cu₁, c) Pd₈Cu₂, d) Pd₇Cu₃, e) Pd₆Cu₄, f) Pd₅Cu₅, g) Pd₃Cu₇ and h) pure Cu.

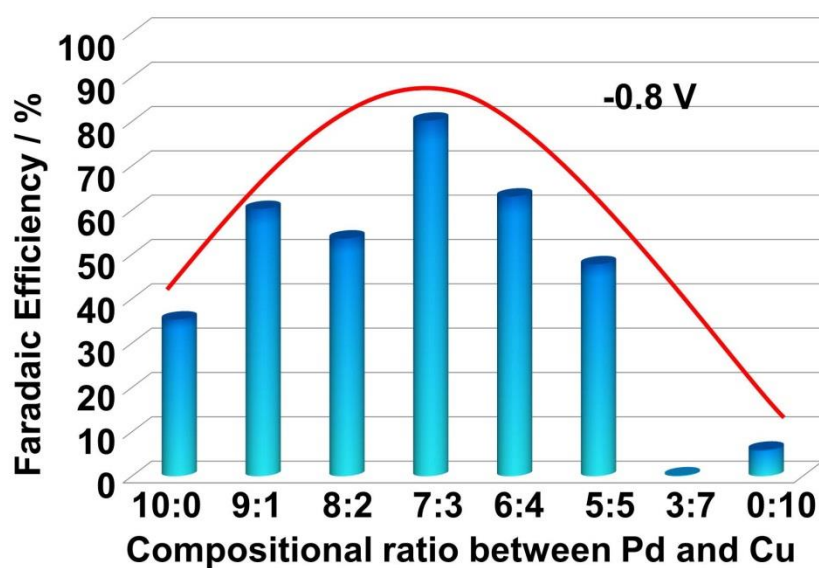


Fig. 3.19 Faradaic efficiency comparison of mesoporous Pd-Cu electrocatalysts with different ratio at -0.8 V vs. RHE.

Alloy materials are extremely cited for their uniquely geometric and electronic effects in enhancing electrocatalytic activities.¹¹ The geometric effect is believed in relating to the atomic arrangement at the active site and so that determines the catalytic activity.²⁸ On the other hand, the electronic effect significantly affects the binding strength of intermediates by adjusting the electronic structure of the catalysts. The binding strength for intermediates COOH* and CO is largely at the discretion of the d-band lying, which is relative to the Fermi level and due to the occupancy of anti-bonding states.²⁹ XPS spectra in Fig. 3.20 could illustrate the interaction between Pd and Cu as evidence. Both of the Pd 3d and Cu 2p peaks shift with the ratio changes, which can be ascribed to the electron transfer between Pd and Cu atoms during the formation of bimetallic alloys.³⁰

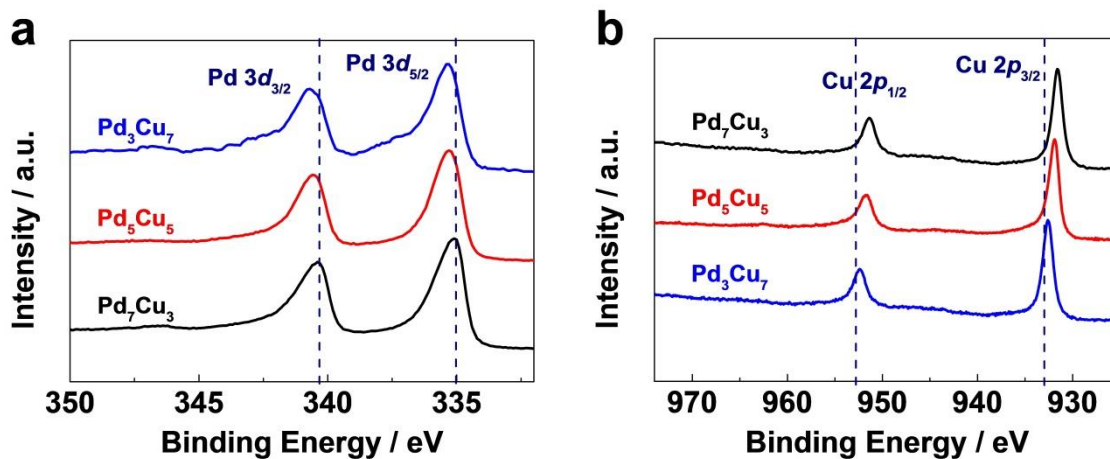


Fig. 3.20 XPS spectra of mesoporous PdCu bimetallic electrocatalysts: a) Pd $3d$ b) Cu $2p$. The dash line (...) marks the peak position of monometallic Pd and Cu.

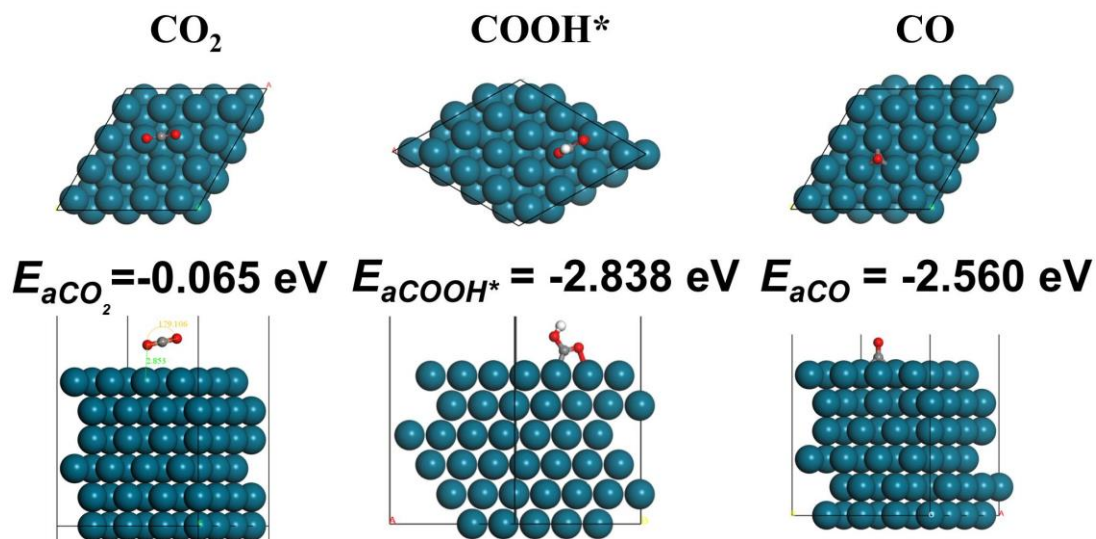


Fig. 3.21 Optimized geometries and adsorption energies of CO₂, COOH* intermediate and CO on the Pd (111) facet.

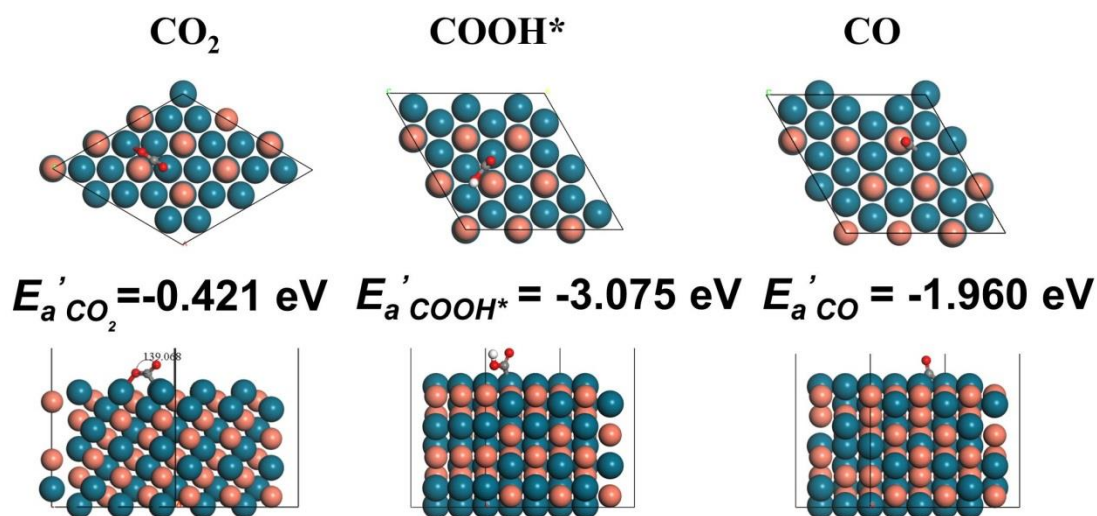


Fig. 3.22 Optimized geometries and adsorption energies of CO_2 , $COOH^*$ intermediate and CO on the Pd-terminated PdCu (111) facet.

DFT calculations were performed to reveal the effect of Pd-Cu alloy on altering the adsorption properties of the reactant target CO_2 , the intermediates $COOH^*$ and the desirable product CO . The well-defined structure of Pd-Cu was adopted to simulate the adsorption energy change on Pd atoms and Cu atoms after forming the Pd-Cu alloy.³¹ Fig. 3.21 and Fig. 3.22 exhibit the models of CO_2 , $COOH^*$ and CO adsorption on Pd (111) and Pd-terminated Pd-Cu (111) facets, and their corresponding adsorption energies. More negative adsorption energy means much stronger adsorption ability on the electrocatalysts surface as summarized in Table 3.2. For the reactant target CO_2 , the adsorption energy changes from -0.065 eV on Pd (111) surface to -0.421 eV on Pd-terminated Pd-Cu (111) surface, which indicates a much strong adsorption capacity of Pd-terminated alloy. In the case of $COOH^*$ intermediate, strong exothermic adsorptions were observed with negative adsorption energies of -2.838 eV and -3.075 eV on Pd (111) and Pd-terminated Pd-Cu (111) surfaces, respectively. The stability of $COOH^*$ intermediates rises obviously within Pd-terminated alloy, which could possibly

restrain the trend to release HOOCH.¹² Cooperating with the CO facilitative mesoporous nanostructure, the production of formic acid can be effectively suppressed.

Table 3.2 Calculated adsorption energies for CO₂, COOH* intermediate and CO on Pd (111), Pd-terminated Pd-Cu (111), Cu (111) and Cu-terminated Pd-Cu (111) facet.

	CO ₂ / eV	COOH* / eV	CO / eV
Pd (111)	-0.065	-2.838	-2.560
Pd-terminated Pd-Cu (111)	-0.421	-3.075	-1.960
Cu (111)	-0.037	-2.280	-1.270
Cu-terminated Pd-Cu (111)	-2.202	-2.470	-1.840

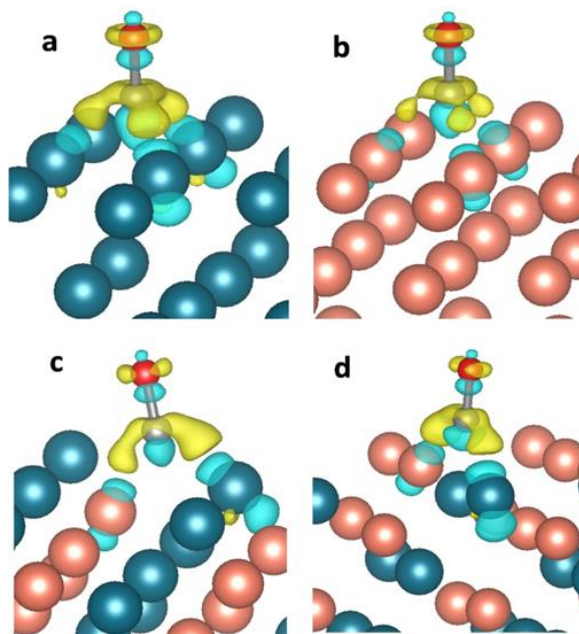


Fig. 3.23 The difference charge density of CO adsorption configuration on a) Pd (111), b) Cu (111), c) Pd- and d) Cu-terminated Pd-Cu (111) surfaces. Herein, yellow and cyan colors indicate charge increase and decrease, respectively.

Moreover, consistent with the previous reports,^{32,33} by alloying Pd with Cu, the CO adsorption energy raises from -2.560 eV on Pd (111) to -1.960 eV on Pd-terminated Pd-Cu (111), which shows the CO desorption ability increases significantly (Fig. 3.23). This suggests that Cu atoms could alter the binding strength for CO of their adjacent Pd atoms, and thus facilitate the product CO release from Pd atoms. The free energy diagram could also contribute to this conclusion as shown in Fig. 3.24. It reveals that the presence of Cu improves the CO₂ and COOH* stabilities on Pd notably and promotes the desorption of CO as well, which thus benefit to the selective reduction of CO₂ to CO and suppress the competing reaction favorably.¹²

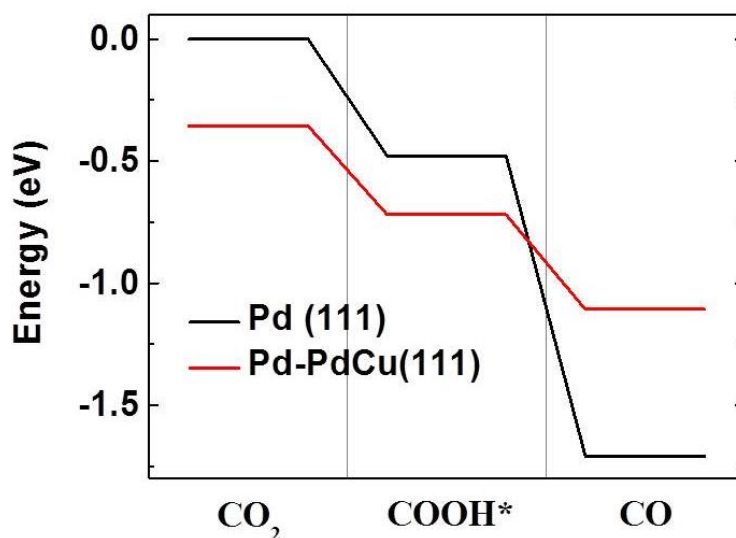


Fig. 3.24 Free energy diagram of CO₂, COOH* intermediate, CO on Pd (111) and Pd-terminated Pd-Cu (111) facet

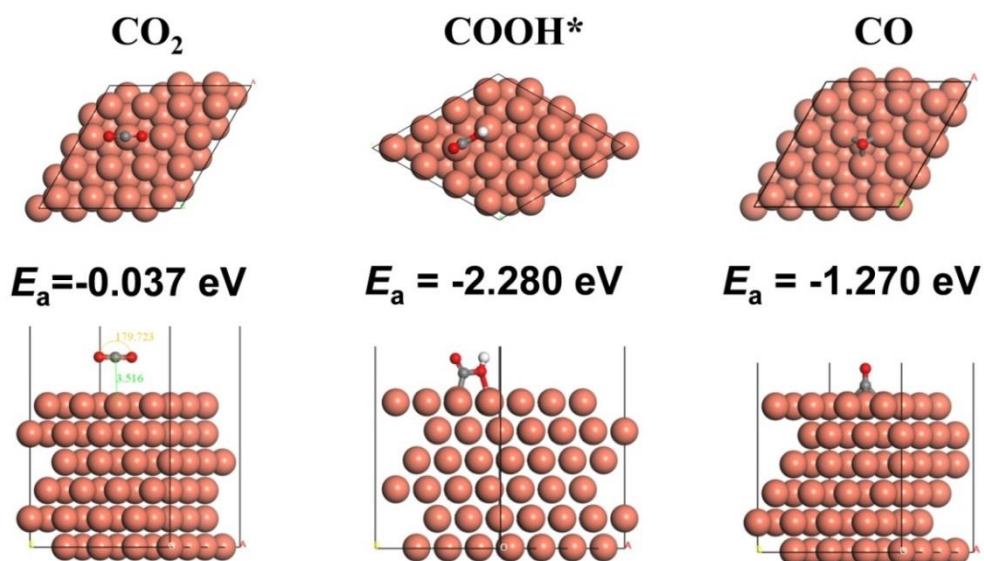


Fig. 3.25 Optimized geometries and adsorption energies of CO_2 , COOH^* intermediate and CO on the Cu (111) facet.

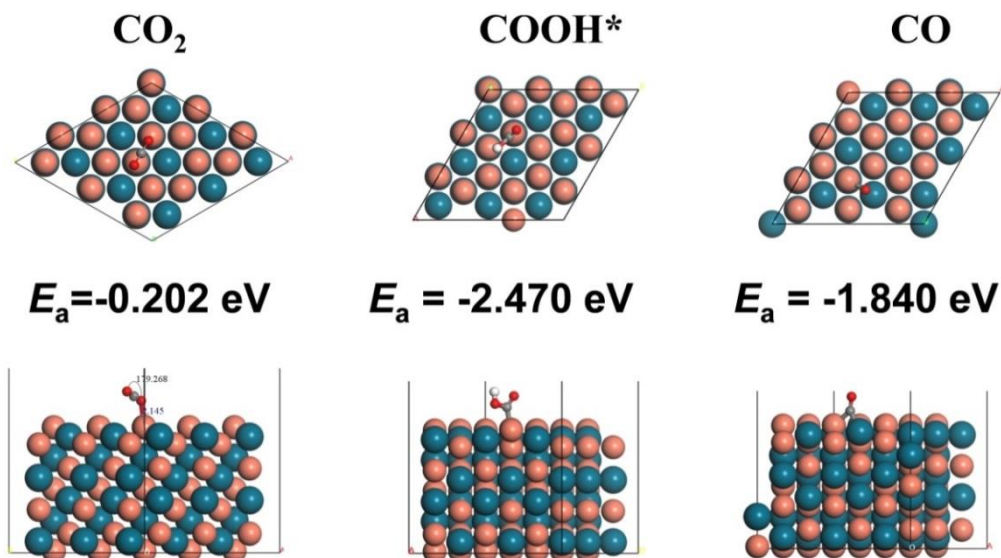


Fig. 3.26 Optimized geometries and adsorption energies of CO_2 , COOH^* intermediate and CO on the Cu -terminated PdCu (111) facet.

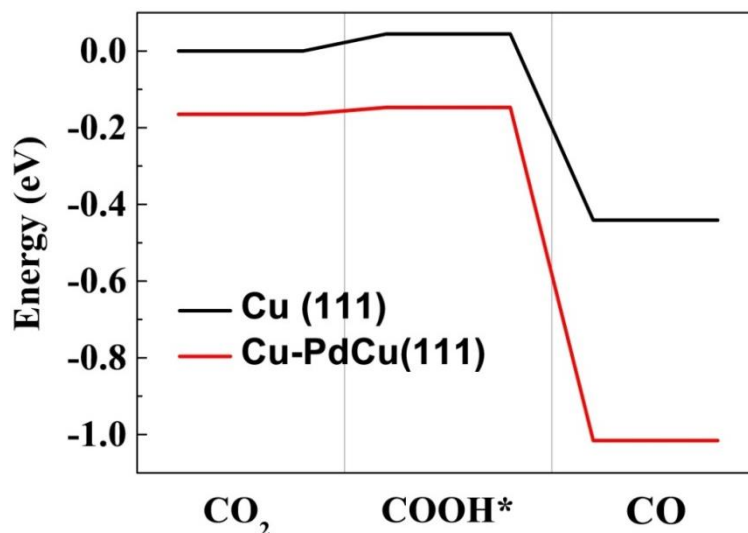


Fig. 3.27 Free energy diagram of CO₂, COOH* intermediate, CO on Cu (111) and Cu-terminated Pd-Cu (111) facet.

The models of CO₂, COOH* and CO adsorption on Cu (111) facet as well as on the Cu-terminated Pd-Cu (111) facet are shown in Fig. 3.25 and Fig. 3.26, respectively. The adsorption energies of CO₂, COOH* also decrease obviously on the Cu atoms within Pd-Cu alloy (111) facet as summarized in Table 3.2. However, the CO release ability on Cu atoms declines as well. The corresponding free energy diagram also exhibit the same trend as shown in Fig. 3.27. This suggests that Cu atoms are not the appropriate reactive centers for the selective CO₂ reduction to CO, but probably could absorb CO to the further multi-electron reductions.³⁴ It consequently could explain the appearance of methane in the products when Cu presents the majority component in the Pd-Cu alloys.

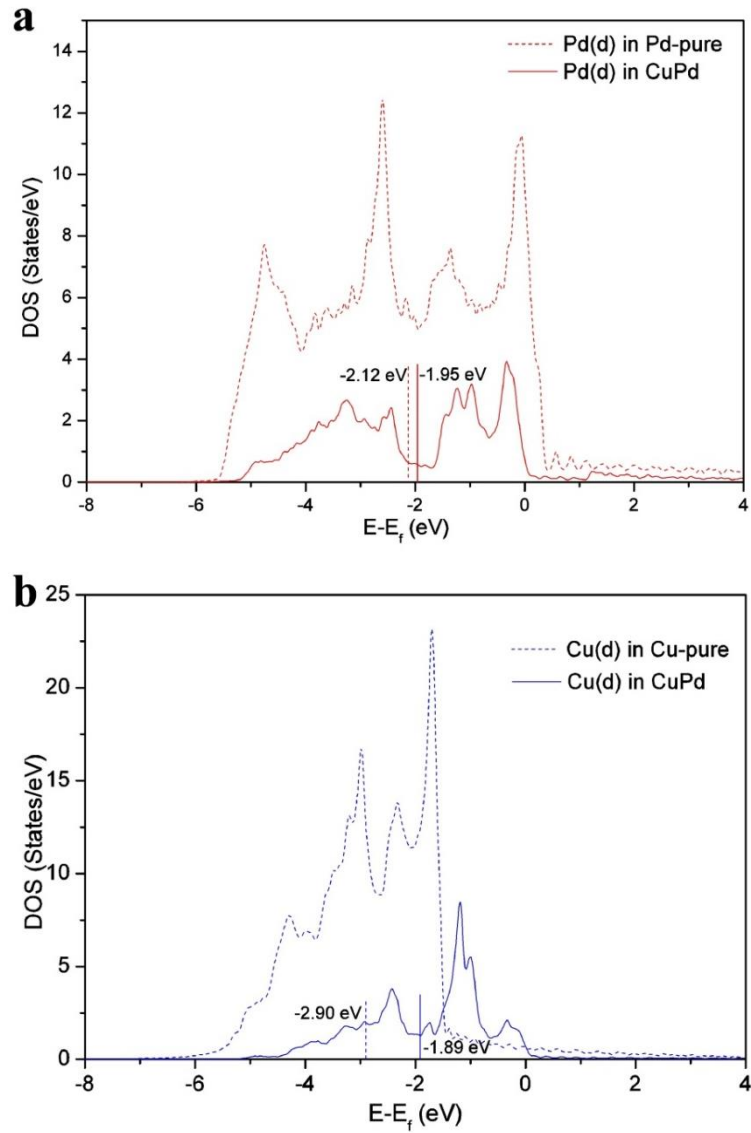


Fig. 3.28 Projected d-states in Pd-Cu, pure Pd and pure Cu: a) projected d-states of Pd in pure Pd and Pd-Cu; b) projected d-states in pure Cu and Pd-Cu. The positions of d-band centers are illustrated.

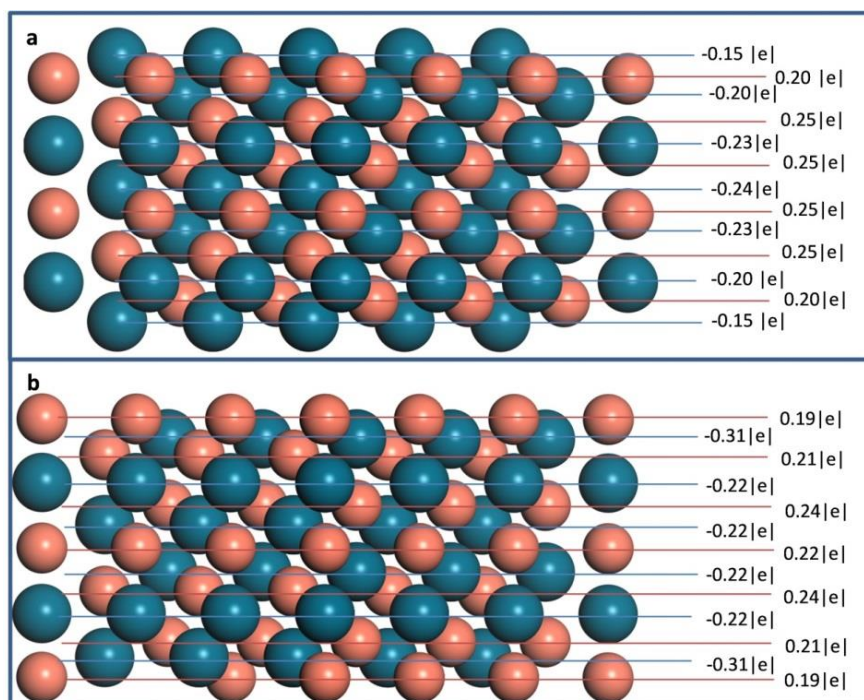


Fig. 3.29 Calculated Bader charge difference referenced to elemental phase of each metal for the Pd- (a) and Cu-terminated (b) Pd-Cu (111) surfaces. $|e|$: elementary charge

Comparison of the projected density of states (pDOS) of pure metals (Cu and Pd) and of Pd-Cu alloy shows that the electronic structures of Cu and Pd were changed by the alloying. It was found that the d-band centers of Cu and Pd in Pd-Cu alloy are higher than those in pure metals as shown in Fig. 3.28, which explains stronger adsorption of CO_2 and COOH^* on Pd-terminated Pd-Cu (111),³⁵ while the weaker adsorption of CO on Pd-terminated Pd-Cu (111) is attributed to the geometrical restriction in the formation of C-Pd bonds on the surface (Fig. 3.23). Bader charge calculation shows that Pd atoms possess negative charge while Cu atoms have positive charge with respect to those of elemental phase of each metal as illustrated in Fig. 3.29.³⁶ Thus it indicates an electron transfer from Cu to Pd in Pd-Cu alloy due to the different electronegativity. The average electron transfer from Cu to Pd is calculated as $0.24 |e|$ in the bulk alloy.

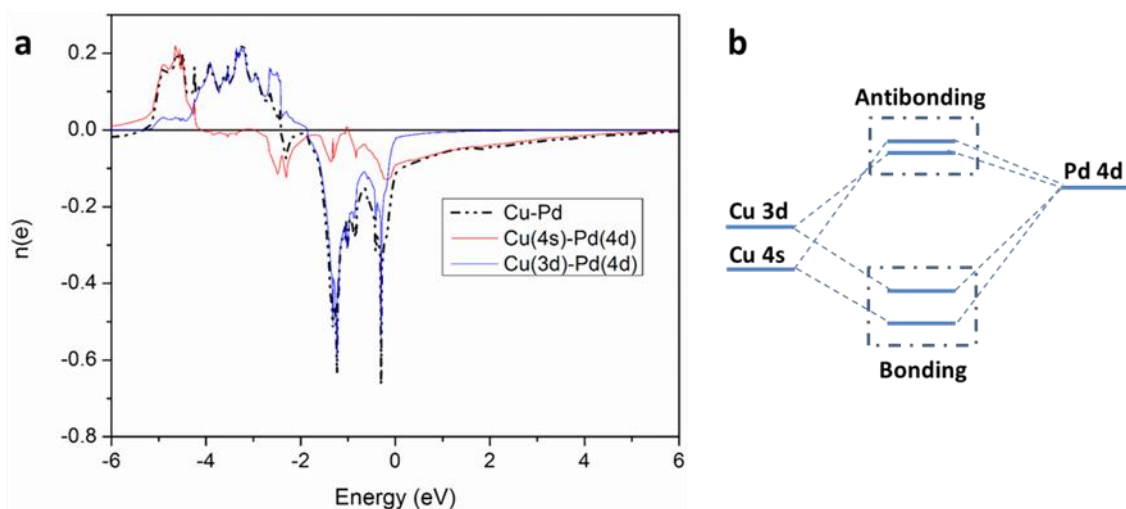


Fig. 3.30 a) Calculated Crystal orbital overlap populations (COOP) for Pd-Cu alloy, b) Energy level diagram for Pd-Cu interaction.

Crystal orbital overlap populations (COOP) was calculated to reveal the orbital configuration of Pd-Cu alloy as shown in Fig. 3.30. The COOP is a density-of-states-weighted overlap population between two orbital centers, and its positive and negative regions represent bonding and antibonding interactions, respectively. Fig. 3.30a shows the orbital-decomposed COOP analysis for Pd-Cu interaction. It reveals that the Pd-Cu interaction is dominantly composed of Cu(4s)-Pd(4d) and Cu(3d)-Pd(4d) interactions. The COOP analysis allows us to construct the corresponding energy level diagrams for the Cu-Pd interaction as shown in Fig. 3.30b. It shows that Cu(4s) electron takes a majority of the electrons transferred from Cu to Pd and Cu(3d) electron contributes to minority part.

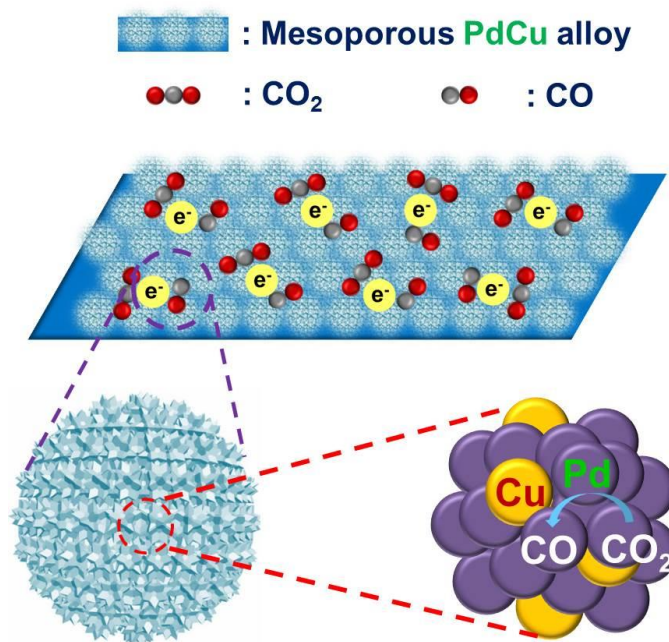


Fig. 3.31 Schematic model of the CO₂ reduction process over mesoporous Pd₇Cu₃.

Thus, combining the calculation results of adsorption energy, free energy and surface electrons transfer in Pd-Cu alloy, it can be deduced that the reactive centers for the selective CO₂ reduction to CO within the Pd-Cu alloys are on the Pd atoms as the schematic model illustrated in Fig. 3.31. In addition, although Cu atoms do not serve as reactive centers, they could still contribute to the activity enhancement by altering the electronic structure of their neighboring Pd and adjusting the atomic arrangement at the active sites. Accordingly, the electronic effect and geometric effect synergistically result in a volcano-like CO productivity, which correlated with the compositional ratio in the mesoporous Pd-Cu bimetallic electrocatalysts. The optimal ratio (Pd₇Cu₃) is obtained when Pd is the dominant component.

3.4 Conclusions

In conclusion, this study shows that a series of mesoporous palladium-copper bimetallic electrocatalysts with a superior activity and high FE were fabricated via a facile electrodeposition method for the selective reduction of CO₂ to CO. The optimal ratio is obtained at Pd₇Cu₃, with FE_{CO} exceeding 80% at -0.8 V vs. RHE. DFT calculations suggest that the highly selective CO formation is due to the geometric and electronic effects within the palladium-copper bimetallic alloys. Pd atoms serve as the reactive centers with an enhanced CO₂, COOH* adsorption ability and CO desorption ability in the presence of Cu. Cu atoms only contribute to the activity by altering the electronic structure of their neighbor Pd and adjusting the atomic arrangement at the active sites. Moreover, the mesoporous nanostructure could provide more active sites for the selective reduction of CO₂ to CO by effectively roughening the surface and enlarging the active surface area.

References

1. C. W. Li, J. Ciston and M. W. Kanan, *Nature*, 2014, **508**, 504-507.
2. K. Nakata, T. Ozaki, C. Terashima, A. Fujishima and Y. Einaga, *Angew. Chem. Int. Ed.*, 2014, **53**, 871-874.
3. B. Kumar, M. Llorente, J. Froehlich, T. Dang, A. Sathrum and C. P. Kubiak, *Annu. Rev. Phys. Chem.*, 2012, **63**, 541-569.
4. Q. Lu, J. Rosen, Y. Zhou, G. S. Hutchings, Y. C. Kimmel, J. G. Chen and F. Jiao, *Nat. Commun.*, 2014, **5**, 3242.
5. Y. Chen, C. W. Li and M. W. Kanan, *J. Am. Chem. Soc.*, 2012, **134**, 19969-19972.
6. W. Zhu, R. Michalsky, Ö. Metin, H. Lv, S. Guo, C. J. Wright, X. Sun, A. A. Peterson and S. Sun, *J. Am. Chem. Soc.*, 2013, **135**, 16833-16836.

7. H. Mistry, R. Reske, Z. Zeng, Z.-J. Zhao, J. Greeley, P. Strasser and B. R. Cuenya, *J. Am. Chem. Soc.*, 2014, **136**, 16473-16476.
8. B. A. Rosen, A. Salehi-Khojin, M. R. Thorson, W. Zhu, D. T. Whipple, P. J. A. Kenis and R. I. Masel, *Science*, 2011, **334**, 643-644.
9. J. Medina-Ramos, R. C. Pupillo, T. P. Keane, J. L. DiMeglio and J. Rosenthal, *J. Am. Chem. Soc.*, 2015, **137**, 5021-5027.
10. J. L. DiMeglio and J. Rosenthal, *J. Am. Chem. Soc.*, 2013, **135**, 8798-8801.
11. D. Kim, J. Resasco, Y. Yu, A. M. Asiri and P. Yang, *Nat. Commun.*, 2014, **5**, 4948.
12. S. Rasul, D. H. Anjum, A. Jedidi, Y. Minenkov, L. Cavallo and K. Takanebe, *Angew. Chem. Int. Ed.*, 2015, **54**, 2146-2150.
13. M. Azuma, K. Hashimoto, M. Hiramoto, M. Watanabe and T. Sakata, *J. Electrochem. Soc.*, 1990, **137**, 1772-1778.
14. J. Lee, Y. Kwon, R. L. Machunda and H. J. Lee, *Chem. Asian J.*, 2009, **4**, 1516-1523.
15. C. Li, T. Sato and Y. Yamauchi, *Angew. Chem. Int. Ed.*, 2013, **52**, 8050-8053.
16. Y. Yamauchi, A. Tonegawa, M. Komatsu, H. Wang, L. Wang, Y. Nemoto, N. Suzuki and K. Kuroda, *J. Am. Chem. Soc.*, 2012, **134**, 5100-5109.
17. W. Tang, A. A. Peterson, A. S. Varela, Z. P. Jovanov, L. Bech, W. J. Durand, S. Dahl, J. K. Norskov and I. Chorkendorff, *Phys. Chem. Chem. Phys.*, 2012, **14**, 76-81.
18. C. Li and Y. Yamauchi, *Chem. Eur. J.*, 2014, **20**, 729-733.
19. C. Li, M. Imura and Y. Yamauchi, *Phys. Chem. Chem. Phys.*, 2014, **16**, 8787-8790.
20. C. Li, B. Jiang, M. Imura, V. Malgras and Y. Yamauchi, *Chem. Commun.*, 2014, **50**, 15337-15340.
21. K. Baba, U. Miyagawa, K. Watanabe, Y. Sakamoto and T. B. Flanagan, *J. Mater. Sci.*, 1990, **25**, 3910-3916.

22. J. Mao, Y. Liu, Z. Chen, D. Wang and Y. Li, *Chem. Commun.*, 2014, **50**, 4588-4591.
23. X. Min and M. W. Kanan, *J. Am. Chem. Soc.*, 2015, **137**, 4701-4708.
24. C. W. Li and M. W. Kanan, *J. Am. Chem. Soc.*, 2012, **134**, 7231-7234.
25. S. A. G. Evans, J. M. Elliott, L. M. Andrews, P. N. Bartlett, P. J. Doyle and G. Denuault, *Analytical Chemistry*, 2002, **74**, 1322-1326.
26. X. Teng, X. Liang, S. Maksimuk and H. Yang, *Small*, 2006, **2**, 249-253.
27. S. Tominaka, C.-W. Wu, T. Momma, K. Kuroda and T. Osaka, *Chem. Commun.*, 2008, DOI: 10.1039/B803225D, 2888-2890.
28. S. Siahrostami, A. Verdaguier-Casadevall, M. Karamad, D. Deiana, P. Malacrida, B. Wickman, M. Escudero-Escribano, E. A. Paoli, R. Frydendal, T. W. Hansen, I. Chorkendorff, I. E. L. Stephens and J. Rossmeisl, *Nat. Mater.*, 2013, **12**, 1137-1143.
29. J. K. Nørskov, T. Bligaard, J. Rossmeisl and C. H. Christensen, *Nat. Chem.*, 2009, **1**, 37-46.
30. C. Hu, X. Zhai, Y. Zhao, K. Bian, J. Zhang, L. Qu, H. Zhang and H. Luo, *Nanoscale*, 2014, **6**, 2768-2775.
31. M. Yamauchi and T. Tsukuda, *Dalton Trans.*, 2011, **40**, 4842-4845.
32. T. D. Pope, K. Griffiths and P. R. Norton, *Surf. Sci.*, 1994, **306**, 294-312.
33. F. Illas, N. López, J. M. Ricart, A. Clotet, J. C. Conesa and M. Fernández-García, *J. Phys. Chem. B*, 1998, **102**, 8017-8023.
34. X. Nie, M. R. Esopi, M. J. Janik and A. Asthagiri, *Angew. Chem. Int. Ed.*, 2013, **52**, 2459-2462.
35. B. Hammer, Y. Morikawa and J. K. Nørskov, *Phys. Rev. Lett.*, 1996, **76**, 2141-2144.
36. W. Tang, E. Sanville and G. Henkelman, *J. Phys.: Condens. Matter*, 2009, **21**, 084204.

Chapter 4 Design of Hierarchical Nanowire Arrays Photoanodes Based on Carbon Nanotubes and Co_3O_4 Decorated ZnO Composite for the Oxidation Half Reaction of Photoelectrochemical CO_2 Conversion

4.1 Introduction

Photoelectrochemical (PEC) reduction of CO_2 appears as a promising way to capture and store the solar energy as well as to produce renewable fuels by simulating the natural photocatalysis process.^{1,2} Between the two half reactions of PEC CO_2 reduction, water oxidation reaction possess a specific status. Because it is not only the anodic reaction of liquid phase conversion of CO_2 , but also would dominate the total activities.^{3,4} In this regard, it is still a challenging target for preparation photoanodes using cost-effective semiconductor materials with high energy conversion efficiency.

Semiconductor nanowires (NWs) have been studied extensively for over two decades for their promising electronic, photonic, thermal, electrochemical and mechanical properties.^{5,6} It is possible to achieve a large-scale implementation of solar-to-fuel energy conversion by taking the advantages of nanowire materials, such as large surface area, reduced electrochemical overpotential, enhanced light absorption and improved charge collection. In particular, ZnO nanowires with tuneable alignment and morphology have been attracting great deal of attention due to their prospective electronic and optical properties. Additionally, the typical electron mobility in ZnO is 10~100 times higher than that in TiO_2 , so the electrical resistance is much lower and the electron-transfer efficiency is higher

than TiO_2 .⁷⁻¹⁰ Despite great efforts have been reported for the synthesis and application of ZnO NWs arrays, there is still some drawbacks accompanied by ZnO photocatalysts, such as the photocorrosion induced by photogenerated holes and the slow interfacial kinetics for water oxidation.^{11, 12} Thus, it is highly desirable to improve the photogenerated charges separation and accelerate the reaction rates of water oxidation.

The integration of photo-absorbing substrate with effective charge conductor materials appears a favourable way to overcome these disadvantages and enhance the efficiency of PEC water oxidation. The hierarchical nanostructure would benefit the PEC water oxidation by reducing the external power consumption, depressing the photogenerated charge recombination and facilitating the interface charge transfer.¹³⁻¹⁵ Co_3O_4 bears the responsibility of efficient O_2 evolution and long durability against chemical- and photo-corrosion, and has been widely employed as low cost catalyst or cocatalyst for robust water oxidation in electrochemical and PEC water splitting.¹⁶⁻¹⁹ Besides, Carbon nanotubes (CNTs) possess unique electrical and optical properties that make them an ideal candidate for charge separation, transport, and collection in photovoltaics due to their conspicuous merits in improving the photoconversion efficiency.²⁰⁻²²

In this chapter, a facile design and fabrication of hierarchical nanowire arrays photoanodes based on CNTs and Co_3O_4 decorated ZnO was synthesised via a stepwise preparation process including chemical soaking and electrosynthesis method. Different amount of CNTs and Co_3O_4 have been loaded on ZnO NWs arrays substrate by finely controlling the concentration of CNTs aqueous solutions as well as the electrodeposition time inside the cobalt precursor electrolyte. Detailed studied of the hierarchical CNTs-ZnO- Co_3O_4 composites

were performed to investigate the activity of PEC water oxidation as photoanodes.

4.2 Experimental methods

4.2.1 Photoanodes preparation

(I) Fabrication of ZnO NWs. ZnO NWs were prepared by a facile hydrothermal synthesis process by referring to the previous report.¹⁰ Briefly, 100 mL of a 0.06 M solution of zinc acetate in absolute ethanol was prepared with ultrasonic agitation as seeds solution. The seeds solution was spin-coated on the pre-treated FTO substrates, and then annealed at 350 °C for 30 min to yield a layer of ZnO seeds. The seeded substrates were suspended vertically in a Teflon vessel, and then sealed in an autoclave and heated to 110 °C for 24 h for nanowire growth. The concentration of the reagent solution varies from 0.04 M to 0.07 M zinc nitrate and hexamethylenetetramine (HMT) aqueous solution to optimize the preparation condition. Finally, the nanowire substrate was removed from the autoclave, washed thoroughly with distilled water, dried in air and annealed at 300 °C for 3h in air.

(II) Fabrication of CNTs-ZnO NWs. The binary CNTs-ZnO Nws were obtained by soaking the as-prepared ZnO NWs in CNTs aqueous solution (concentration of 0.25 mg mL⁻¹, 0.50 mg mL⁻¹ and 1.00 mg mL⁻¹). CNTs powders (Multi-walled, 40~70 nm, Wako) were treated with 3:1 H₂SO₄/HNO₃ mixture for functionalization and better dispersion in water before use.²³ The ZnO/FTO substrates were immersed in the CNTs aqueous solution for 30s, dried in air and annealed at 300 °C for 3h in air.

(III) Fabrication of CNTs-ZnO-Co₃O₄ NWs. The as-obtained CNTs-ZnO/FTO substrates were subsequently used as the working electrode and placed in an electrochemical cell which was assembled in a three-electrode configuration, by using platinum as the counter electrode and Ag/AgCl as the reference electrode. The electrodeposition of cobalt precursors were carried out by galvanostatic deposition at a current density of 1 mA cm⁻² in 0.15 M Co(NO₃)₂ aqueous solution. Finally, the resulting nanowire arrays were withdrawn, rinsed with distilled water and annealed at 300 °C for 3h in air. Fig. 4.1 shows the schematic model of the synthesis process. Co₃O₄-ZnO NWs were synthesized as the same way without decorating the CNTs.

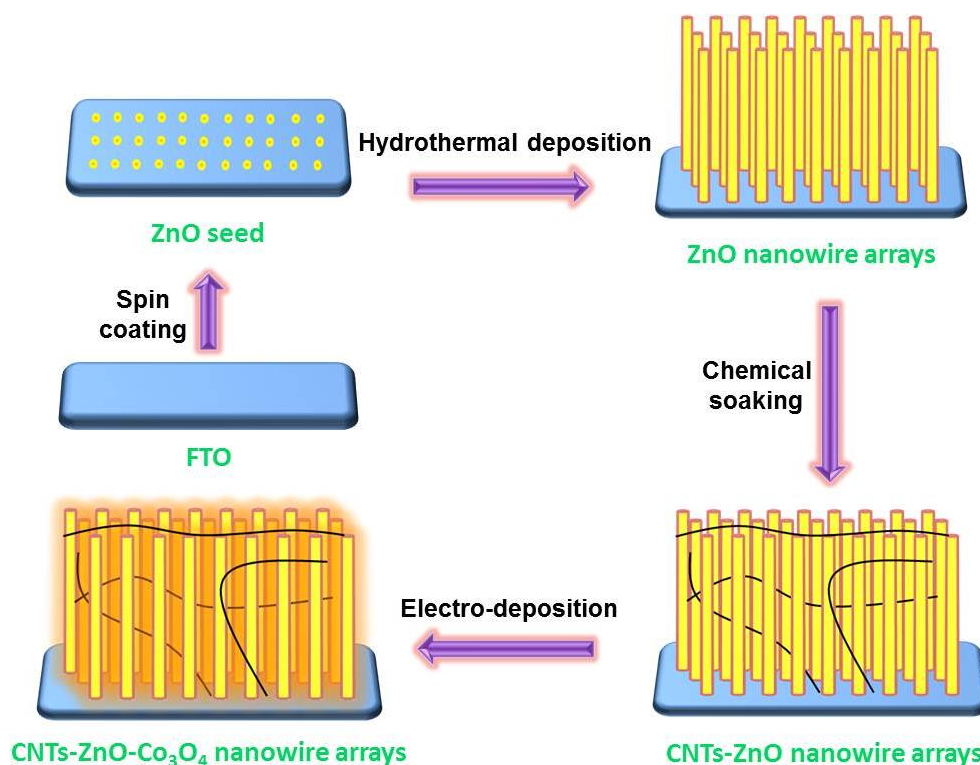


Fig. 4.1 Schematic illustration of the synthesis route of the hierarchical CNTs and Co₃O₄ decorated ZnO NWs arrays.

4.2.2 Sample characterization

The crystal structure of ZnO NWs was determined with an X-ray diffractometer (X'Pert Powder, PANalytical B.V., Netherlands) with Cu-K α radiation. Scanning electron microscopy images were recorded with a HITACHI S-4800 field emission scanning electron microscopy. Transmission electron microscopy images were recorded with a field emission transmission electron microscope (2100F, JEOL Co., Japan) operated at 200 kV, combined with energy dispersive X-ray spectroscopy (EDX) for the determination of metal composition. The diffuse reflection spectra were measured with an integrating sphere equipped UV-visible recording spectrophotometer (UV-2600, Shimadzu Co., Japan) using BaSO₄ as reference and the optical absorptions were converted from the reflection spectra according to Kubelka-Munk equation. Photoelectron Spectroscopy (XPS) experiments were performed in type Theta probe (Thermo Fisher Co., USA) using monochromatized Al K α at $h\nu = 1486.6$ eV and the peak positions were internally referenced to the C 1s peak at 284.6 eV.

4.2.3 Photoelectrochemical measurements

PEC activity measurements were performed with a CHI electrochemical analyser (ALS/CH model 650A) using a standard three-electrode mode with 0.5 M Na₂SO₄ (pH 6.8) solution as the electrolyte using Ag/AgCl (saturated KCl) as the reference electrode and a Pt sheet as the counter electrode. The pristine ZnO NWs, binary CNTs-ZnO NWs, Co₃O₄-ZnO NWs and the ternary CNTs-ZnO-Co₃O₄ NWs arrays were fabricated respectively as photoanode. The simulated sunlight was obtained by an AM 1.5 solar simulator (WXS-80C-3 AM 1.5G) with a light intensity of 100 mW cm⁻². Linear sweep voltammetry (LSV)

was performed with a voltage scan speed of 10 mV s^{-1} and the light was chopped manually at regular intervals. The incident photon to electron conversion efficiency (IPCE) was calculated from chronoamperometry measurements using a motorized monochromator (M10; Jasco Corp.). Electrochemical impedance spectroscopy (EIS) was performed at similar conditions as described above for photoelectrochemical tests. The amplitude of the sinusoidal wave was 5 mV and the frequency range examined was 100 kHz to 1 Hz.

4.3 Results and discussions

4.3.1 Characteristics of ZnO-based NWs composite

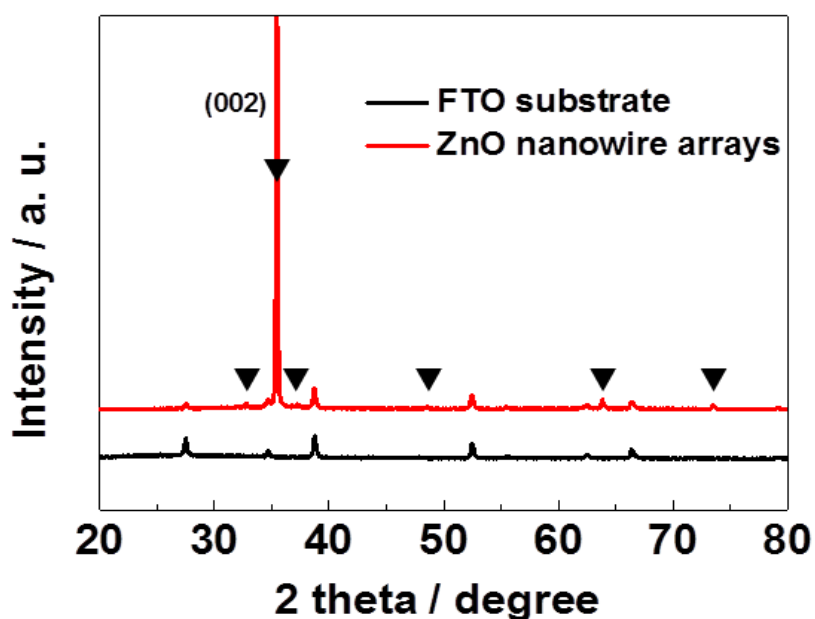


Fig. 4.2 XRD pattern of ZnO NWs arrays (marked by ▼)

The crystal structures were examined by X-ray diffraction (XRD) as Fig. 4.2 shows the XRD patterns of FTO substrate and ZnO/FTO, respectively. The main

peak at 2θ value of 35.1° can be indexed to (002) crystal phase, which confirms the preferential anisotropic growth along the [001] direction of FTO. The microstructures of the prepared ZnO NWs were examined by scanning electron microscope (SEM) and transmission electron microscopy (TEM) as shown in Fig. 4.3. The length of the ZnO NWs are about $2\ \mu\text{m}$ as cross section view shown in the inset of Fig. 4.3b and are vertically aligned on the FTO substrate with an average diameter of $\sim 90\ \text{nm}$. This anisotropic growth is further identified by HRTEM image in the inset of Fig. 4.3a. The microscopic morphologies of ZnO NWs prepared in different hydrothermal synthesis conditions are shown in Fig. 4.4. With the concentration increase, the ZnO NWs grow more densely.

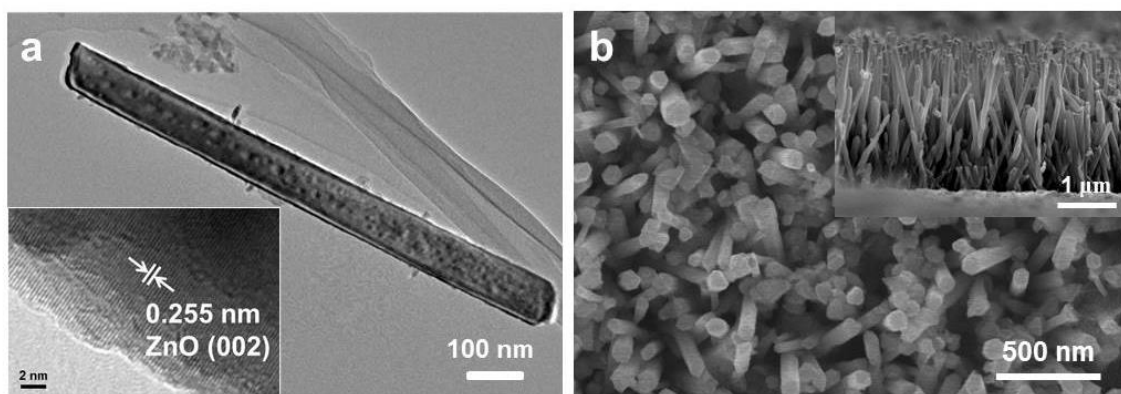


Fig. 4.3 a) TEM image (inset: HRTEM image), b) SEM image (inset: cross section) of ZnO NWs arrays.

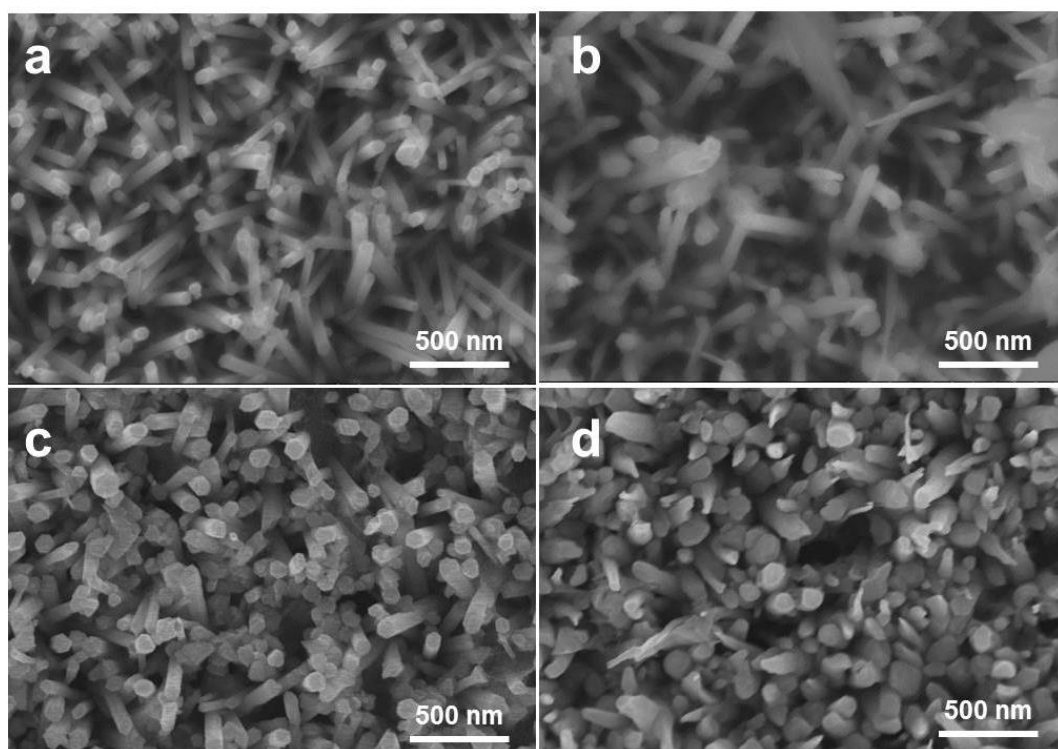


Fig. 4.4 SEM images of ZnO NWs prepared in different hydrothermal synthesis conditions: a) 0.04 M, b) 0.05 M, c) 0.06 M and d) 0.07 M zinc nitrate and hexamethylenetetramine (HMT).

Different concentrations of CNTs aqueous solution were adopted to integrate with ZnO NWs in order to optimize the amount of CNTs. The SEM images (Fig. 4.5) finely confirm that ZnO NWs and CNTs interlaced with one another. CNTs cross through the ZnO NWs arrays and the CNTs loading amount increase obviously with increasing the concentration.

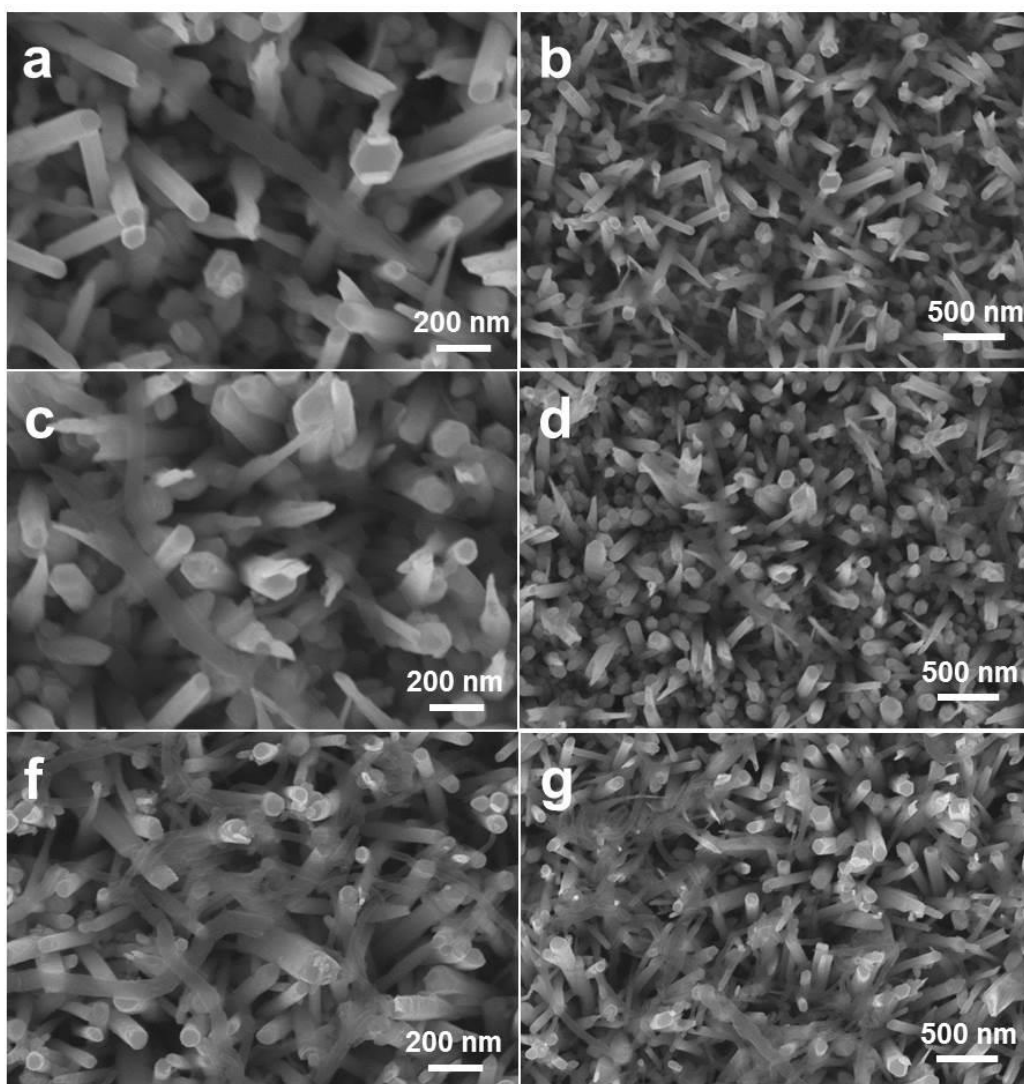


Fig. 4.5 SEM images of CNTs-ZnO NWs prepared in different concentrations of CNTs aqueous solution: a), b) 0.25 mg mL⁻¹; c), d) 0.50 mg mL⁻¹; f), g) 1.00 mg mL⁻¹.

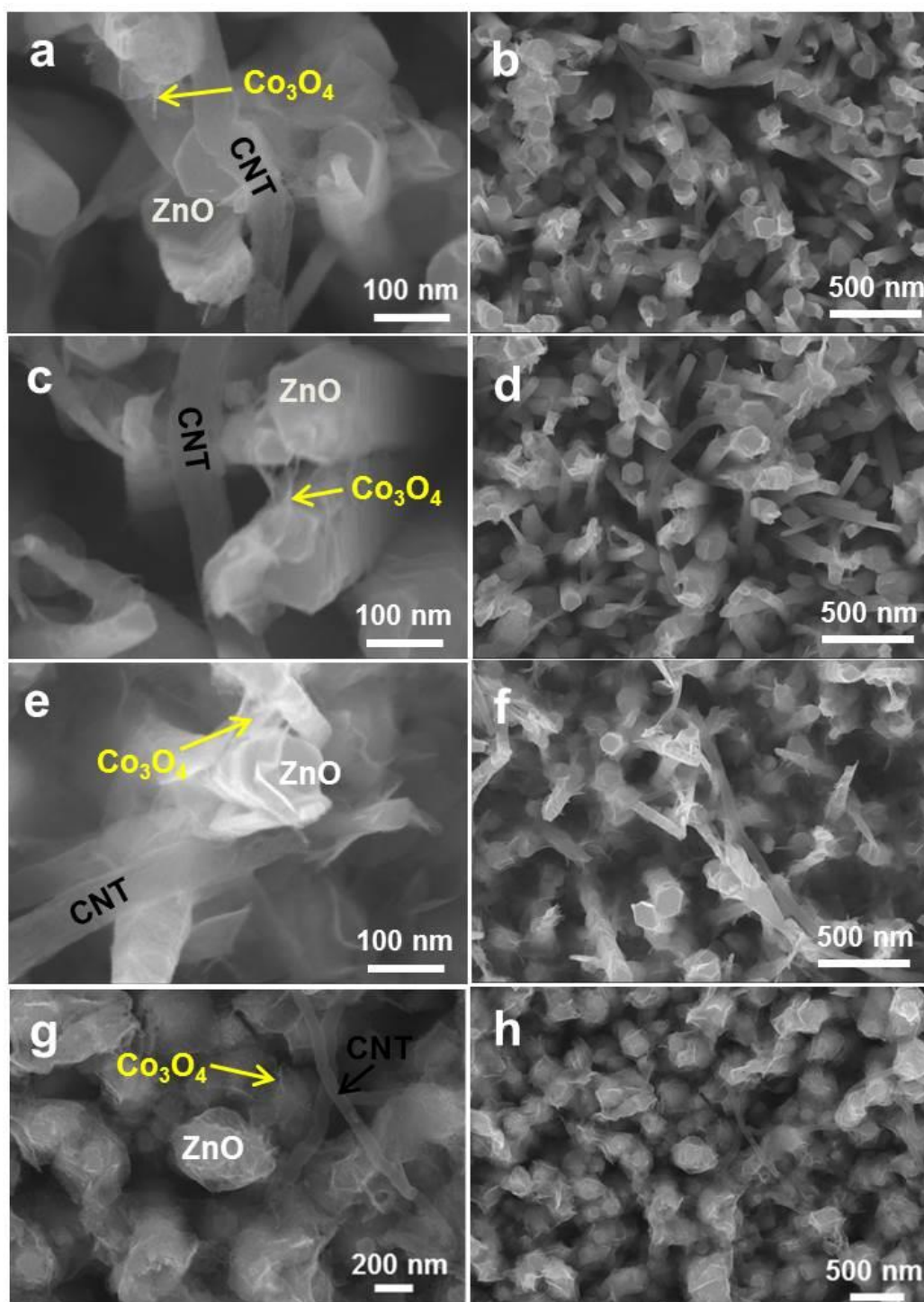


Fig. 4.6 SEM images of the ternary CNTs and Co_3O_4 decorated ZnO NWs arrays with various electrodeposition time: a), b) 10s; c), d) 30s; e), f) 50s and g), h) 70s.

Time-dependent experiments were then carried out to study the formation process of Co_3O_4 on the hierarchical NWs arrays. Fig. 4.6 exhibits the SEM images of the ternary CNTs and Co_3O_4 decorated ZnO NWs arrays with different electrosynthesis time. When the deposition time is 10s, only a small amount of nanoflake Co_3O_4 subunits were loaded on the surface of ZnO NWs. As the electrodeposition time was prolonged gradually, the Co_3O_4 nanoflakes grow bigger and more densely. After the electrosynthesis duration is extended to 70s, the ZnO NWs are fully wrapped with the Co_3O_4 nanoflakes. In particular, the nanostructure has changed to core-shell nanoarrays.

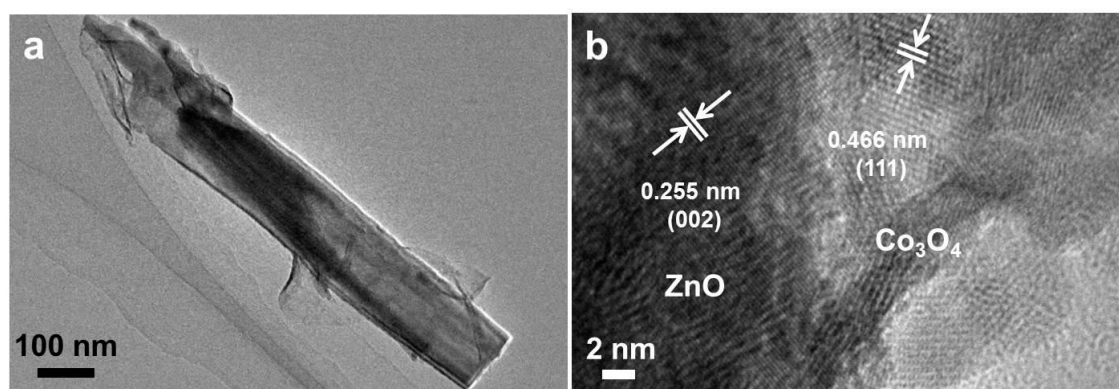


Fig. 4.7 a) TEM image, b) HRTEM image of the CNTs and Co_3O_4 decorated ZnO NWs.

The detailed microscopic morphology and nanostructure information of the ternary CNTs-ZnO- Co_3O_4 NWs arrays were further investigated by TEM and HRTEM, as shown in Fig. 4.7. The TEM image shows the specific nanoflake-like Co_3O_4 decorated ZnO NWs morphology (Fig. 4.7a), which is in accordance well with the SEM results. ZnO NWs and Co_3O_4 nanoflakes can be clearly distinguished in the HRTEM image (Fig. 4.7b), and it also indicate a finely contacted interface. The corresponding EDX mapping analysis (Fig. 4.8)

confirms that zinc is located in the central part of the NWs while cobalt is homogeneously distributed around the NWs.

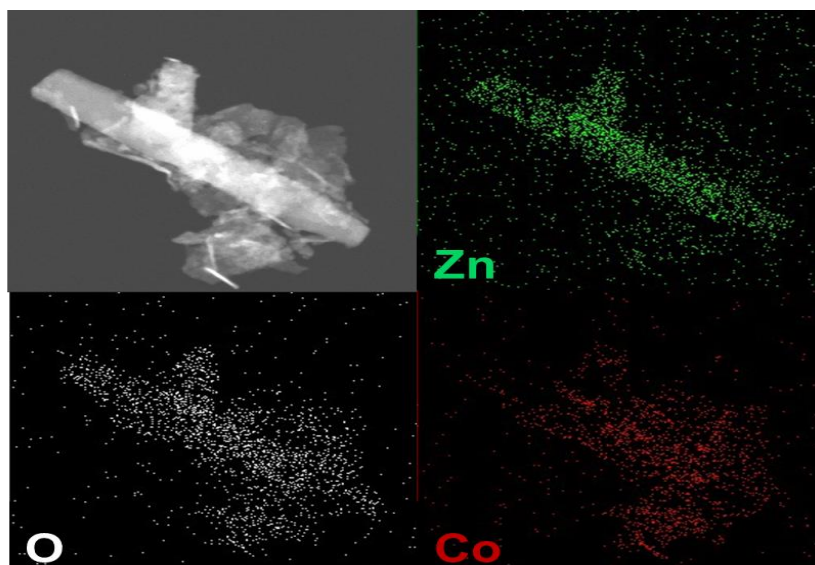


Fig. 4.8 EDX mapping of the CNTs and Co_3O_4 decorated ZnO NWs.

In order to confirm the phase state of the cobalt oxide, the ternary NWs arrays sample is characterized by XPS analysts as shown in Fig. 4.9. The Co 2p XPS spectra show two major peaks with binding energy values at 795.1 and 780.1 eV, corresponding to the Co 2p_{1/2} and Co 2p_{3/2} spin-orbit peaks of the Co_3O_4 phase, respectively. The Co 2p peaks can be decomposed to Co^{3+} and Co^{2+} oxidation state, with Co^{3+} presenting a more dominant state. The weak satellite structure is ascribed to a shake-up related to the Co^{2+} component of the structure.²⁴ It is clearly detected in the spectrum that a satellite peak at 790.3 eV is about 9 eV higher than the position of the main peak of Co 2p_{3/2}. This is associated with the typical assignment of cobalt oxidation states in Co_3O_4 .²⁵ Thus, it can be deduced that the electrodeposited cobalt precursors have successfully been converted to Co_3O_4 after annealing in air.

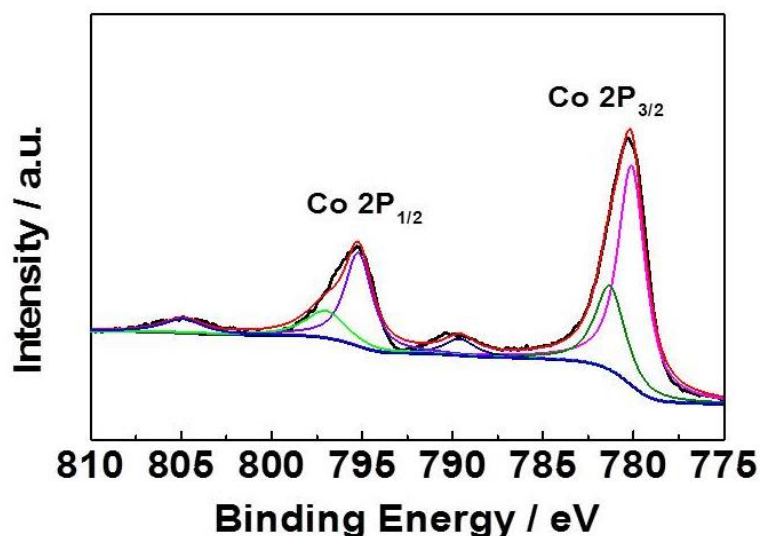


Fig. 4.9 XPS spectra of Co 2p for the CNTs and Co₃O₄ decorated ZnO NWs.

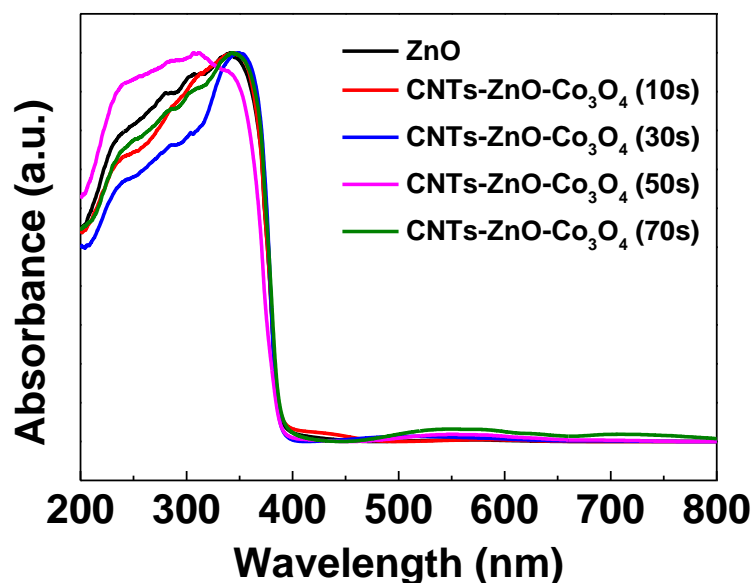


Fig. 4.10 UV-vis absorption spectra of CNTs-ZnO-Co₃O₄ NWs arrays with various Co precursor electrodeposition durations.

UV-vis absorption spectra of the ternary CNTs and Co₃O₄ decorated ZnO NWs arrays with various electrodeposition durations are shown in Fig. 4.10. The spectra exhibit similar absorption properties with intense absorption edges. With the deposition time increasing, some absorption peaks appear in the visible light region due to the visible light response of Co₃O₄. The binary Co₃O₄ decorated

ZnO NWs arrays were also synthesized as contrast samples. The morphology exhibits the same growth tendency as the ternary NWs arrays. With increasing the deposition time of the cobalt precursor, Co_3O_4 nanoflakes grow more densely as show in Fig. 4.11.

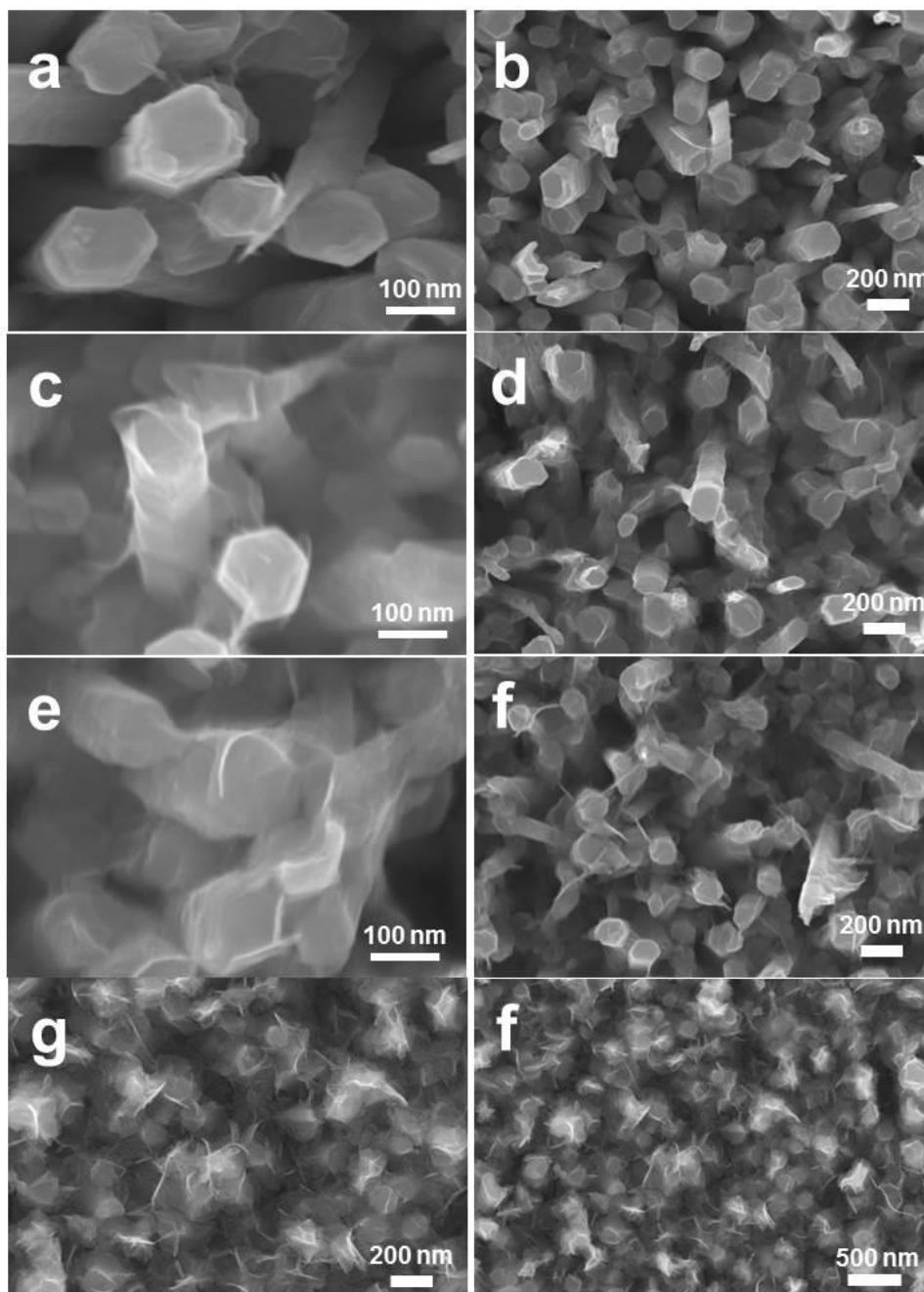


Fig. 4.11 SEM images of binary Co_3O_4 -ZnO NWs arrays with various electrodeposition time: a), b) 10s; c), d) 30s; e), f) 50s and g), h) 70s.

4.3.2 PEC performance of pristine ZnO NWs, binary CNTs-ZnO NWs, Co₃O₄-ZnO NWs photoanodes

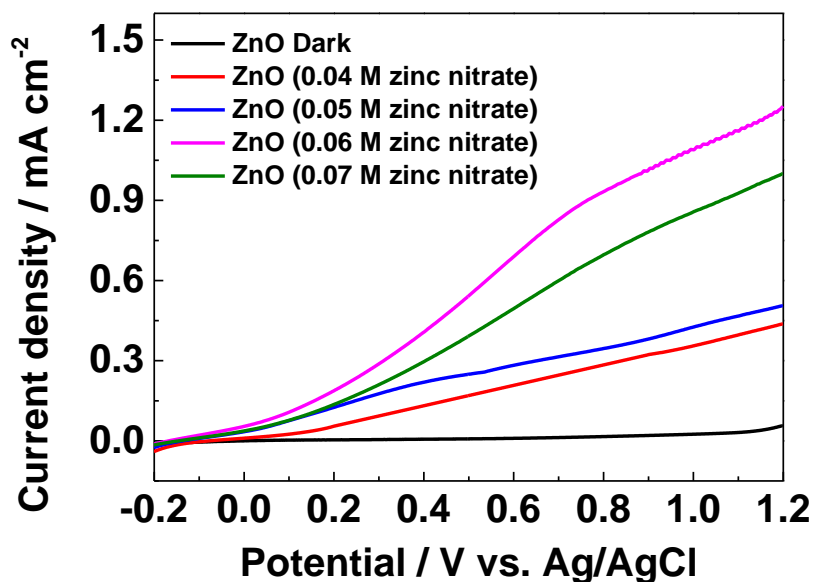


Fig. 4.12 Current-voltage curves of pristine ZnO NWs prepared in different hydrothermal synthesis conditions.

The photoelectrocatalytic performance of the pristine ZnO NWs, binary CNTs-ZnO NWs and Co₃O₄-ZnO NWs arrays as photoanodes were investigated in PEC water oxidation under AM 1.5G light. All the current-voltage results were recorded in a 0.5 M Na₂SO₄ (pH 6.8) aqueous solution with the potential region from -0.2 V to 1.2 V vs. Ag/AgCl at a scan rate of 10 mV s⁻¹. The pristine ZnO NWs were synthesized in various concentrations of zinc nitrite solutions during the hydrothermal process to optimize the preparation conditions of ZnO NWs. The corresponding photocurrent densities are shown in Fig. 4.12. The best PEC performance is observed at the ZnO NWs prepared in 0.06 M zinc nitrite aqueous solution, where the current density exceeded 0.7 mA cm⁻² at 0.6 V (approximate to 1.23 V vs. RHE). It is mainly attributed to a better growth of crystal and space

alignment in this 0.06 M zinc nitrite solution. Thus, the ZnO NWs used in the following study are all synthesized in this condition.

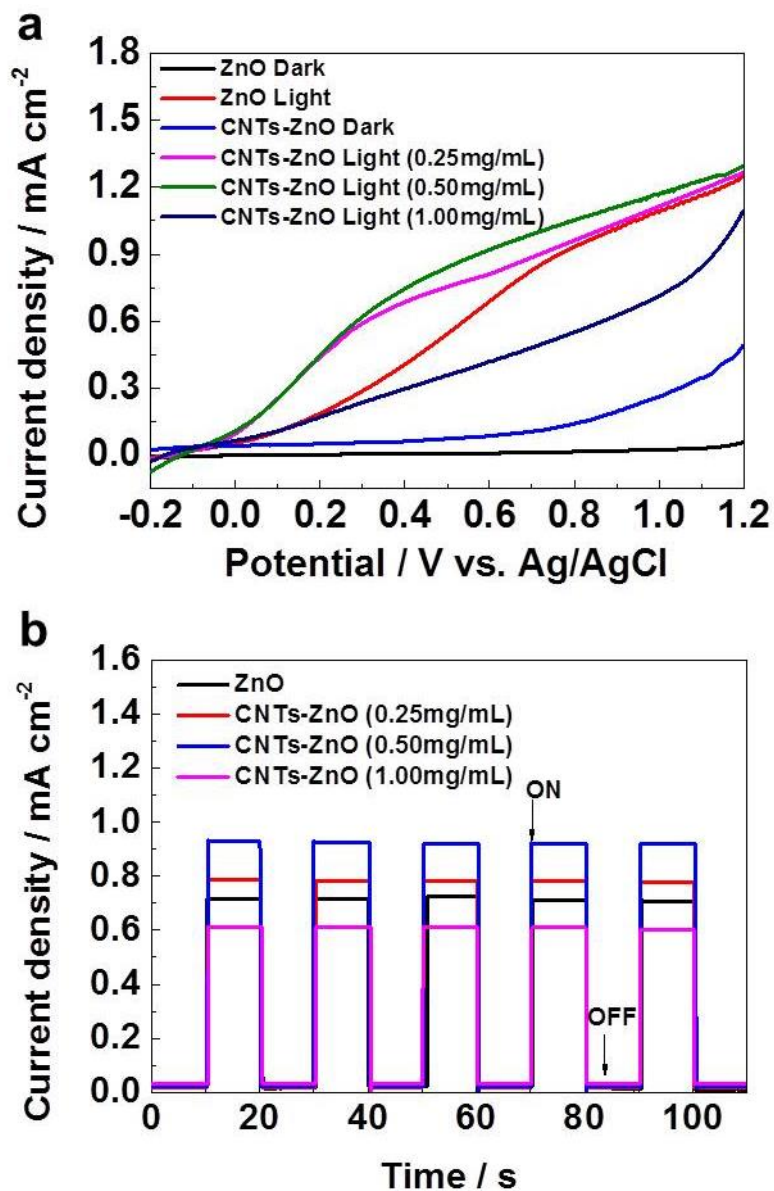


Fig. 4.13 a) Current-voltage curves and b) amperometric I-t curves measured at 0.6 V of CNTs-ZnO NWs prepared in different concentrations of CNTs aqueous solution.

The PEC performances of the binary CNTs-ZnO NWs synthesized in different concentration of CNTs aqueous solutions are shown in Fig. 4.13. The samples prepared in 0.25 mg mL^{-1} and 0.50 mg mL^{-1} CNTs aqueous solutions show obvious enhancement of the photocurrent densities, especially in the potential region of 0.0 V to 0.6 V. It can be deduced that the CNTs interlaced with the ZnO NWs increase the total conductivity of the binary CNTs-ZnO NWs arrays. However, with the concentration of CNTs aqueous solution increased to 1.00 mg mL^{-1} , the photocurrent density decreases dramatically. It is mainly because that too many CNTs loaded on ZnO NWs block the light as shown in Figure S2G and S2F. As the sample prepared in 0.50 mg mL^{-1} CNTs aqueous solution exhibited the best PEC performance, this 0.50 mg mL^{-1} CNTs aqueous solution was adapted for the following synthesis of the ternary CNTs and Co_3O_4 decorated ZnO NWs arrays. The binary Co_3O_4 decorated ZnO NWs arrays were also synthesized as contrast samples. The morphology exhibits the same growth tendency as the ternary NWs arrays. With increasing the deposition time of the cobalt precursor, Co_3O_4 nanoflakes grow more densely as show in Fig. 4.11. The corresponding PEC performances are shown in Fig. 4.14. The photocurrent densities show a pronounced enhancement compared with the pristine ZnO NWs. Co_3O_4 -ZnO (30s) exhibits the best activity, where the current density increases to ca. 1.3 mA cm^{-2} at 0.6 V under illumination.

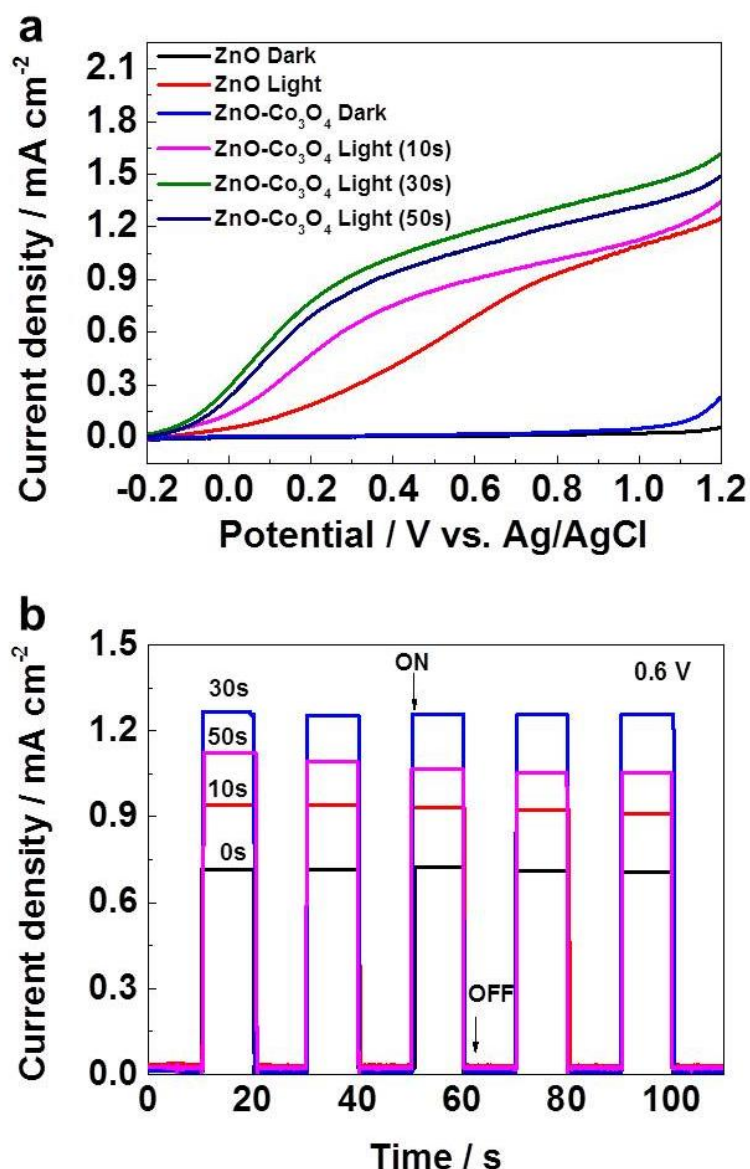


Fig. 4.14 a) Current-voltage curves and b) amperometric I-t curves measured at 0.6 V of Co₃O₄-ZnO NWs prepared in various electrodeposition time.

4.3.3 PEC performance of ternary CNTs-ZnO-Co₃O₄ NWs composite photoanode

The hierarchical CNTs-ZnO-Co₃O₄ nanoarrays were subsequently investigated as photoanodes, which exhibit promising photoelectrocatalytic activities for PEC water oxidation reaction. Fig. 4.15 shows the comparison with the pristine ZnO NWs, binary CNTs-ZnO NWs and Co₃O₄-ZnO NWs. Both of

the dark and light current densities enhanced remarkably and the photocurrent density of CNTs-ZnO-Co₃O₄ nanoarrays increased significantly in the potential region from -0.2 V to 1.2 V vs. Ag/AgCl. The photoelectric response of CNTs-ZnO-Co₃O₄ nanoarrays photoanode starts at a more negative onset potential, and the photocurrent density roaringly increases to 1.9 mA cm⁻² at 0.6 V under illumination. It is about 2.7 times larger than that of pristine ZnO NWs as well as 1.9 times and 1.5 times larger than the binary CNTs-ZnO NWs and Co₃O₄-ZnO NWs at 0.6 V, respectively. These results indicate that the PEC performance for water oxidation was definitely enhanced by decorating the ZnO NWs with CNTs and Co₃O₄ to form the hierarchical nanostructure. Additionally, the cathodic shift of the onset potential suggests that a decreased charge recombination and a reduced overpotential in the ternary photoanode.^{11, 26}

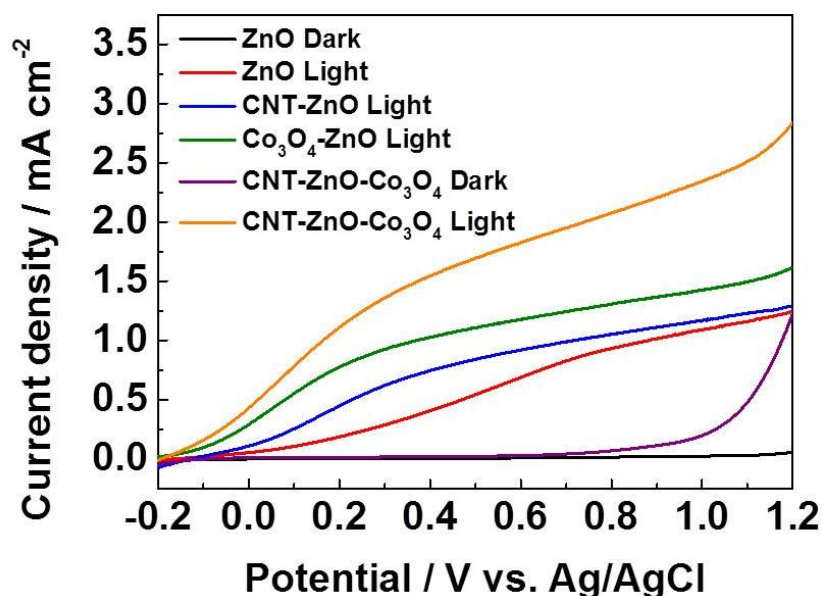


Fig. 4.15 Current-voltage curves of pristine ZnO NWs, binary CNTs-ZnO (0.50 mg mL⁻¹) NWs, Co₃O₄-ZnO (30 s) NWs and ternary CNTs-ZnO-Co₃O₄ (30 s) NWs.

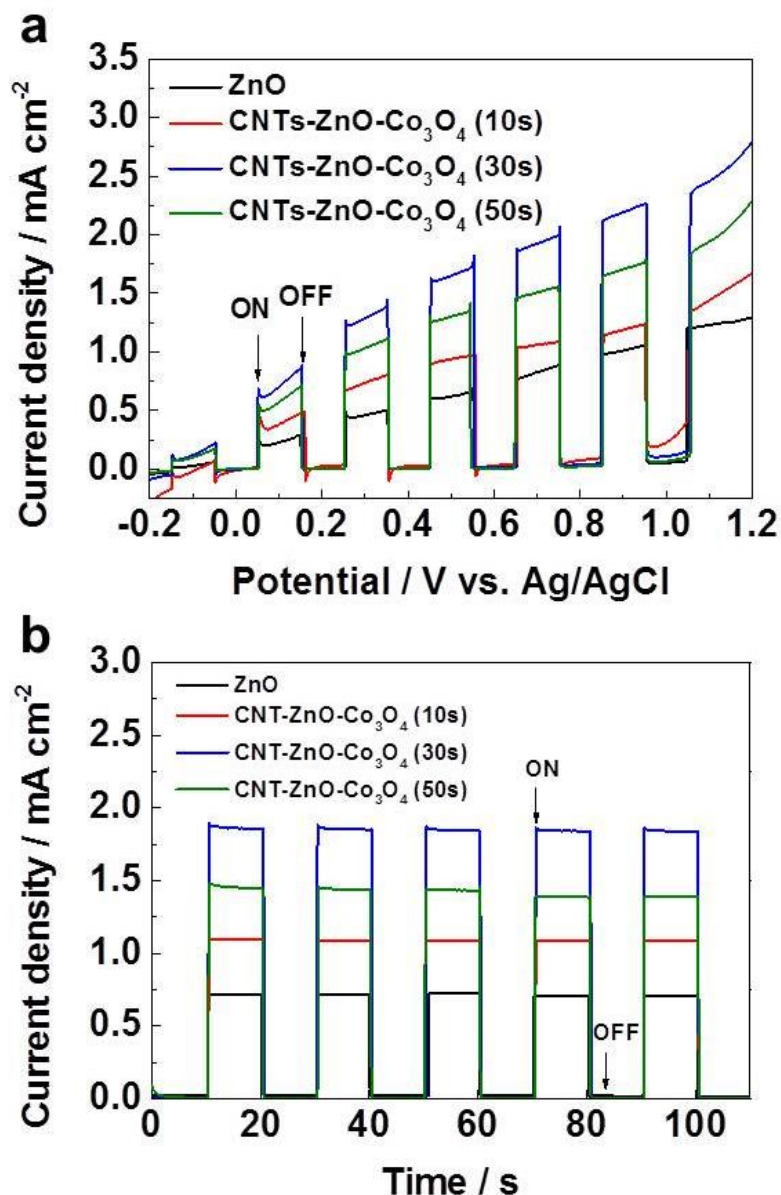


Fig. 4.16 a) current-voltage curves of pristine ZnO NWs and ternary CNTs-ZnO-Co₃O₄ NWs under chopped light illumination; b) amperometric I-t curves of pristine ZnO NWs and ternary CNTs-ZnO-Co₃O₄ NWs measured at 0.6V vs. Ag/AgCl.

In order to further investigate the effect of the Co₃O₄ decorated on the CNTs-ZnO NWs, the photocurrent densities of the ternary composites with various cobalt precursor deposition time were carried out during repeated ON-OFF illumination cycles. As shown in Fig. 4.16a, a steady and prompt

photoresponse can be observed. The measured photocurrents are greatly affected by the loading amount of Co_3O_4 . The ternary nanoarrays photoanode reaches the maximum activity when the cobalt precursor deposition time is 30s. With the deposition time exceeding this proper level, the photocurrent decreases significantly. A dense wrapping up of the Co_3O_4 nanoflakes seems to have hindered the light absorption. Moreover, densely loaded Co_3O_4 resulted in more contact of Co_3O_4 with CNTs, increases the recombination between the electrons in CNTs and the holes in Co_3O_4 , so that the charge transfer efficiency within the composite has been decreased obviously. Thus, the loading of Co_3O_4 should be controlled in an optimal amount, not only to fully realize its ability as cocatalysts for water oxidation but also to avoid its contact with CNTs as well as the corresponding charge recombination. The transient photocurrents of the samples were examined during the light ON-OFF cycling at 0.6 V as shown in Fig. 4.16b. All of the samples exhibit prompt and reproducible photocurrent responses upon each illumination. It further confirms that the photogenerated charges have promptly transferred from ZnO NWs to the loaded CNTs and Co_3O_4 . Thus, this ternary hierarchical nanostructure effectively enhances the optical pathway and assists the charge separation. When comparing our photocurrent density as photoanode with the commonly reported ZnO,^{11, 27-29} TiO_2 ,³⁰⁻³³ Fe_2O_3 ,³⁴⁻³⁶ WO_3 ,^{37, 38} based photoelectrodes in the literatures (usually around 1 mA cm^{-2} at $\sim 1.2 \text{ V}$ vs. RHE), the results in this work exhibits superior PEC activity. This can be attributed to the facilitated charge transfer and increased water oxidation reaction rates by forming the ternary CNTs and Co_3O_4 decorated ZnO NWs arrays composites nanostructure.

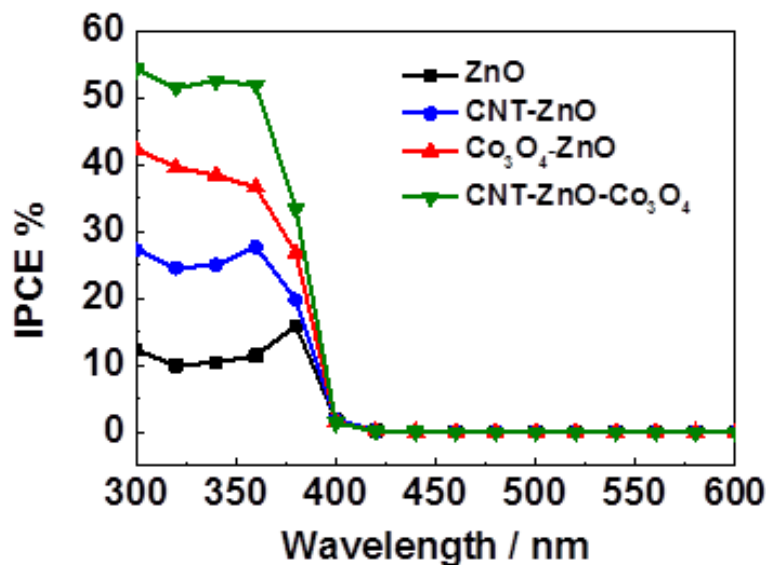


Fig. 4.17 IPCE spectra of pristine ZnO NWs, binary CNTs-ZnO NWs, Co₃O₄-ZnO NWs and ternary CNTs-ZnO-Co₃O₄ NWs at 0.6 V vs. Ag/AgCl.

Incident photon to current conversion efficiency (IPCE) was evaluated at 0.6 V vs. Ag/AgCl for the pristine ZnO NWs, binary CNTs-ZnO NWs, Co₃O₄-ZnO NWs and the ternary CNTs-ZnO-Co₃O₄ NWs arrays, in order to understand the interplay between the photoactivity and light absorption as shown in Fig. 4.17. IPCE can be expressed as $IPCE = 1240 j_p(\lambda) / \lambda E_\lambda(\lambda)$, where $j_p(\lambda)$ is the measured photocurrent density (mA cm^{-2}), λ is the incident light wavelength (nm) and $E_\lambda(\lambda)$ is the incident monochromatic light power density (mW cm^{-2}) at a specific wavelength. The photocurrent responses of the binary and ternary NWs arrays exhibit almost the same feature as the absorption spectrum of pristine ZnO NWs, suggesting that the observed photocurrent is mainly based on the band gap transition of ZnO. The ternary CNTs-ZnO-Co₃O₄ NWs arrays exhibit significant enhancement of photoactivity. It shows the highest IPCE value of 52.5% at 340 nm, which is 5.1 times higher than that of the pristine ZnO NWs as well as 2.1

times and 1.4 times higher than the binary CNTs-ZnO NWs and Co_3O_4 -ZnO NWs, respectively.

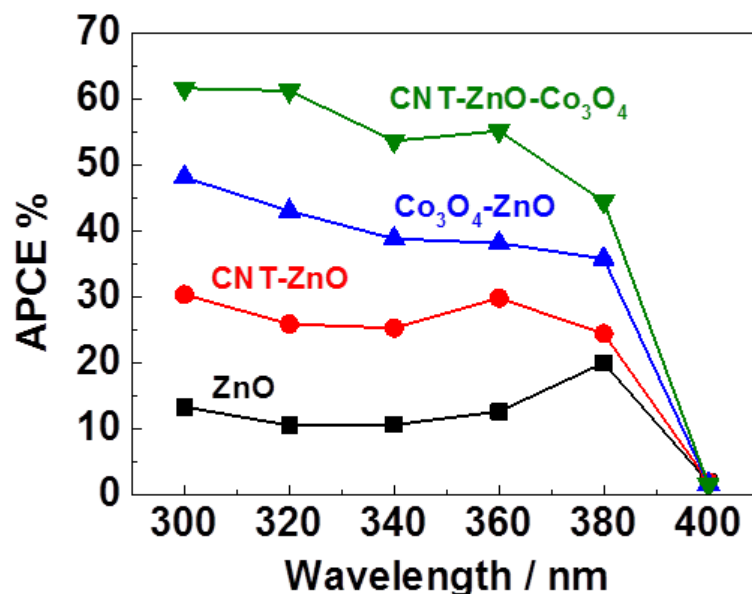


Fig. 4.18 APCE spectra (derived from the IPCE and LHE) of pristine ZnO NWs, binary CNTs-ZnO NWs, Co_3O_4 -ZnO NWs and ternary CNTs-ZnO- Co_3O_4 NWs at 0.6 V vs. Ag/AgCl.

Absorbed-photon-to-current conversion efficiency (APCE) was further calculated by considering the absorbance (A_λ) of the material at the particular wavelength as shown in Fig. 4.18 using the following equation: $\text{APCE} = \text{IPCE} / (1 - 10^{-A_\lambda})$, where A_λ is the absorbance, $(1 - 10^{-A_\lambda})$ represents the light harvesting efficiency (LHE) of the film. APCE values only response in the absorption range of ZnO (before 400 nm) and it exhibits similar tendency to the IPCE values of the ZnO-based photoanodes. The APCE results further confirmed that ZnO serves as the photo-response component within the composite materials. The ternary composite CNT-ZnO- Co_3O_4 demonstrates an APCE value of 59.7% at 340 nm, which is ca. 5.1 times higher than that of the pristine ZnO NWs. The binary

composites of CNT-ZnO and Co₃O₄-ZnO also exhibit enhancements of APCE, which is ca. 2.4 and 3.7 times higher than the pristine ZnO NWs, respectively. These results suggest that the enhancement of photactivity is mainly due to an increase in electron-hole separation, rather than the increase in photon absorption by loading CNT and Co₃O₄ on ZnO NWs.

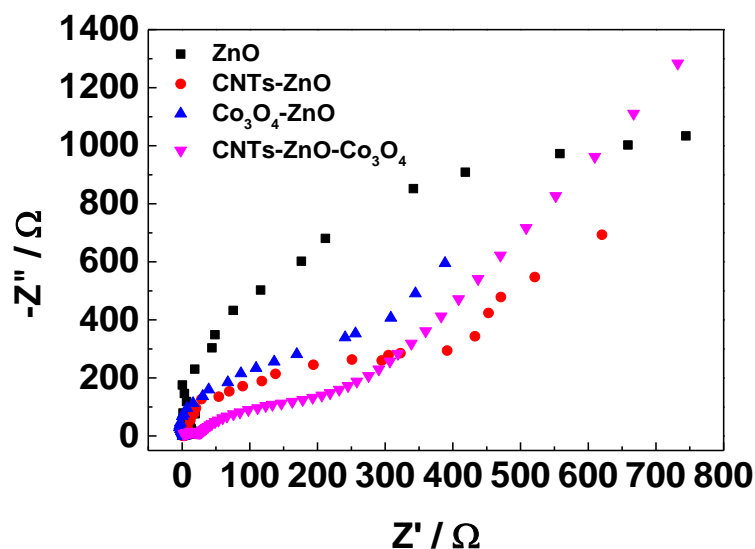


Fig. 4.19 EIS plots of the pristine ZnO NWs, binary CNTs-ZnO NWs, Co₃O₄-ZnO NWs and the ternary CNTs-ZnO-Co₃O₄ NWs arrays.

Electrochemical impedance spectroscopy (EIS) was carried out to further confirm the advantage of the ternary CNTs-ZnO-Co₃O₄ NWs in improving the charge transfer as shown in Fig. 4.19. A smaller size of the semicircle arc diameters indicates a more effective separation of the photogenerated electron-hole pair and a faster interfacial charge transfer to the electron donor acceptor.^{39, 40} The charge separation and transfer abilities are in the order of CNTs-ZnO-Co₃O₄ NWs > CNTs-ZnO NWs > Co₃O₄-ZnO NWs > ZnO NWs. Both of the decorated CNTs and Co₃O₄ have exhibited effective ability in improving the charge transfer. Although using oxygen-containing groups to

functionalize CNTs would reduce the length and conductivity of CNTs,^{41, 42} the charge transfer resistance has been effectively reduced by loading CNTs on ZnO NWs.

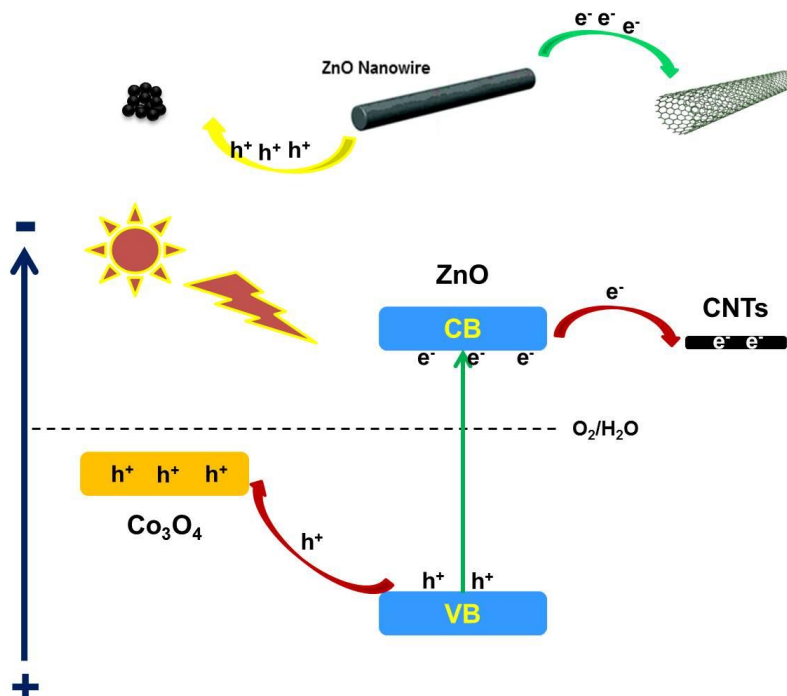


Fig. 4.20 Schematic illustration of the charge transfer pathway in ternary CNTs-ZnO-Co₃O₄ NWs arrays under illumination.

Fig. 4.20 illustrates a supposed schematic model of the charge transfer pathway in the ternary CNTs-ZnO-Co₃O₄ NWs arrays under illumination. CNTs facilitate the charge separation and transfer by increasing the conductivity of the nanoarrays in a macroscopic aspect. In a microscopic point of view, since not each ZnO nanowire possess the same conductivity, only the high-conductivity nanowire could timely transfer the photogenerated electron to the FTO substrate before recombination. After interlacing the ZnO NWs with CNTs, CNTs bridge the low-conductivity nanowire, high-conductivity nanowire and FTO substrate together. Thus, the electron generated in the low-conductivity nanowire could

also be timely transferred to the FTO substrate through CNTs and high-conductivity nanowire mediately under bias. On the other hand, Co_3O_4 , as an effective water oxidation cocatalyst,^{16, 17, 43} could further promote the charge separation and transfer from ZnO to Co_3O_4 . Thus the recombination of photogenerated hole-electron pairs has been decreased. Moreover, the chemical stability of CNTs-ZnO- Co_3O_4 NWs has also been improved due to the promoted holes transfer from ZnO to Co_3O_4 , which can prevent ZnO from photo-corrosion. As shown in Fig. 4.21, the photocurrent response is almost identical over 30 cycles. In addition, Co_3O_4 is also an effective material in decreasing water oxidation overpotential and increasing reaction rates of water oxidation. It is usually associated with the mechanism involving the electrochemical steps of $\text{Co(II)} \rightarrow \text{Co(III)}$ and $\text{Co(III)} \rightarrow \text{Co(IV)}$.^{43, 44} Therefore, accounting for the synergistic cooperation of CNTs and Co_3O_4 in charge separation, the hierarchical construction of ternary CNTs-ZnO- Co_3O_4 NWs arrays composites demonstrates an efficient way in water oxidation as a photoanode.

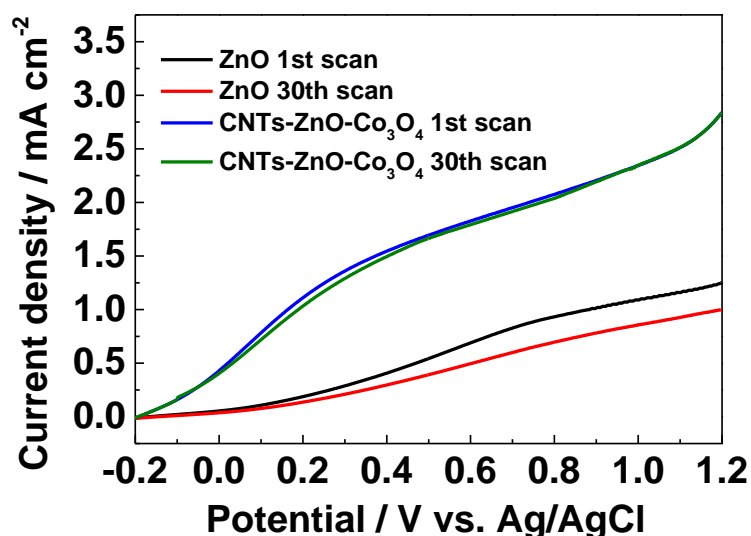


Fig. 4.21 Stability tests for PEC performance of ZnO NWs and CNTs-ZnO- Co_3O_4 NWs after 30 scans.

4.4 Conclusions

In summary, hierarchically CNTs and Co_3O_4 decorated ZnO nanowire arrays with ternary heteroassembly nanostructures have been successfully fabricated via a facile stepwise synthesis process. Detailly, CNTs were interlaced with ZnO NWs to improve the conductivity and Co_3O_4 was loaded on ZnO as water oxidation cocatalysts. ZnO NWs serves as the main photosensitizer while CNTs could act as a cocatalyst to further promote the separation and transfer of photogenerated electrons, meanwhile Co_3O_4 could synergistically transfer the holes from ZnO. Therefore, the ternary CNTs-ZnO- Co_3O_4 NWs arrays exhibit significantly enhanced activity in PEC water oxidation compared with the pristine ZnO NWs, binary CNTs-ZnO NWs and Co_3O_4 -ZnO NWs as photoanodes under AM 1.5G simulated sunlight. This can be attributed to the effectively improved photogenerated charge separation and transfer as well as the markedly accelerated water oxidation reaction rates due to the specific ternary architecture.

References

1. B. Kumar, M. Llorente, J. Froehlich, T. Dang, A. Sathrum and C. P. Kubiak, *Annu. Rev. Phys. Chem.*, 2012, **63**, 541-569.
2. M. Gratzel, *Nature*, 2001, **414**, 338-344.
3. M. G. Walter, E. L. Warren, J. R. McKone, S. W. Boettcher, Q. Mi, E. A. Santori and N. S. Lewis, *Chem. Rev.*, 2010, **110**, 6446-6473.
4. T. Hisatomi, J. Kubota and K. Domen, *Chem. Soc. Rev.*, 2014, **43**, 7520-7535.
5. N. P. Dasgupta, J. Sun, C. Liu, S. Brittman, S. C. Andrews, J. Lim, H. Gao, R. Yan and P. Yang, *Adv. Mater.*, 2014, **26**, 2137-2184.
6. Y. Xia, P. Yang, Y. Sun, Y. Wu, B. Mayers, B. Gates, Y. Yin, F. Kim and H. Yan, *Adv.*

- Mater.*, 2003, **15**, 353-389.
7. Z. L. Wang and J. Song, *Science*, 2006, **312**, 242-246.
8. H. Yu, Z. Zhang, M. Han, X. Hao and F. Zhu, *J. Am. Chem. Soc.*, 2005, **127**, 2378-2379.
9. L. Vayssieres, *Adv. Mater.*, 2003, **15**, 464-466.
10. H. M. Chen, C. K. Chen, Y.-C. Chang, C.-W. Tsai, R.-S. Liu, S.-F. Hu, W.-S. Chang and K.-H. Chen, *Angew. Chem. Int. Ed.*, 2010, **49**, 5966-5969.
11. M. Shao, F. Ning, M. Wei, D. G. Evans and X. Duan, *Adv. Funct. Mater.*, 2014, **24**, 580-586.
12. S. K. Karuturi, J. Luo, C. Cheng, L. Liu, L. T. Su, A. I. Y. Tok and H. J. Fan, *Adv. Mater.*, 2012, **24**, 4157-4162.
13. A. Kudo and Y. Miseki, *Chem. Soc. Rev.*, 2009, **38**, 253-278.
14. J. Yang, D. Wang, H. Han and C. Li, *Acc. Chem. Res.*, 2013, **46**, 1900-1909.
15. Y. Ma, X. Wang, Y. Jia, X. Chen, H. Han and C. Li, *Chem. Rev.*, 2014, **114**, 9987-10043.
16. M. Liao, J. Feng, W. Luo, Z. Wang, J. Zhang, Z. Li, T. Yu and Z. Zou, *Adv. Funct. Mater.*, 2012, **22**, 3066-3074.
17. L. Xi, P. D. Tran, S. Y. Chiam, P. S. Bassi, W. F. Mak, H. K. Mulmudi, S. K. Batabyal, J. Barber, J. S. C. Loo and L. H. Wong, *J. Phys. Chem. C*, 2012, **116**, 13884-13889.
18. T. Y. Ma, S. Dai, M. Jaroniec and S. Z. Qiao, *J. Am. Chem. Soc.*, 2014, **136**, 13925-13931.
19. N. Kang, J. H. Park, M. Jin, N. Park, S. M. Lee, H. J. Kim, J. M. Kim and S. U. Son, *J. Am. Chem. Soc.*, 2013, **135**, 19115-19118.
20. J. Wei, Y. Jia, Q. Shu, Z. Gu, K. Wang, D. Zhuang, G. Zhang, Z. Wang, J. Luo, A. Cao and D. Wu, *Nano Lett.*, 2007, **7**, 2317-2321.

21. Z. Li, V. P. Kunets, V. Saini, Y. Xu, E. Dervishi, G. J. Salamo, A. R. Biris and A. S. Biris, *ACS Nano*, 2009, **3**, 1407-1414.
22. Z. Li, S. A. Kulkarni, P. P. Boix, E. Shi, A. Cao, K. Fu, S. K. Batabyal, J. Zhang, Q. Xiong, L. H. Wong, N. Mathews and S. G. Mhaisalkar, *ACS Nano*, 2014, **8**, 6797-6804.
23. Y.-C. Tsai, S.-C. Li and S.-W. Liao, *Biosens. Bioelectron.*, 2006, **22**, 495-500.
24. N. S. McIntyre, D. D. Johnston, L. L. Coatsworth, R. D. Davidson and J. R. Brown, *Surf. Interface Anal.*, 1990, **15**, 265-272.
25. Y. Wang, Z.-W. Fu and Q.-Z. Qin, *Thin Solid Films*, 2003, **441**, 19-24.
26. Y. Hou, F. Zuo, A. Dagg and P. Feng, *Angew. Chem. Int. Ed.*, 2013, **52**, 1248-1252.
27. K. Pan, Y. Dong, W. Zhou, Q. Pan, Y. Xie, T. Xie, G. Tian and G. Wang, *ACS Appl. Mater. Interfaces*, 2013, **5**, 8314-8320.
28. X. Yang, A. Wolcott, G. Wang, A. Sobo, R. C. Fitzmorris, F. Qian, J. Z. Zhang and Y. Li, *Nano Lett.*, 2009, **9**, 2331-2336.
29. M. Zhong, Y. Li, I. Yamada and J.-J. Delaunay, *Nanoscale*, 2012, **4**, 1509-1514.
30. A. Wolcott, W. A. Smith, T. R. Kuykendall, Y. Zhao and J. Z. Zhang, *Small*, 2009, **5**, 104-111.
31. J. Cao, Y. Zhang, H. Tong, P. Li, T. Kako and J. Ye, *Chem. Commun.*, 2012, **48**, 8649-8651.
32. Q. Kang, J. Cao, Y. Zhang, L. Liu, H. Xu and J. Ye, *J. Mater. Chem. A*, 2013, **1**, 5766-5774.
33. S. Hoang, S. Guo, N. T. Hahn, A. J. Bard and C. B. Mullins, *Nano Lett.*, 2012, **12**, 26-32.
34. D. K. Zhong and D. R. Gamelin, *J. Am. Chem. Soc.*, 2010, **132**, 4202-4207.
35. K. J. McDonald and K.-S. Choi, *Chem. Mat.*, 2011, **23**, 1686-1693.
36. J. Cao, L. Liu, A. Hashimoto and J. Ye, *Electrochem. Commun.*, 2014, **48**, 17-20.

37. D.-D. Qin, C.-L. Tao, S. A. Friesen, T.-H. Wang, O. K. Varghese, N.-Z. Bao, Z.-Y. Yang, T. E. Mallouk and C. A. Grimes, *Chem. Commun.*, 2012, **48**, 729-731.
38. X. Chen, J. Ye, S. Ouyang, T. Kako, Z. Li and Z. Zou, *ACS Nano*, 2011, **5**, 4310-4318.
39. W. H. Leng, Z. Zhang, J. Q. Zhang and C. N. Cao, *J. Phys. Chem. B*, 2005, **109**, 15008-15023.
40. X. F. Cheng, W. H. Leng, D. P. Liu, Y. M. Xu, J. Q. Zhang and C. N. Cao, *J. Phys. Chem. C*, 2008, **112**, 8725-8734.
41. Y. Zhang, J. Li, Y. Shen, M. Wang and J. Li, *J. Phys. Chem. B*, 2004, **108**, 15343-15346.
42. Y. Shen, J. S. Reparaz, M. R. Wagner, A. Hoffmann, C. Thomsen, J.-O. Lee, S. Heeg, B. Hatting, S. Reich, A. Saeki, S. Seki, K. Yoshida, S. S. Babu, H. Mohwald and T. Nakanishi, *Chem. Sci.*, 2011, **2**, 2243-2250.
43. M. Barroso, A. J. Cowan, S. R. Pendlebury, M. Grätzel, D. R. Klug and J. R. Durrant, *J. Am. Chem. Soc.*, 2011, **133**, 14868-14871.
44. J. A. Koza, Z. He, A. S. Miller and J. A. Switzer, *Chem. Mat.*, 2012, **24**, 3567-3573.

Chapter 5 Design of Photoelectrochemical Device for the Selective Conversion of CO₂ to CO Using Mesoporous Palladium-Copper Bimetallic Cathode and Hierarchical ZnO-Based Nanowire Arrays Photoanode

5.1 Introduction

Photoelectrochemical (PEC) CO₂ reduction has been developed and researched as an alternative approach to obtain an efficient CO₂ reduction and reduced the corresponding energy demand, for it possess both the advantages of photocatalytic and electrocatalytic CO₂ reduction.¹ Since the first report about PEC CO₂ reduction over p-type gallium phosphide,² several semiconductors have been fabricated as photocathodes for CO₂ conversion, such as p-Si,^{3,4} p-InP,^{5,6} p-GaP,⁷ p-GaAs,⁸ n-GaAs,⁹ etc. In theory, there are three options for the assembly of PEC device: (I) p-type semiconductor photocathode and metal anode, (II) n-type semiconductor photoanode and metal cathode and (III) n-type semiconductor photoanode and p-type semiconductor photocathode.¹⁰ It is worthwhile to note that the previous reports of PEC CO₂ reduction mainly belong to the first strategy. The PEC processes were assembled of designed p-type semiconductor photocathodes for the directly CO₂ reduction and integrated with common used metal anodes, such as Pt, etc. Although these attempts demonstrated attractive activities, the high overpotentials of semiconductor photocathodes were required to obtain these results.¹¹ The well-studied phosphides and arsenides are rank poisonous, which would lead a high risk and

raise the cost during the manufacturing process. In addition, there are still limited suitable p-type semiconductors as photocathodes candidate.

The last two options for the assembly of PEC device, in particular the second strategy with n-type semiconductor photoanode and metal cathode, were well-studied for PEC water splitting.¹² It thus provides an alternative paradigm for the PEC CO₂ conversion. Moreover, in the previous reports, there are still limited reports about the overall PEC CO₂ conversion. From the point view of future application, the overall PEC CO₂ conversion performance is determined by not only the half reaction of CO₂ reduction, but also the other half reaction of water oxidation.⁹ Thus, both the cathodic and anodic materials should be studied to realize an efficient PEC CO₂ reduction when constructing the PEC device. An effective overall PEC CO₂ conversion device could be assembled by designing and fabricating both a semiconductor photoanode and a metal cathode. The half reaction of water oxidation is performed at the semiconductor photoanode. The half reaction of water oxidation is performed at the semiconductor photoanode. Thus it provides much more options to utilize oxides semiconductors, rather than the limited number of p-type phosphides and arsenides as photocathodes. It could facilitate the overall CO₂ conversion by effectively catalyzing the water oxidation and simultaneously supporting photogenerated electrons and active hydrogen to the cathode side. On the other hand, the half reaction of CO₂ conversion is carried out at metal cathodes through an electrocatalytic process. Metal electrodes have shown a great many merits in the selective reduction of CO₂. Although overpotentials still interfere in the development of electrocatalysts for CO₂ reduction, the overpotentials over metals are usually less than the p-type semiconductors due to the much lower resistance and better electron transfer.^{13, 14} Moreover, the excess energy consumption caused by these overpotentials could

be accommodated by the photogenerated electrons from the photoanode side within this designed PEC device.

In this chapter, a design and assembling of overall PEC CO₂ conversion device was studied by integrating the previous studied mesoporous palladium-copper bimetallic cathode and ternary hierarchical CNTs-ZnO-CO₃O₄ nanowire arrays photoanode for the selective conversion of CO₂ to CO. The effectiveness of both of the cathodic and anodic sides on the overall PEC CO₂ conversion performance was studied. And the overall performance of CO₂ conversion process was investigated in a two-electrode cell system to conform that it is a feasible strategy to realise the overall PEC CO₂ conversion by integrating an n-type semiconductor photoanode and a metal cathode.

5.2 Experimental methods

The photoelectrochemical conversion of CO₂ was measured on a CHI 660D electrochemical workstation. The electrolyte solution was aqueous 0.1 M KHCO₃ solution at cathodic side and 0.1 M K₂SO₄ at the anodic side in a gas-tight two compartment H-cell separated by a Nafion117 film. Both of the solutions were purged by Ar gas and the cathodic side was saturated with CO₂ successively before the measurement. The photocurrent response was investigated under the illumination of an AM 1.5 solar simulator (WXS-80C-3 AM 1.5G, 100 mW cm⁻²) in a two-electrode cell system, with mesoporous Pd₇Cu₃ alloy electrocatalysts (0.07 cm²) as cathode and hierarchical CNTs-ZnO-Co₃O₄ NWs composite as photoanode (1 cm²) as the schematic model shown in Fig. 5.1. Nanoparticle Pd₇Cu₃ alloy (N-PdCu) which was prepared without Brij 58 surfactant was also performed as cathode and pristine ZnO NWs (P-ZnO) as well as Pt foil was also

used as anode to contrast with the designed mesoporous Pd₇Cu₃ alloy (M-PdCu) cathode and the ternary CNTs-ZnO-Co₃O₄ NWs composite (T-ZnO) photoanode PEC device.

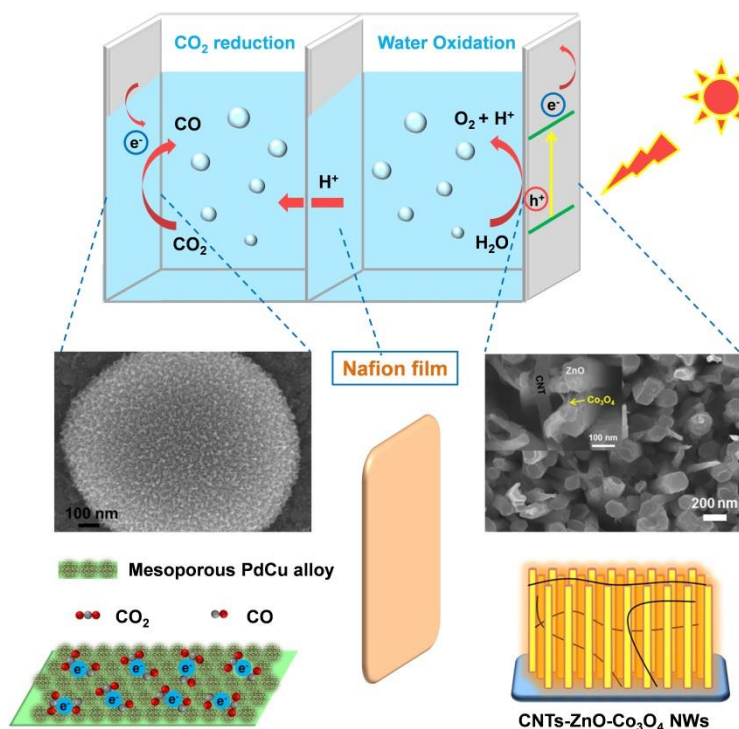


Fig. 5.1 Schematic model of the PEC device for the selective conversion of CO₂ to CO. Cathode: Mesoporous PdCu alloy; Photoanode: Ternary Hierarchical CNTs-ZnO-Co₃O₄ NWs composite.

The products of reduction half reactions in cathodic side were sampled and measured with a gas chromatograph (GC). The main products of CO₂ reduction CO and other carbon products were sampled and measured with a gas chromatograph (GC-14B, Shimadzu) equipped with a flame ionization detector (FID) according to the standard curves. The GC column is Porapak Q-methanizer for CO and CO₂ measurement, PEG1000 for organic products measurement. The product of competing water reduction reaction H₂ was measured with a gas

chromatograph (GC-8A, Shimadzu) with a TCD detector according to the standard curve. The GC column is 5A molecular sieve. The incident photon to electron conversion efficiency (IPCE) was calculated from chronoamperometry measurements using a motorized monochromator (M10; Jasco Corp.).

5.3 Results and discussions

5.3.1 The effect of photoanodes on the overall PEC CO₂ conversion

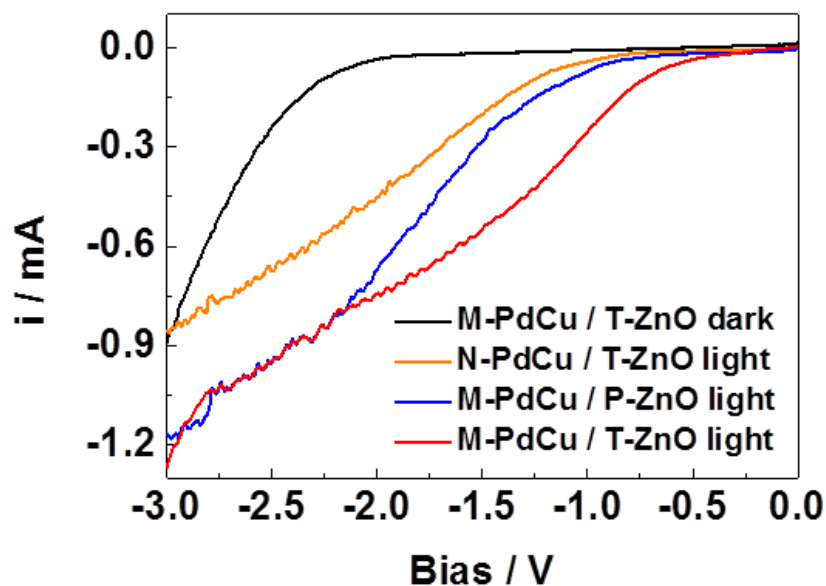


Fig. 5.2 Current-voltage curves of the PEC device with various cathode and photoanode combinations; M-PdCu: mesoporous Pd₇Cu₃ alloy, N-PdCu: nanoparticle Pd₇Cu₃ alloy, T-ZnO: ternary CNTs-ZnO-Co₃O₄ NWs composite, P-ZnO: pristine ZnO NWs.

The photoactivity of the designed PEC device was investigated under the illumination of an AM 1.5 solar simulator in a two-electrode cell system. Nanoparticle Pd₇Cu₃ alloy (N-PdCu), which was prepared without Brij 58

surfactant, was also performed as a contrastive cathode to the designed mesoporous Pd₇Cu₃ alloy (M-PdCu) cathode. Pristine ZnO NWs (P-ZnO) were prepared as photoanodes to contrast with the ternary CNTs-ZnO-Co₃O₄ NWs composite (T-ZnO) photoanode. In addition, Pt foil was employed as anode as well to compare the electrochemical CO₂ conversion process with the PEC process. Fig. 5.2 shows the total current-voltage curves measured by a two-electrode cell with various cathode and anode combinations in the bias region from 0 V to -3 V. The photoelectric response of the designed PEC device with M-PdCu/T-ZnO exhibits an obviously dark and light current difference, which indicates a remarkable photogenerated charge separation within the PEC device. When replacing the cathodic and anodic side by N-PdCu and P-ZnO, respectively, the photocurrent response varied dramatically. It thus can be deduced that both of the cathodic and anodic sides play a crucial role in contributing to the overall PEC performance. Moreover, the photocurrent of M-PdCu/T-ZnO starts at a more positive onset bias than the electrochemical counterpart with Pt foil as anode (Fig. 5.3). It shows a photocurrent of -0.03 mA at -0.5 V and dramatically increases to -0.75 mA at -2.0 V under illumination, which is about 4.3 times and 25 times larger than the current of Pt anode and dark current, respectively. The electrochemical counterpart, whereas, only exhibits a little current response until the applied bias increasing to the very negatively higher region. These results imply that the photogenerated electrons could contribute to most of the energy demand for the CO₂ reduction, especially at the lower biases.

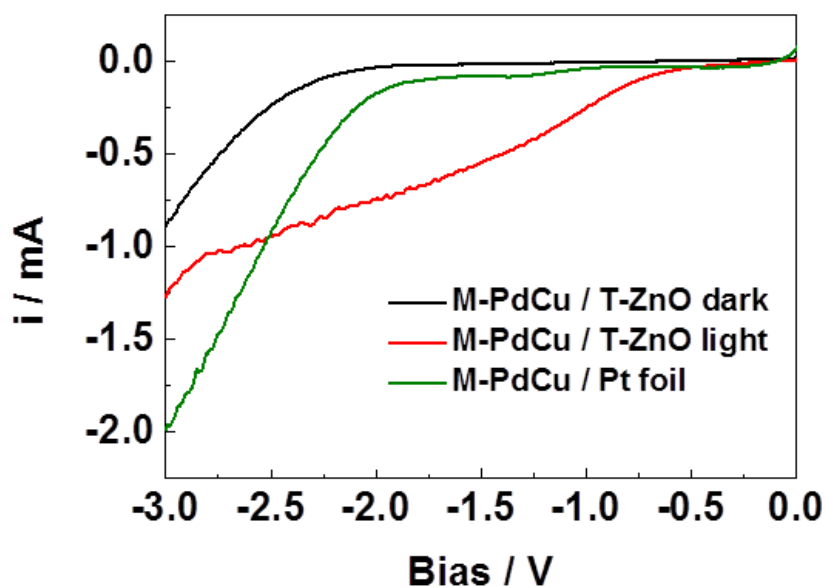


Fig. 5.3 Current-voltage curves comparison between the electrochemical CO_2 conversion process (M-PdCu / Pt foil) and the PEC process (M-PdCu / T-ZnO).

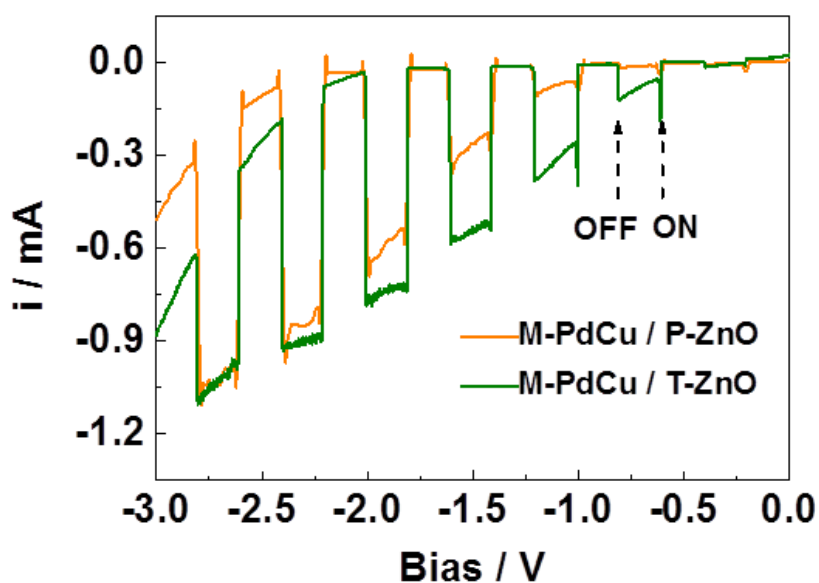


Fig. 5.4 Current-voltage curves of M-PdCu / P-ZnO and M-PdCu / T-ZnO under chopped light illumination.

The effect of photoanodes on the photoresponsibility of the PEC device was examined under chopped light illumination, by using pristine ZnO NWs (P-ZnO) and ternary CNTs-ZnO-Co₃O₄ NWs composite (T-ZnO) as photoanodes, respectively. Here the mesoporous Pd₇Cu₃ (M-PdCu) alloy was fixed as the cathode. The current-voltage scans were carried out during repeated ON-OFF illumination cycles as shown in Fig. 5.4. A steady and prompt photoresponse can be observed for both of these two photoanodes, with T-ZnO demonstrating much larger photocurrent, in particular at the lower biases. The assembling of N-PdCu/T-ZnO also performs a similar photoresponse performance as shown in Fig. 5.5.

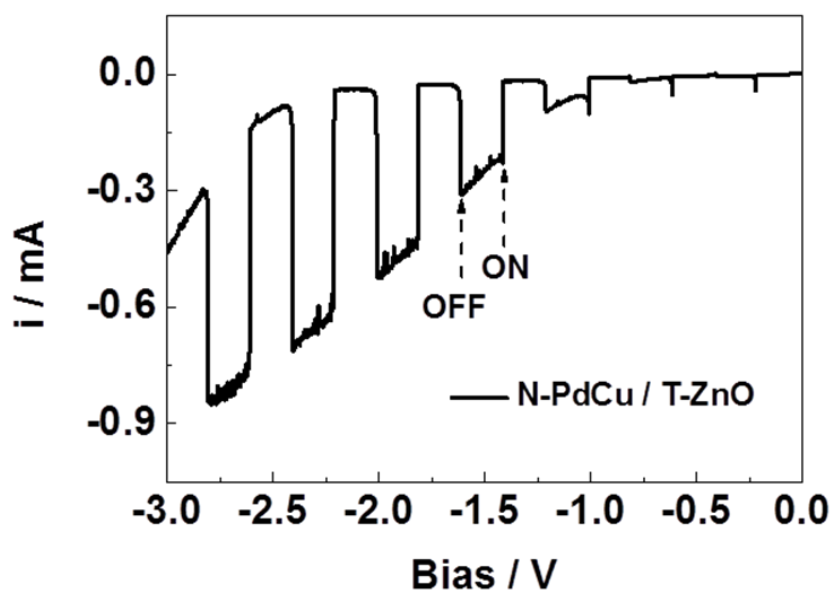


Fig. 5.5 Current-voltage curves over nanoparticle Pd₇Cu₃ (N-PdCu) alloy cathode and ternary CNTs-ZnO-Co₃O₄ NWs composite (T-ZnO) photoanode under chopped light illumination.

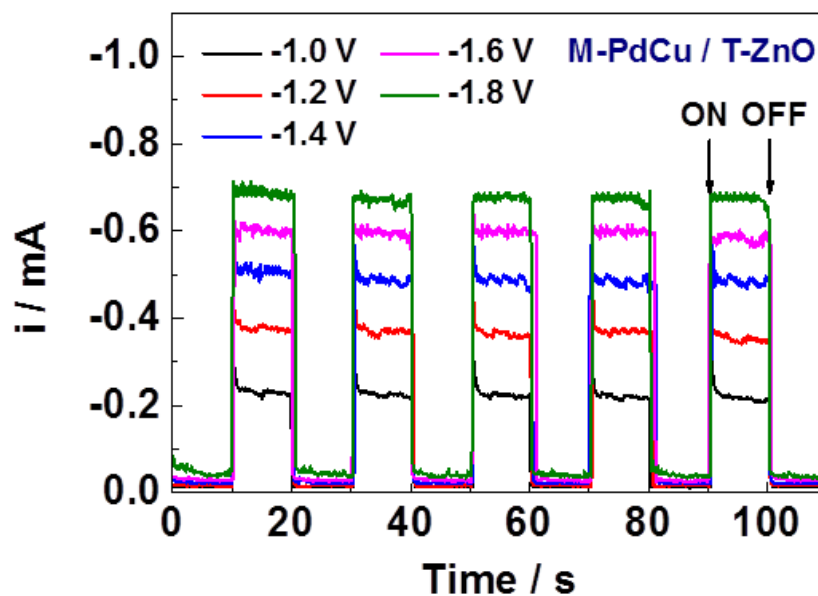


Fig. 5.6 Chopped amperometric I-t curves of M-PdCu / T-ZnO at various biases.

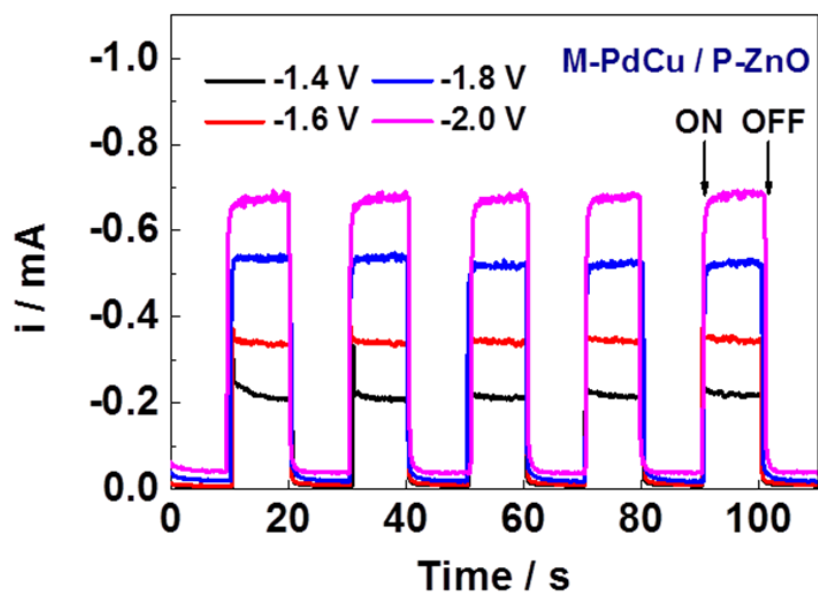


Fig. 5.7 Chopped amperometric I-t curves of M-PdCu / P-ZnO at various biases.

Fig. 5.6 exhibits the transient photocurrents of T-ZnO photoanode during the light ON-OFF cycling at various biases. The corresponding amperometric I-t curves of P-ZnO photoanodes are shown in Fig. 5.7. All of the chopped curves

exhibit prompt and reproducible photocurrent responses upon each bias (Fig.5.6 and Fig. 5.7). T-ZnO exhibits obviously larger photoresponses than P-ZnO at all the applied biases, with photocurrents of -0.51 mA at -1.4 V and -0.68 mA at 1.8 V, which is ca. 2.3 times and 1.3 times larger than the P-ZnO counterpart, respectively. It thus could be concluded that the anodic part within the PEC device significantly determines the overall PEC activity of CO₂ conversion. T-ZnO photoanode possess much better photoactivity due to its much better solar light utilization efficiency and increased reaction rates of water oxidation as discussed in Chapter 4. Moreover, these results confirm that solar energy could serve as a considerable energy source to carry out the overall PEC CO₂ conversion in our designed PEC device, especially at lower biases before the photocurrent reaching its limiting current.

5.3.2 The effect of metal cathodes on the overall PEC CO₂ conversion

The apparent photocurrent response is not only from the desired CO₂ reduction, but also contains the current from water reduction reaction as exhibited in equation (1) and (2). Because hydrogen evolution reaction (HER) from water reduction is a very aggressive competing reaction to the selective reaction of CO₂ to CO.

Desired CO₂ reduction:



Competing reaction of CO₂ reduction:



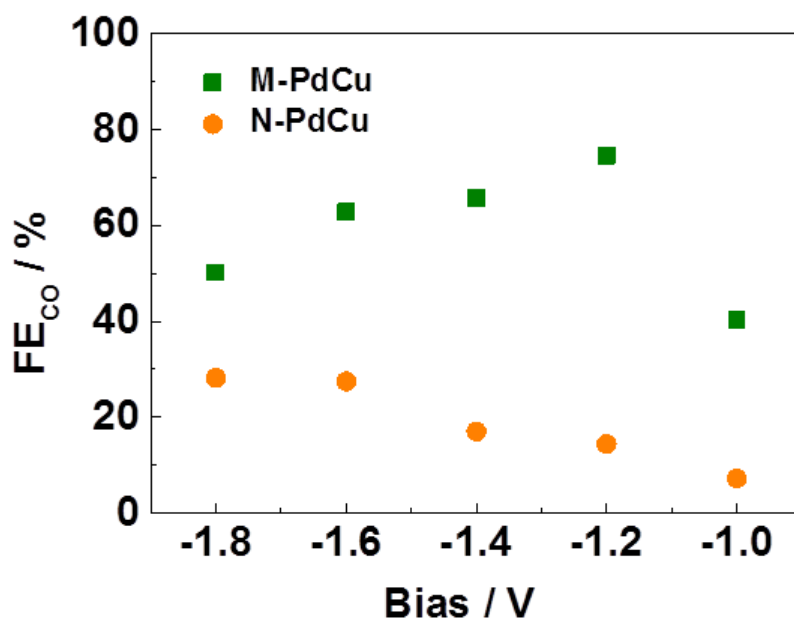


Fig. 5.8 Faradaic efficiencies for CO of the overall PEC CO₂ conversion over M-PdCu and N-PdCu alloy cathodes, with T-ZnO as photoanode.

Thus, Faradaic efficiency (FE) was examined to investigate the photocurrent contribution of each product as well as to study the effect of cathodes on the overall PEC CO₂ conversion. Mesoporous Pd₇Cu₃ (M-PdCu) alloy and nanoparticle Pd₇Cu₃ (N-PdCu) were served as cathode, respectively, and ternary CNTs-ZnO-Co₃O₄ NWs composite (T-ZnO) was fixed as photoanode. The Faradaic efficiency (FE) of the PEC CO₂ conversion process can be expressed as $FE = znF / it$, where z (reaction electron number) = 2 for CO and H₂, n is the GC detected product molar number (mol), F is the Faradaic constant (C mol⁻¹), i is the photocurrent (A) and t is the reaction time (s). Both the FEs for CO over M-PdCu and N-PdCu are highly depended on the applied biases, in which M-PdCu exhibits much higher FE_{CO} than N-PdCu at all the biases as shown in Fig. 5.8. The maximum FE_{CO} over M-PdCu appears to be ca. 75% at -1.2 V, and

N-PdCu only shows a maximum FE_{CO} of 31% at a more negative bias -1.8 V. These results suggest that the architecture difference between M-PdCu and N-PdCu lead to different CO selectivity during their CO_2 reduction processes. M-PdCu with mesoporous structure could effectively reduce the overpotential for converting CO_2 to CO (from -1.8 V to -1.2 V). According to the previous reports, active sites (in particular edge sites) can facilitate the stabilization of intermediates (such as $COOH^*$) and promote the formation of CO during the CO_2 conversion process by adjusting the reaction mechanism and the rate-determining step.^{15, 16} M-PdCu has been confirmed that it possesses more active sites than N-PdCu for the selective conversion CO_2 to CO due to its mesoporous nanostructure according to the study in Chapter 3.

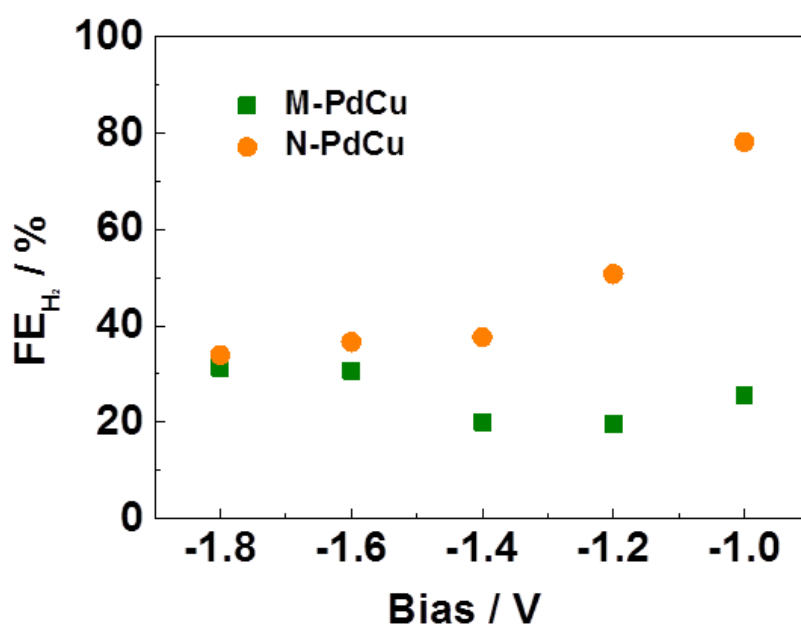


Fig. 5.9 Faradaic efficiencies for H_2 of the overall PEC CO_2 conversion over M-PdCu and N-PdCu alloy cathodes, with T-ZnO as photoanode.

The FEs of the competing hydrogen evolution reaction (HER) are shown in Fig. 5.9. M-PdCu exhibits much lower FE_{H_2} at almost all the applied biases. According to Azuma et al's summary about aqueous CO_2 reduction on metal electrodes,¹⁷ both pure Pd and Cu electrodes exhibit high FE_{H_2} (ca. 90% on Pd and ca. 50% on Cu at -2.2 V vs. SCE) and very low FE_{CO} (ca. 3.2% on Pd and ca. 5.4% on Cu at -2.2 V vs. SCE) in aqueous electrolyte. This can be ascribed to their relative low overpotential for HER.¹⁸ The selectivity exhibits an obvious improvement on N-PdCu (FE_{CO} ca. 31% and FE_{H_2} ca. 34% at -1.8 V), which can be ascribed to the geometric and electronic effects within the alloy materials.¹⁹ Moreover, the product ratio between CO and H_2 was further increased on M-PdCu by forming the mesoporous nanostructure (FE_{CO} ca. 75% and FE_{H_2} ca. 19% at -1.2 V). These results suggest that the mesoporous architecture not only benefits the CO formation, but depresses the competing hydrogen evolution effectively in aqueous electrolyte as well.

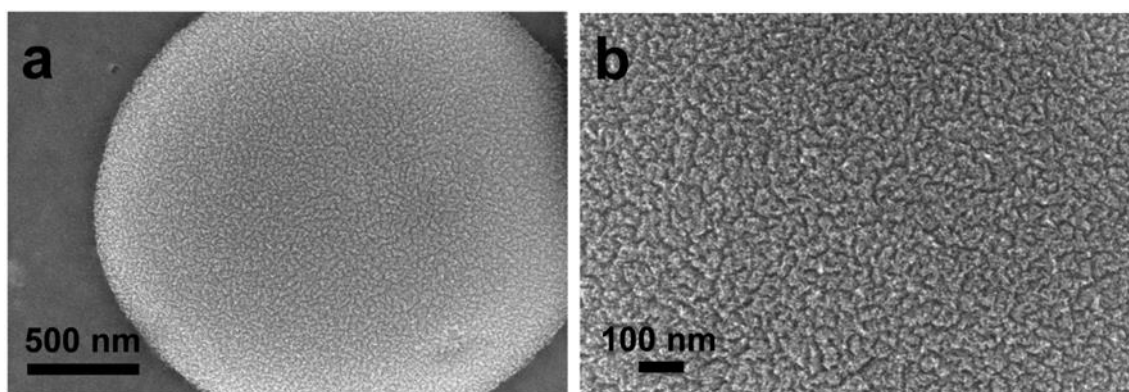


Fig. 5.10 a) and b) Top-surface SEM images of mesoporous Pd₇Cu₃ alloy after the PEC measurements.

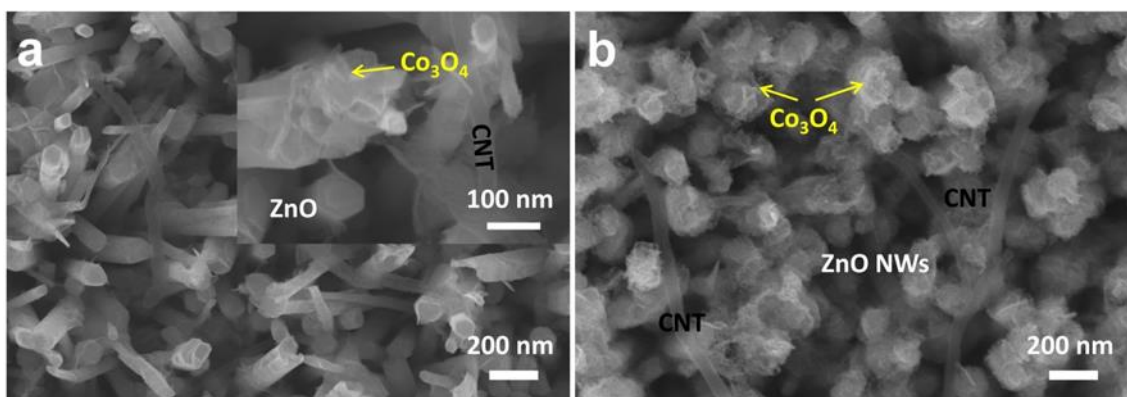


Fig. 5.11 SEM images of ternary CNTs-ZnO- Co_3O_4 NWs composite a) before and b) after the PEC measurements.

The SEM images of the M-PdCu cathode and T-ZnO photoanode after the PEC measurements are shown in Fig. 5.10 and Fig. 5.11, respectively. The Pd-Cu alloy still exhibits a highly dispersed mesoporous surface (Fig. 5.10). On the other hand, the semiconductor photoanode maintains at the ternary architecture with CNTs and Co_3O_4 decorated ZnO NWs morphology after the PEC process (Fig. 5.11). A long term test was investigated at -1.2 V to examine the durability of overall PEC CO_2 conversion over M-PdCu/T-ZnO as shown in Fig. 5.12. The reaction demonstrates a steady current response and both the FEs for CO and H_2 only show slightly changes. Thus, it can be deduced that the assembling of M-PdCu/T-ZnO can provide a stable overall PEC conversion of aqueous CO_2 to CO. Fig. 5.13 shows the electrochemical CO_2 reduction performances of mesoporous Pd_7Cu_3 and nanoparticle Pd_7Cu_3 with optimal FE_{CO} of ca. 80%. The PEC CO_2 conversion performances shown in Fig. 5.8 (ca. 75 %) demonstrate almost identical relationship of the selectivity and activity with the electrochemical counterpart. The FEs for CO show a slightly shrink, which could be ascribed to the enhancement of increased ohmic resistances of the overall PEC

device.¹⁰ It thus can be deduced that the overall PEC activity for CO₂ conversion is directly determined by the catalytic characteristic of metal cathodes, while the photoanode dominates the solar utilization efficiency of the whole process.

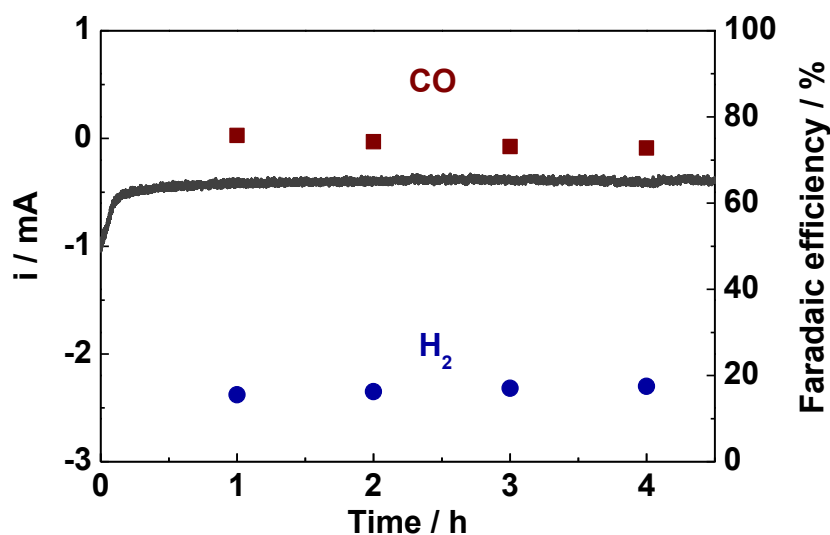


Fig. 5.12 Durability test over M-PdCu/T-ZnO (mesoporous Pd₇Cu₃ alloy cathode and ternary CNTs-ZnO-Co₃O₄ NWs composite photoanodes) at -1.2 V.

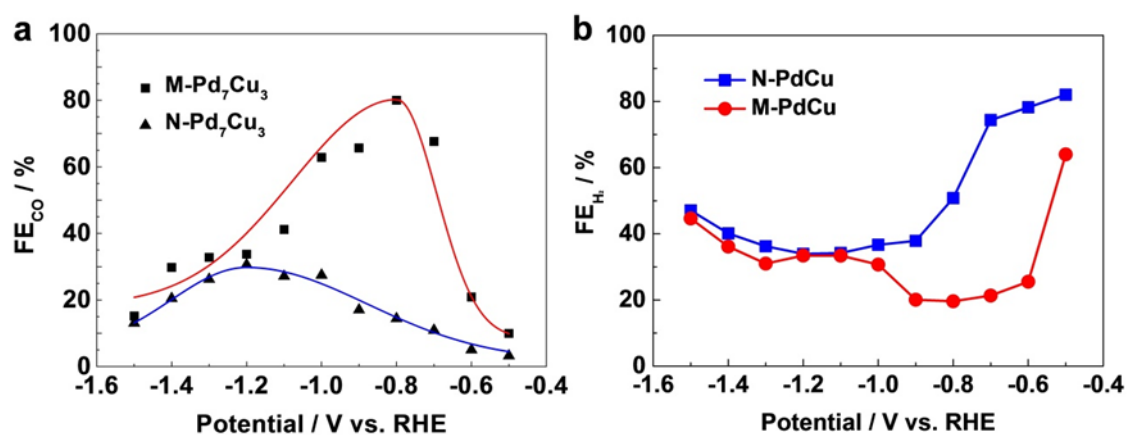


Fig. 5.13 Faradaic efficiencies for a) CO and b) H₂ of the electrochemical CO₂ reduction over M-PdCu and N-PdCu alloys, with Pt and Ag/AgCl (in saturated KCl) electrode as counter and reference in a three-electrode cell system.

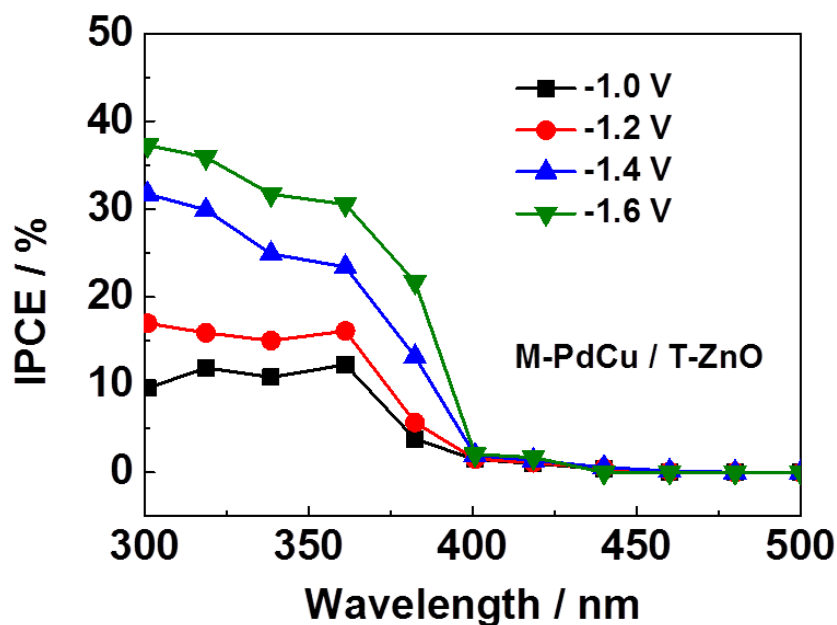


Fig. 5.14 IPCE spectra of M-PdCu/T-ZnO at high FE_{CO} bias region.

Incident photon to current conversion efficiency (IPCE) was evaluated at high FE_{CO} bias region during the PEC process, in order to understand the interplay between the photoactivity and light absorption as shown in Fig. 5.14. IPCE can be expressed as $IPCE = 1240 j_p(\lambda) / \lambda E_\lambda(\lambda)$, where $j_p(\lambda)$ is the measured photocurrent density (mA cm^{-2}), λ is the incident light wavelength (nm) and $E_\lambda(\lambda)$ is the incident monochromatic light power density (mW cm^{-2}) at a specific wavelength. The IPCE values are greatly affected by the applied bias and increases with the bias obviously during the high FE_{CO} bias region. It exhibits a photon conversion efficiency of ca. 16% at 340 nm -1.2 V and doubled to ca. 31% at -1.6 V. This result confirms that the PEC process could definitely utilize solar light to carry out the overall CO_2 conversion during the high FE_{CO} bias region. However, the IPCE value exhibits an obvious gap to the maximum photon conversion efficiency of the ternary CNTs-ZnO- Co_3O_4 NWs photoanode for PEC water oxidation as studied in Chapter 4 (IPCE of 52.5% at ca. 1.2 V vs. RHE).

The overall PEC process should be controlled by both the cathodic and photoanodic sides, and the low-reaction-rate side should mainly determine the overall PEC reaction.²⁰ As illustrated in Fig. 5.2, M-PdCu / T-ZnO exhibits much larger photocurrent than M-PdCu / P-ZnO until ca. -2.1 V and the photocurrents approach to identical response after ca. -2.1 V. It can be deduced that at lower biases (before -2.1 V), the anodic side presents relative low reaction rates and is still in the growth stage of photocurrent for water oxidation. It consequently serves as the dominant side of the overall PEC process. Both the T-ZnO and P-ZnO phototodes exhibit obvious enhancements of photocurrents with increasing the applied bias, in which the photoresponse disparity can be ascribed to their photocatalytic ability gap for water oxidation. In our designed PEC device, the high FE_{CO} biases (-1.0 V ~ -1.6 V) appears at anodic controlled region, thus the IPCE values do not catch up with the optimal photon conversion efficiency and increase with the bias. When further increase the applied bias beyond -2.1 V, the photocurrents are close to identical response (Fig. 5.2). Both the two PEC devices possess the same cathodes M-PdCu, it thus could be assumed that the cathodic reaction instead of the anodic side to become the rate determining side at higher biases (after -2.1 V).

In order to further verify this assumption, the photocurrent responses of different area ratios M-PdCu / T-ZnO were examined as shown in Fig. 5.15. The M-PdCu alloy cathodes were prepared on purchased glassy carbon (GC) substrate (diameter = 3 mm, BAS Inc.) and thus the cathodic area was fixed as ca. 0.07 cm². The T-ZnO photoanodes were prepared on FTO substrate by a hydrothermal process. The T-ZnO photoanodes were prepared to 0.5 cm × 1.0 cm, 1.0 cm × 1.0 cm, 1.5 cm × 1.5 cm and 2.0 cm × 2.0 cm by cutting the FTO substrates to appropriate sizes. As shown in Fig. 5.15, the photocurrent response increase with

the photoanodic areas and they do not approach to identical current at higher biases (such as -2.1 V). These results suggest that the overall PEC process is mainly controlled by the photoanodic side at the applied bias region and our previous assumption is not correct. The similar photocurrent responses of M-PdCu / P-ZnO and M-PdCu / T-ZnO are not caused by the change of determined side from photoanode to cathode. The probably reasons might be as follows. At lower biases, T-ZnO exhibits larger photocurrent than P-ZnO because a better charge separation and transfer of photogenerated electron-hole pairs by loading CNT and Co_3O_4 as cocatalysts. When the applied bias increase to higher region, the external bias is strong enough to separate and transfer the photogenerated charge on P-ZnO as well as preventing the electron-hole recombination. ZnO serves as the photoresponse semiconductor in both T-ZnO and P-ZnO, thus they demonstrate similar photocurrent at high bias region.

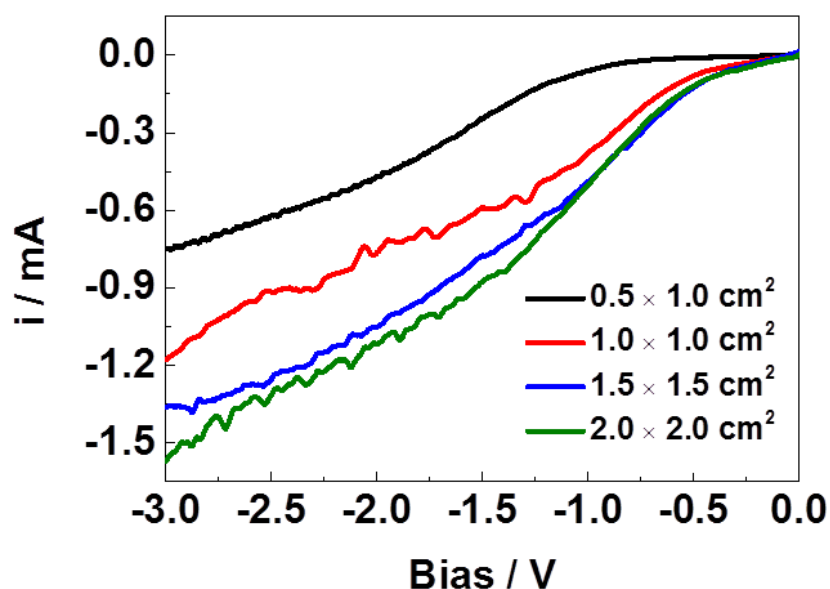


Fig. 5.15 Photocurrent responses of the assembly of fixed area mesoporous Pd_7Cu_3 alloy cathode (ca. 0.07 cm^2) and various areas of ternary CNTs-ZnO- Co_3O_4 NWs photoanode.

In addition, although the results in Fig. 5.15 show the photoanode as the main rate-determined side, the photocurrent response become approximate to each other with increasing the photoanode area. The photocurrent differences between the adjacent photoanode areas become smaller. The photocurrents of the area $2.0\text{ cm} \times 2.0\text{ cm}$ and $1.5\text{ cm} \times 1.5\text{ cm}$ almost exhibit identical responses before ca. -1.0 V , and they demonstrated very small difference at high biases (after ca. -1.0 V). This might be caused by the non-uniform distribution of light intensity on the large area photoanode surface ($2.0\text{ cm} \times 2.0\text{ cm}$). Due to the size limit of our autoclave for hydrothermal preparation, we did not examine the photocurrent response on larger area photoanode. It can be deduced that if the photoanode area can be larger to some extent, the photocurrent will not be increased with the area and the overall PEC reaction will be mainly determined by the cathodic side. Thus, in the point of realizing a maximum performance of our assembly of M-PdCu / T-ZnO, the area ratio between T-ZnO photoanode and M-PdCu cathode should be larger enough, so that the photoanode could support enough photogenerated electrons to the cathode. Because the FE of overall PEC reaction is mainly determined by the catalytic characteristic of the cathode materials, the maximum FE for CO will not be changed by enlarging the photoanode area. However, the optimal FE_{CO} can be obtained at more positive bias. For example, the maximum FE_{CO} (ca. 75%) was obtained at -1.2 V when the photoanode area is $1.0\text{ cm} \times 1.0\text{ cm}$. After enlarging the photoanode area to $2.0\text{ cm} \times 2.0\text{ cm}$, an identical FE_{CO} can be obtained at ca. -1.0 V .

Table 5.1 Comparison with the previous results of PEC CO₂ reduction to CO in aqueous electrolyte. (* This work)

Materials	Surface orientation	Electrolyte	Metal particles on surface or in solution	Potential / V	Faradic efficiency
p-Si ²¹ (1.1 eV)	(111)	0.1 M KHCO ₃	Au	-0.74 vs. SCE	CO (62.2%)
p-InP ²² (1.3 eV)	(100)	0.1 M Na ₂ SO ₄	None	-1.2 vs. SCE	CO (16.1%) HCOOH (4.6%) H ₂ (70.7%)
p-GaP ²⁰ (2.3 eV)	(100)	0.1 M KHCO ₃	None	-0.9 vs. Ag/AgCl	CO (11.9%) HCOOH (56.2%) H ₂ (2.3%)
p-CdTe ²² (1.4 eV)	(111)	0.1 M Na ₂ SO ₄	None	-1.2 vs. SCE	CO (43.3%) HCOOH (5.4%) H ₂ (45.1%)
M-PdCu* /T-ZnO	N/A	0.1 M KHCO ₃	None	Bias -1.2 in two electrode cell	CO (75%) H ₂ (19%)

The comparison of our result with the previous reports for PEC CO₂ reduction to CO in aqueous electrolytes is summarized in Table 5.1. The overall PEC CO₂ conversion performance of our designed device exhibits an attractive superiority than the previous reports over p-type photocathodes for aqueous CO₂ reduction to CO. It provides a better selectivity between HCOOH (or HCOO⁻) and CO. Both formate and CO are 2-electron CO₂ reduction reactions, and are competing reactions with each other. The selectivity between these 2-electron products is highly depended on the stability of intermediates (COOH*). Metal

catalysts (Au, Ag, Cu, etc.)^{17, 23} are usually cited for their superior ability in selecting CO₂ reduction products than semiconductors. In this work, CO is the dominate product, which can be ascribed to the abundant active sites and adjusted electronic structure of the mesoporous Pd-Cu alloy for CO evolution.⁴⁰ In addition, it also indicates that the activity and photon conversion efficiency could be further improved by assembling a more matched cathode and photoanode combination from various options of metal cathodes and n-type photoanodes. The previous researches about PEC CO₂ reduction mainly focused on improving the activities of each half reaction on cathodic or anodic side. The engineering techniques for PEC device construction should also be paid with more attentions for the overall PEC CO₂ conversion in the future. This report provides alternative possibility to the research of PEC CO₂ reduction by substituting and integrating different metal cathode electrocatalysts and photocatalysts anode materials. The corresponding assembling technique between the metal cathode and semiconductor photoanode will be studied in our following work.

5.4 Conclusions

In summary, our results show that a selective reduction of CO₂ to CO was achieved over a designed photoelectrochemical device by using novel mesoporous paladium-copper bimetallic cathode and ternary hierarchical ZnO-based NWs arrays photoanode. The mesoporous Pd₇Cu₃ bimetallic catalysts exhibit superior activity and selectivity as cathode for the PEC CO₂ reduction, while the ternary CNTs-ZnO-Co₃O₄ NWs photoanode demonstrates high solar utilization efficiency. The overall PEC CO₂ conversion activity is an integrated performance and it is determined by both of the cathodic and anodic side. The overall photocurrent response is mainly controlled by the photoanodic side

(CNTs-ZnO-Co₃O₄ NWs composite photoanode) at the applied bias region in our PEC system. The designed PEC device exhibits much larger photocurrent than the current of electrochemical CO₂ reduction counterpart in a two-electrode cell system at the lower applied biases. The maximum FE_{CO} of the PEC CO₂ conversion is ca. 75% at -1.2 V with IPCE of 16% at 340 nm. We believe that our designed PEC device provide an alternative strategy towards obtaining efficient, selective and low energy consumption PEC CO₂ reduction in the future.

References

1. B. Kumar, M. Llorente, J. Froehlich, T. Dang, A. Sathrum and C. P. Kubiak, *Annu. Rev. Phys. Chem.*, 2012, **63**, 541-569.
2. M. Halmann, *Nature*, 1978, **275**, 115-116.
3. M. G. Bradley and T. Tysak, *J. Electroanal. Chem.*, 1982, **135**, 153-157.
4. M. G. Bradley, T. Tysak, D. J. Graves and N. A. Viachiopoulos, *J. Chem. Soc., Chem. Commun.*, 1983, DOI: 10.1039/C39830000349, 349-350.
5. B. A. Parkinson and P. F. Weaver, *Nature*, 1984, **309**, 148-149.
6. S. Kaneco, H. Katsumata, T. Suzuki and K. Ohta, *Appl. Catal., B*, 2006, **64**, 139-145.
7. E. E. Barton, D. M. Rampulla and A. B. Bocarsly, *J. Am. Chem. Soc.*, 2008, **130**, 6342-6344.
8. W. M. Sears and S. R. Morrison, *J. Phys. Chem.*, 1985, **89**, 3295-3298.
9. K. W. Frese and D. Canfield, *J. Electrochem. Soc.*, 1984, **131**, 2518-2522.
10. Y. Fang, J. Tong, Q. Zhong, Q. Chen, J. Zhou, Q. Luo, Y. Zhou, Z. Wang and B. Hu, *Nano Energy*, 2015, **16**, 301-309.

11. K. Hirota, D. A. Tryk, T. Yamamoto, K. Hashimoto, M. Okawa and A. Fujishima, *J. Phys. Chem. B*, 1998, **102**, 9834-9843.
12. T. Hisatomi, J. Kubota and K. Domen, *Chem. Soc. Rev.*, 2014, **43**, 7520-7535.
13. J. Lee, Y. Kwon, R. L. Machunda and H. J. Lee, *Chem. Asian J.*, 2009, **4**, 1516-1523.
14. G. Centi and S. Perathoner, *Catal. Today*, 2009, **148**, 191-205.
15. W. Zhu, R. Michalsky, Ö. Metin, H. Lv, S. Guo, C. J. Wright, X. Sun, A. A. Peterson and S. Sun, *J. Am. Chem. Soc.*, 2013, **135**, 16833-16836.
16. S. Rasul, D. H. Anjum, A. Jedidi, Y. Minenkov, L. Cavallo and K. Takanabe, *Angew. Chem. Int. Ed.*, 2015, **54**, 2146-2150.
17. S. Shen, C. X. Kronawitter, J. Jiang, P. Guo, L. Guo and S. S. Mao, *Nano Energy*, 2013, **2**, 958-965.
18. T. Wang, X. Meng, P. Li, S. Ouyang, K. Chang, G. Liu, Z. Mei and J. Ye, *Nano Energy*, 2014, **9**, 50-60.
19. D. Kim, J. Resasco, Y. Yu, A. M. Asiri and P. Yang, *Nat. Commun.*, 2014, **5**.
20. Z. Chen, H. Dinh and E. Miller, *Photoelectrochemical Water Splitting: Standards, Experimental Methods, and Protocols*, Springer New York, 2013.
21. C. Delacourt, P. L. Ridgway, J. B. Kerr and J. Newman, *J. Electrochem. Soc.*, 2008, **155**, B42-B49.
22. A. J. Morris, G. J. Meyer and E. Fujita, *Acc. Chem. Res.*, 2009, **42**, 1983-1994.
23. K. Hirota, D. A. Tryk, K. Hashimoto, M. Okawa and A. Fujishima, Elsevier, Amsterdam, 1998.

Chapter 6 General Conclusion and Future Prospects

6.1 General conclusion

In this thesis, the main work is to obtain a highly efficient, selective and low energy consumption photoelectrochemical (PEC) CO₂ reduction process. The PEC device was constructed by integrating the designed metal cathode and n-type semiconductor photoanode. The effects of both the two designed materials on PEC CO₂ conversion performance were investigated respectively and synthetically. The detailed study could be concluded in the following parts.

1. Photocatalytic CO₂ reduction process was studied as a preliminary research for the following PEC CO₂ conversion by choosing NaTaO₃ as the photoresponse semiconductor due to its significantly negative conduction band and proper band gap. By introducing electron donor H₂ into the system, a stable reactivity has been obtained over the series of NaTaO₃ due to an effective release of the peroxides intermediates of water oxidation. Ru and Pt exhibited the best products selectivity among various loaded noble metals (Pt, Au, Cu, Pd, Ru) cocatalysts due to the much better charge separation as well as the enhanced hydrogen activation, stabilization and utilization in the presence of electron donor during the gaseous photocatalytic CO₂ reduction process.

2. Electrochemical CO₂ reduction process was studied as following step to achieve an efficient and selective CO₂ reusable performance by using noble metals as catalysts directly and also reserved as cathode materials for the following study of PEC CO₂ conversion. Novel mesoporous palladium-copper bimetallic electrocatalysts were fabricated via facile electrodeposition approach for the selective reduction of CO₂ to CO. Mesoporous nanostructure was confirmed that it could effectively roughen the catalysts surface and increase the active sites. While the compositional ratio between Pd and Cu

also determines the selective conversion of CO₂ to CO due to the synergistic geometric and electronic effects. The optimal ratio was obtained at Pd₇Cu₃, with FE_{CO} exceeding 80% at -0.8 V vs. RHE. DFT calculations suggest Pd atoms serve as the reactive centers with an enhanced CO₂, COOH* adsorption ability and CO desorption ability in the presence of Cu. Moreover, fabricating mesoporous bimetallic electrocatalysts provides a promising strategy towards obtaining efficient, selective and cost-effective electrochemical CO₂ reduction in the future research.

3. A hierarchical carbon nanotube (CNT) and Co₃O₄ decorated ZnO nanowire (NW) arrays composite was fabricated and reserved as photoanode for the half reaction of water oxidation within the photoelectrochemical (PEC) CO₂ conversion. The ternary CNTs-ZnO-Co₃O₄ NWs arrays exhibit significantly enhanced activity in PEC water oxidation compared with the pristine ZnO NWs, binary CNTs-ZnO NWs and Co₃O₄-ZnO NWs as photoanodes under AM 1.5G simulated sunlight. This can be attributed to the effectively improved photogenerated charge separation and transfer as well as the markedly accelerated water splitting reaction rates due to the specific ternary architecture.

4. Finally, an overall PEC CO₂ conversion was investigated by integrating the mesoporous Pd-Cu cathode and ZnO-based NWs arrays photoanode for the selective reduction of CO₂ to CO. The overall PEC CO₂ conversion activity was confirmed that it is an integrated performance and it is determined by both of the cathodic and anodic side. Solar energy could serve as a dominant energy source at all the high CO-selective biases for the PEC CO₂ conversion. Moreover, integrating noble metal cathode electrocatalysts and n-type photocatalysts anode materials opens up a promising strategy towards obtaining efficient, selective and low energy consumption PEC CO₂ conversion in the future research.

Generally, this thesis confirmed that integrating functional nanostructured

bimetallic cathode and n-type hierarchical composite photoanode provides a promising approach to carry out the overall PEC CO₂ conversion. The mesoporous bimetallic nanostructures could effectively increase the density of specific active sites for the selective conversion of CO₂ to CO at the cathode side. The harvested active sites not only stabilized the intermediates COOH*, but also altered the adsorption abilities of CO₂ and CO to benefit the CO generation. In the photoanode side, the ternary nanowire architecture with certain functional component facilitated the water oxidation reaction by effectively lowering the overpotential and accelerating the reaction rates. The loaded dual cocatalysts also benefited the electron-hole pair separation and transfer, respectively, for an efficient solar utilization. Thus, both the designed cathodic and anodic materials synthetically contributed to the performance of overall PEC CO₂ conversion. Moreover, this study opened up a perspective strategy towards obtaining efficient, selective and low energy consumption PEC CO₂ reduction in the future research.

6.2 Future prospects

Based on the present study, the following researches remain as challenges towards achieving efficient and selective CO₂ reduction.

1. In the aspect of photocatalytic CO₂ reduction, some other cost-effective electron donors should be studied to substitute H₂. The effect of particle size and nanostructure of cocatalysts are essential to the photocatalytic activity, which need to be investigated. In addition, loading dual cocatalysts with certain function is also a potential approach to improve the activity of gaseous photocatalytic CO₂ reduction.

2. In the point view of PEC CO₂ conversion, both the cathodic and anodic sides remain as the research topic to further improve the activities. About metal cathode

materials, mesoporous alloys have been confirmed effective for the selective CO₂ conversion. However, there are still possibilities to further reduce the overpotential and improve the selectivity of CO₂ conversion, in particular the selective reduction of CO₂ to hydrocarbon products. To prepare nanoscale bimetallic and even trimetallic alloys with functional nanostructure is a potential strategy to further improve the catalytic performance. Besides, the assembling way of the PEC device, which is not only related with the design of cathode and anode materials but also comprises the specific engineering techniques, is a challenging issue to further improve the activity of overall PEC CO₂ conversion.

Acknowledgement

I would like to express my deep and sincere gratitude to my supervisor, Prof. Jinhua Ye. She kindly provided me the opportunity to continue my PhD study in Hokkaido University and National Institute for Materials Science (NIMS) and she introduced me to the field of photocatalysis and gave me patient and meticulous direction about my study. Her wide knowledge and her logical way of thinking have been of great value for me. And her understanding, encouraging and personal guidance have provided a good basis for the present thesis.

I am deeply grateful to my vice supervisor, Hidenori Noguchi sensei and Naoto Umezawa sensei, for their detailed and constructive comments. I would also like to thank Dr. Peng Li, for his valuable advice and friendly help. His extensive discussions and constructive suggestions around my work have been very helpful for my study.

During this work I have also obtained a lot of help from my group members. I wish to extend my warmest thanks to Dr. Tetsuya Kako for sharing me with the fundamental knowledge of photocatalysis. I wish to express gratitude to Dr. Junjie Wand for his great help in the calculation part. I would also like to thank Dr. Shuxin Ouyang, Dr. Lequan Liu, Dr. Zongwei Mei, Dr. Kun Chang, Dr. Tao Wang, Dr. Qing Kang, Dr. Junyu Cao, Dr. Hua Xu, Dr. Jianjun Guo, Dr. Huimin Liu and Dr. Huabin Zhang for their unselfish help and guidance. I still wish to thank other members, Mrs. Aya Hagino, Ms. Haruna Kurokawa, Dr. Guixia Zhao, Dr. Xianguang Meng, Mr. Guigao Liu, Ms. Qing Yu, Mr. Li Shi, Mr. Xiao Hai and Ms. Hong Pang for their help in experiments and daily life.

I wish to thank my parents for their constant support and encouragement in all my PhD endeavors.